

University of St Andrews



Full metadata for this thesis is available in
St Andrews Research Repository
at:

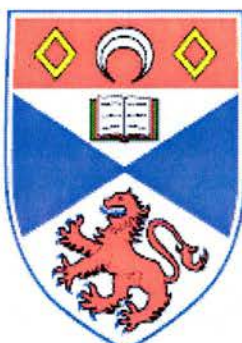
<http://research-repository.st-andrews.ac.uk/>

This thesis is protected by original copyright

Compact femtosecond lasers: routes to improved practicality and adaptability

*Thesis submitted for the degree of
Doctor of Philosophy
to the University of St Andrews
by
Barry Stormont*

*J.F. Allen Research Laboratories
Department of Physics and Astronomy
University of St Andrews
North Haugh
St Andrews,
Fife KY16 9SS*



Th
F65

Declarations

I, Barry Stormont, hereby certify that this thesis, which is approximately forty thousand words in length, has been written by me, that it is a record of work carried out by me and that it has not been submitted in any previous application for a higher degree.

Signature of Candidate:

Date: *4/8/2005*

I was admitted as a research student and candidate for the degree of Doctor of Philosophy in October 2000; the higher study for which this is a record was carried out at the University of St Andrews between 2000 and 2004.

Signature of Candidate:

Date: *4/8/2005*

I hereby certify that the candidate has satisfied the conditions of Resolution and Regulations appropriate for the degree of Doctor of Philosophy and the candidate is qualified to submit this thesis in application for that degree.

Signature of Supervisor:

Date:

In submitting this thesis to the University of St Andrews I understand that I am giving permission for it to be made available for use in accordance with the University Library for the time being in force, subject to any copyright in the work not being affected thereby. I understand that the title and abstract will be published, and that a copy may be made available to any bona fide library or research worker.

Signature of Candidate:

Date: *4/8/2005*

“...hold down the chord of C,
Pluck the fretted bass string the thumb of the right hand,
And pluck the third, second and third strings with the first, second and third fingers of
the right hand...”

Abstract

In this thesis, a number of practical femtosecond laser systems are described. Through appropriate selection and design of the intracavity optics used in these lasers, increased adaptability is achieved without making any compromise on the robustness of the final laser design. The laser systems developed during the course of this project made use of Ti: sapphire and Cr: LiSAF as gain media and took full advantage of the optical properties of each.

The Ti: sapphire gain medium has been used in the demonstration of a low-threshold laser system pumped by an inexpensive, compact, green laser. A design was also assessed where a femtosecond pulse train was produced at a multi-gigahertz pulse repetition frequency. This was made possible through the use of specially engineered intracavity mirrors that were designed as part of this work.

Cr: LiSAF crystals when optically pumped with inexpensive red laser diodes are usually regarded as low-gain laser materials. As part of the work presented in this thesis a femtosecond laser based on this material was taken to a pulse repetition rate as high as 1GHz. This approaches the fundamental limit set by the optical properties of the material without the need for stabilisation to prevent damage to the optical components. Also, a scheme whereby the centre wavelength of a femtosecond Cr: LiSAF laser can be tuned without the use of intracavity prisms has been described. This scheme permits the oscillating bandwidth to be controlled thereby allowing a degree of control over the intracavity pulse duration.

The research presented in this thesis shows that it is possible to design a laser that is a highly versatile source of ultrashort optical pulses. These concepts and configuration options illustrate that femtosecond lasers can be designed to be highly adaptable tools capable of opening up new avenues of research across science and technology.

Synopsis

In chapter 1, the key issues surrounding ultrashort pulses in the context of this thesis are presented. Pulse propagation through dispersive and nonlinear media is described. Modelocking techniques allowing the generation of ultrashort optical pulses are discussed, and particular attention is paid to techniques that rely on an intracavity semiconductor saturable absorber mirror. The technique of two-photon autocorrelation is described as a valuable tool for inferring the duration of ultrashort optical pulses. The information and commentary presented in chapter 1 provides the basis on which the work described in subsequent chapters is built.

Chapter 2 includes a description of a number of different mirror-based dispersion compensation schemes. Particular attention is paid to Gires-Tournois interferometer mirror based schemes due to their inherent ease of optimisation. Techniques through which the dispersion of an optical element or entire laser cavity can be measured are presented. The technique of white-light interferometry is used to measure the dispersion in reflection of a mirror containing an exploitable phase feature that facilitates dispersion compensation in a Cr: LiSAF laser cavity. Mirror designs developed as part of this project allowed for the construction of a Ti: sapphire laser having a high pulse repetition frequency (described in chapter 4).

The project work presented in chapter 3 deals with the design of a birefringent filter as a tuning element for a low-gain Cr: LiSAF femtosecond laser. This filter was used in conjunction with MCGTI mirrors provided by Prof. Robert Szipocs (*R&D Lezer-Optika Bt., Budapest*) to develop a femtosecond laser with a centre wavelength tunability of 20nm that did not rely on the use of intracavity prisms. This same filter was used to constrict the oscillating bandwidth of the laser system and thus provide a degree of control over the output pulse durations.

Chapter 4 describes the implementation of high repetition-rate femtosecond laser oscillators based on the Cr: LiSAF and Ti: sapphire gain media. A detailed analysis of instabilities caused by low pulse energies is presented and used to determine the optimum laser parameters for high repetition-rate operation. A repetition rate of over 1GHz (146fs pulses) is achieved from a diode-pumped

femtosecond Cr: LiSAF laser and a repetition rate of 2.3GHz (240fs pulses) is achieved from a modelocked Ti: sapphire laser incorporating the dispersion-compensating mirrors developed as part of the project material detailed in chapter 2.

The development of a Ti: sapphire laser with a low threshold incident pump power is described in chapter 5. This laser produced 80mW of total average output power in the form of bandwidth-limited 75fs pulses for just 1W of incident pump power. The computer modelling described in chapter 4 is adapted to consider such important factors as crystal selection, pump/laser mode overlap and delivery of sufficient fluence to a saturable absorber to both initiate and sustain modelocking.

Chapter 6 presents the results of a series of experiments using an electrically-pumped vertical extended-cavity surface emitting laser (VECSEL) as a saturable absorber modelocking element. Through current injection, a degree of control over the pulse formation process was observed. Although the pulsed output of the laser was limited to several hundred picoseconds, this work is seen as a first-step on the way to locking ultrashort optical pulses to an electrical clock signal.

In chapter 7 the major conclusions drawn from previous chapters are presented. Ideas for future work as a continuation of this project are also outlined.

Contents

Chapter 1 Introduction and General Background	1
1.1 General Introduction	1
1.2 Pulse propagation	2
1.3 Modelocking with saturable absorber mirrors	11
1.4 Measurement of ultrashort optical pulses	18
1.5 Conclusions	23
References	25
 Chapter 2 Dispersion of multilayer dielectric mirrors	
measurement and analysis	30
2.1 Introduction	30
2.2 Measurement of dispersion	30
2.2.1 Interferometric and intracavity dispersion measurement techniques	31
2.2.2 Motivation and measurement of the dispersion of multilayer mirrors using white light interferometry	32
2.2.2.1 Motivation	32
2.2.2.2 Dispersion measurement using White light interferometry	33
2.3 Analysis and design of dispersive mirrors	38
2.3.1 Introduction	38
2.3.2 Gires-Tournois interferometer mirrors and multiple-cavity Gires-Tournois interferometer mirrors	38
2.3.3 Chirped mirrors as a source of negative dispersion	44
2.3.4 Design of a dispersive mirror for use in high repetition rate Ti: sapphire lasers	45
2.3.4.1 Introduction	45
2.3.4.2 The LTR method	46

2.3.4.3 GTI mirrors for high repetition-rate Ti: sapphire lasers	50
2.4 Conclusions	54
References	56
 Chapter 3 Tuning of compact Cr: LiSAF lasers using a novel birefringent filter	
3.1 Introduction	58
3.2 Three techniques for tuning a modelocked laser	58
3.3 Tuning using a birefringent filter and multiple-cavity Gires-Tournois interferometer mirrors	63
3.3.1 Introduction: how tunability and negative GDD is achieved	63
3.3.2 Modelling of the filter using Jones matrix algebra	64
3.3.3 Conclusions	71
3.4 Steeply diving optic axis birefringent filter as an intracavity tuning element	71
3.4.1 Tuning of a cw laser	72
3.4.2 Tuning of a modelocked laser	75
3.4.2.1 Preliminary work on tuning of a modelocked laser	75
3.4.2.2 Tuning the ‘double-pumped’ Cr:LiSAF laser	77
3.5 Conclusions	81
References	82
 Chapter 4 High repetition-rate near infra-red femtosecond Lasers	
4.1 Introduction	84
4.2 Avoidance of Q-switched modelocking	85
4.3 Construction of an efficient laser	89
4.4 1GHz repetition-rate Cr: LiSAF laser	95
4.5 High repetition-rate Ti: sapphire lasers	97

4.5.1 Initial investigations of Ti: sapphire lasers: 500MHz repetition-rate	97
4.5.2 ~1GHz Ti: sapphire laser	103
4.5.3 >2GHz Ti:sapphire laser	108
4.6 Conclusions	110
References	111
Chapter 5 Low-threshold Ti: sapphire lasers	112
5.1 Introduction	112
5.2 Modelling and optimisation of low-threshold Ti: sapphire lasers	113
5.3 Experimental realisation of a low-threshold, SESAM Modelocked Ti: sapphire laser	118
5.3.1 Assessment of a cw system	118
5.3.2 Assessment of the modelocked laser system	122
5.4 Ti: sapphire laser pumped with miniature green laser	124
5.5 Conclusions	127
References	128
Chapter 6 Modelocked Ti: sapphire laser using a VECSEL as a saturable absorber device	129
6.1 Introduction	129
6.2 Vertical extended cavity surface emitting lasers – a background	130
6.3 Ti: sapphire laser operating beyond 900nm	133
6.3.1 Introduction	133
6.3.2 Design of the “>900nm Ti: sapphire laser”	133
6.4 Ti: sapphire laser using a VECSEL as a saturable absorber	136
6.4.1 Initial investigations	136
6.4.2 ‘Switchable’ pulses using pulsed incident current	142
6.5 Conclusions	144
References	146

Chapter 7: Conclusions and Future work	147
Acknowledgements	152

Chapter 1 - Introduction and General Background

1.1 General Introduction

Conceptually, it is nontrivial to understand just how short optical pulses produced by modern ultrafast lasers can be. Pulses as short as 10fs ($1\text{fs} = 1 \times 10^{-15}\text{s}$) can be produced directly from optimised broadband laser oscillators. Over the years, several analogies have been made to illustrate the timescales involved. One such analogy that goes some way to indicating this is that ‘there are the same number of femtoseconds in one second as there are seconds in thirty-two million years’.

Although the underlying physical mechanisms for the generation of ultra-broadband continua in photonic crystal fibre (PCF) are still the subject of debate, the experimental realisation of a white-light continuum with good spatial properties would not be possible without ultrashort-pulse lasers [1]. This phenomenon has driven a renaissance in many fields in the last few years. Among these are microscopy [2], and ultra-high resolution optical coherence tomography (OCT). OCT uses a series of laterally adjacent depth scans to build up a cross-sectional image [3, 4]. Broadband continua have also been generated at repetition-rates of 1GHz [5]. This high repetition-rate, coupled with the broad frequency bandwidth, may yet prove useful in data communications where wavelength division multiplexing (WDM) and optical time division multiplexing (OTDM) have the potential to allow very high rates of data transfer [6].

Femtosecond laser pulses may also be used to produce even shorter extreme ultraviolet or X-ray pulses through high harmonic generation [7]. Incident light can excite electrons from their natural position in an atom. Attractive forces then act to restore these electrons back to their original position. This results in the electrons shedding energy in the form of X-rays, which are harmonics of the incident light. Researchers have measured the duration of these X-ray pulses [8] and found them to be several hundred attoseconds (10^{-18}s) long and have also been able to use such pulses to monitor and control molecular and electronic motion [9, 10].

With these two, very different, applications of femtosecond laser systems in mind, it is easy to see why ultrafast laser science is such a hot bed of research. The following sections of this chapter will deal with femtosecond pulse propagation, generation, and measurement. It will also put the project work discussed in later chapters in the context of up-to-date research in laser and optical physics.

1.2 Pulse propagation

The most common approximation made when describing an optical pulse mathematically is to assume that the envelope, $\varepsilon(t)$, of the pulse varies slowly with respect to the carrier frequency, ω_0 . This is known as the slowly varying envelope approximation (SVEA) [11]. The electric field as a function of time, $E(t)$ can then be written as:

$$E(t) = \varepsilon(t)e^{i\phi(t)}e^{-i\omega_0 t} \quad (1)$$

where $\varepsilon(t)$ is the time-varying function which describes the electric field envelope, and $\phi(t)$ is the temporal phase variation across the pulse. The pulses referred to in this thesis are usually assumed to have hyperbolic secant temporal envelope functions [11] and these may be represented by:

$$\varepsilon(t) = \varepsilon_0 \operatorname{sech}\left(\frac{1.763t}{\Delta\tau_p}\right) \quad (2)$$

where ε_0 is the electric field amplitude and $\Delta\tau_p$ is the full width at half maximum (FWHM) of the pulse.

The corresponding spectral components of this optical pulse can be found by taking the Fourier transform of the temporal description given in equations 1 and 2. The fundamental dependence of the pulse spectrum on its temporal components gives rise to the bandwidth theorem that states that a given pulse duration requires a minimum spectral bandwidth required to support it. This can be expressed as:

$$\Delta\nu\Delta\tau \geq X \quad (3)$$

where X is a constant that depends on the pulse shape, $\Delta\nu$ is the FWHM frequency bandwidth associated with the pulse, and $\Delta\tau$ is the FWHM temporal duration of the pulse. For a sech^2 pulse intensity profile, such as that described in equations 1 and 2, the value of X is 0.315. When a pulse exhibits a frequency chirp it means that the spectral components making up the pulse arrive at different times, such that the pulse duration increases. This has the net effect of increasing the value of X and so the pulse duration has been increased through some physical mechanism but the frequency bandwidth has remained unaltered. For most optical materials the resonances of absorption can be found in the ultraviolet region of the optical spectrum. These resonances give rise to a refractive index change with respect to frequency that will temporally broaden the pulse, due to a frequency-dependent phase velocity. Many resonances are usually present in an optical medium and are often described in terms of an empirical Sellmeier equation, as shown in equation 4.

$$n^2 - 1 = \sum_j \frac{A_j}{\omega_j^2 - \omega^2} \quad (4)$$

The parameters A_j and ω_j have been tabulated for a wide range of materials. These resonances create a dispersion relation such that both the phase velocity and group velocity associated with a wavepacket become functions of frequency. This, in turn, means that an optical pulse will change its shape as it propagates.

A short pulse can be thought of as a series of spectrally-narrow long pulses summed together coherently. It is therefore more intuitive to discuss dispersion as a frequency-dependent phase difference between spectral components. Siegman [11] shows that this spectral phase function can be approximated by a Taylor series expansion:

$$\phi(\omega) = \phi_0 + \sum_n \frac{1}{n!} \phi_n(\omega_0) (\omega - \omega_0)^n \quad (5)$$

where ϕ_n is the n^{th} derivative of the spectral phase function evaluated at reference frequency ω_0 . The quantity determined by each individual differentiation is measured in fs^n and the physical interpretation of each of these terms will now be discussed: The absolute phase, ϕ_0 , is the phase accumulated at the carrier frequency and is related to the phase velocity through the relation:

$$v_\phi = L \left(\frac{\omega_0}{\phi_0} \right) \quad (6)$$

This is the speed at which the central carrier frequency propagates through a medium of length L .

The second term, defined as group delay and is related to the group velocity of the wavepacket through a medium of length L through the relation:

$$v_g = L \left(\frac{d\omega}{d\phi} \right) \quad (7)$$

The lowest-order term that can be considered useful within the context of this thesis is $\phi_2(\omega_0)$, which is the group delay dispersion (GDD). The terms ‘positive’ and ‘negative’ dispersion relate to the sign of this quantity. It is measured in fs^2 and is the rate at which a pulse centred on the reference frequency will increase in duration as it propagates through the system. It should be noted that although the terms group delay dispersion and group velocity dispersion (GVD) are sometimes used interchangeably, they are quite different. In a system where higher-order dispersion terms can be neglected, Walmsley et al. [12] have shown that an incident transform-limited Gaussian pulse with initial duration, τ_1 , centred at frequency, ω_0 , will exit the medium having had its duration broadened to a value τ_0 , given by:

$$\tau_0 = \tau_i \sqrt{1 + \frac{16(\ln 2)^2 (\phi_2(\omega))^2}{\tau_i^4}} \quad (8)$$

[Higher-order differentiations are termed third-order dispersion (TOD), fourth-order, etc. and are only important as the pulse duration becomes shorter and where the lower-order terms are small]

The sign of the GDD is important because it indicates the order in which the frequency components will exit the dispersive system. If the sign is positive then the frequency components of the pulse will exit with the shorter wavelength components trailing the longer (sometimes this is termed ‘up-chirp’) and vice versa if the sign is negative. This can be seen in figure 1.1 where heavily ‘up-chirped’, ‘down-chirped’, and unchirped 10fs Gaussian pulses have been plotted.

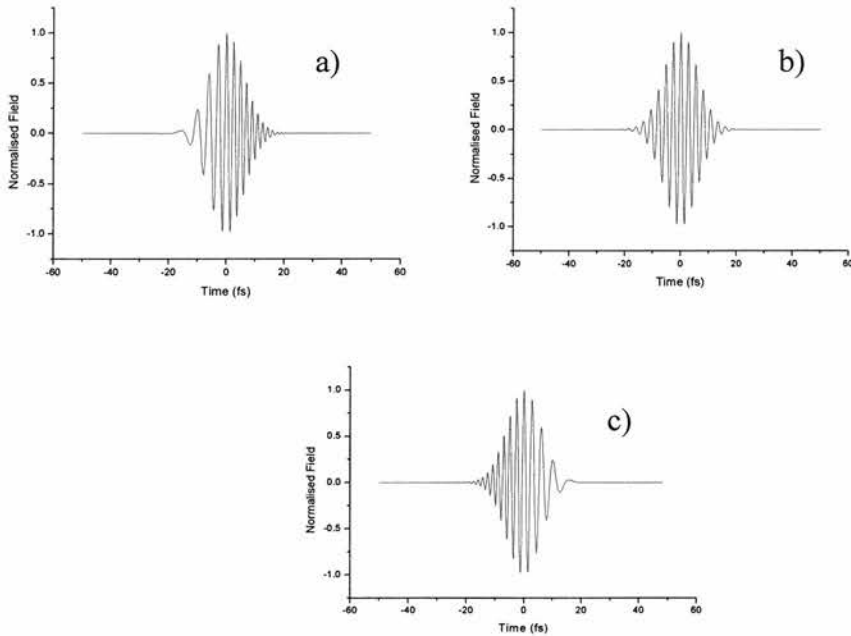


Figure 1.1: Plots of 10fs Gaussian pulses centred on 800nm with a) positive or up chirp, b) transform-limited (no chirp), and c) negative or down chirp

The transform-limited pulse in figure 1.1 b) cannot be made shorter, whereas by contrast if all the frequency components in figure 1.1 a) and figure 1.1 c) arrived simultaneously then the pulses would be significantly shorter.

As a pulse traverses an optical system which has non-zero GDD, the pulse will change shape. For many practical applications it is vital to have control of the induced frequency chirp of an optical pulse. For many laser crystals the sign of GDD is positive, and hence arrangements providing negative GDD are required in order to compensate for the resulting temporal broadening. There are many geometrical systems containing a number of prisms that can compensate for positive GDD in this way. One such system involves the use of two prisms [13-16] as indicated in figure 1.2. Two prisms are orientated such that they are opposing each other and such that both provide minimum deviation. The prisms are cut at Brewster's angle in order to minimise reflection loss. The chromatic dispersion relating to the refractive index of the prism material leads to a geometrical dispersion of the broadband input light. In the optical region of the spectrum, longer wavelengths of light travel a shorter path in air than the shorter wavelengths. In the material longer wavelength components travel longer paths, so by adjusting the separation of the prisms and the prism material traversed these two effects can be made to compensate each other. The total dispersion of the entire prism system can thus be adjusted to take either positive or negative values.

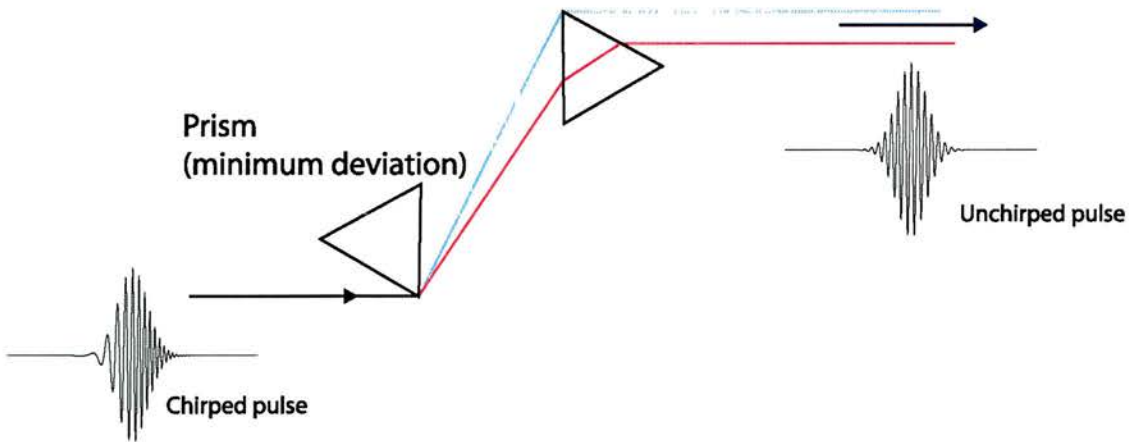


Figure 1.2: Arrangement of two prisms that provides negative group delay dispersion

Changing the prism insertion and path length between the prisms can alter the magnitude of the dispersion offered by the prism arrangement. Using such an arrangement, pulses as short as 11fs have been generated directly from a laser oscillator [17]. Higher orders of dispersion are the main challenge when it

comes to generating very short pulses using a laser that incorporates intracavity prisms. Analytical expressions exist which allow these higher orders to be calculated for arbitrary sequences of prisms [18]. However, removing this higher order dispersion entirely still remains a significant resonator design issue and is one of the main difficulties in generating optimally short pulses.

As can be seen in figure 1.2, intracavity prisms introduce large amounts of spatial dispersion in order to compensate for temporal broadening of the optical pulse [19]. This has the advantage that the oscillating bandwidth and centre wavelength of the laser can be selected through the incorporation of an intracavity slit. However, for many applications the induced spectral shear across the pulse is unacceptable. Mirror-based dispersion compensation schemes do not impose such a spectral shear across the laser beam and can also compensate for higher-order dispersive effects. These schemes are discussed fully in chapters 2 and 3 of this thesis. These chapters show that mirror-based dispersion compensation schemes can be specifically designed to achieve a particular laser output. Chapter 3 of this thesis details the successful use of a birefringent plate as a frequency selective element in a compact femtosecond laser, thus showing that lasers utilising mirror-based dispersion compensation schemes can still be tunable. Chapter 4 explains that the repetition-rate of a femtosecond laser can be significantly increased if the intracavity mirrors are correctly designed. The project work detailed in later chapters shows that a degree of adaptability, which cannot be achieved with prisms, is available with mirror-based dispersion compensation schemes.

An ultrashort optical pulse can induce a number of nonlinear effects as it propagates through a medium. The main mechanism relevant to pulse propagation through a dielectric medium is the optical Kerr effect. The optical Kerr effect produces, at sufficiently high intensity and assuming an instantaneous response of the medium, intensity-dependent refractive index changes. In a centro-symmetric laser medium the polarisation response can be approximated by,

$$P = \epsilon_0 \chi_1 E + \epsilon_0 \chi_3 E^3 \quad (9)$$

However, it is well known that

$$\chi_1 = n^2 - 1 \quad (10)$$

and so the following can be postulated

$$\chi_1 + \chi_3 E^2 = n^2 - 1 \quad (11)$$

Here n' is the refractive index which has been modified by the incident intense electric field. The authors of reference [20] show that this can be rewritten as:

$$n' = n + n_2 I(r, t) \quad (12)$$

where n_2 is the intensity-dependent component of refractive index measured in W^{-1}m^2 . The dependence of this intensity function has been written explicitly because the spatial component gives rise to self-focussing and the temporal component to a self-phase modulation effect.

An incident pulse having a spatially varying intensity profile can induce spatially varying refractive index changes in the laser crystal of a resonator, and thereby creates a weak ‘dynamic’ lens. This can be illustrated as in Figure 1.3, where n_2 is assumed to be a positive quantity.

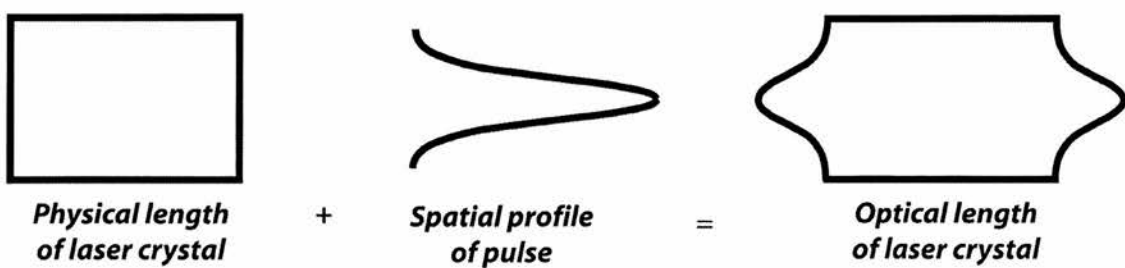


Figure 1.3: The effect of the spatial dependence of refractive index arising from the optical Kerr effect.

This effect of creating a lens in the gain medium has important consequences for the propagation of ultrashort pulses [21, 22], and self-focussing is also the

mechanism responsible for the break up of optical pulses in high power lasers and amplifiers.

Self-phase modulation or ‘SPM’ is another important consequence of the optical Kerr effect. If the refractive index change is instantaneous as the pulse propagates through the medium, there will be a component of the refractive index having a temporal dependence that follows the intensity profile of the optical pulse. This will manifest itself as a nonlinear phase change. Assuming that the pulse does not change shape as it propagates through the nonlinear medium there will be an induced phase change across the temporal profile of the pulse given by [20],

$$\phi(t) = \frac{L\delta n\omega_0}{c} \quad (13)$$

Where L is the length of the nonlinear medium, δn is the change in refractive index associated with the time-dependent intensity profile, ω_0 is the carrier frequency and c is the speed of light.

However, given that,

$$\delta n = n_2 I(t), \quad (14)$$

and that

$$\delta\omega = \frac{d\phi}{dt}, \quad (15)$$

it follows that this phase change will result in a change of frequency given by,

$$\Delta\omega = \frac{-2\pi L n_2}{\lambda} \left(\frac{dI(t)}{dt} \right) \quad (16)$$

This phase shift and subsequent spectral broadening is shown schematically in figure 1.4

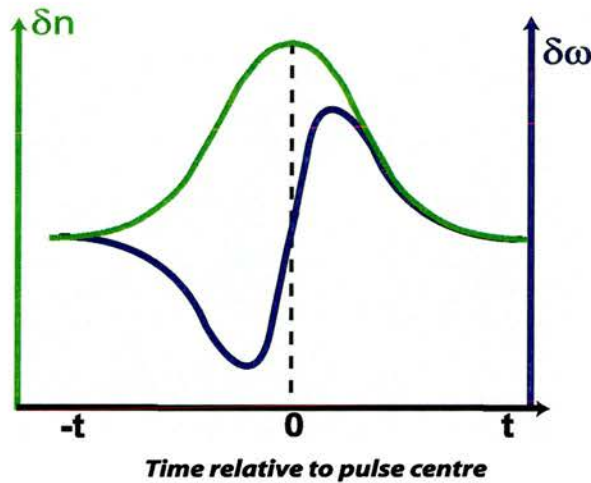


Figure 1.4: Schematic indicating how spectral broadening can arise from self phase modulation in a gain medium.

The features of the instantaneous frequency shift, $\Delta\omega$, shown in figure 1.4 imply there is a positive frequency chirp around the centre region of the pulse. SPM must be compensated in a similar way to linear chirp by using the techniques outlined earlier in this chapter. Self-phase modulation is useful because it induces an exploitable spectral broadening of the pulse. Thus, if the laser can be operated in a regime with zero net dispersion then optimally short pulse durations can be obtained. The combined action of self-focussing and self-phase modulation can provide preferential gain for a high intensity pulsed laser mode rather than low intensity cw oscillation [23]. This technique, where the gain medium provides an artificial saturable absorber, is called Kerr-lens modelocking (KLM) or self-modelocking. The stability of this pulsed operation can be enhanced through exploiting an intracavity soft [24] or hard aperture [25]. However, to maintain sufficient intensity to fully exploit this effect the laser cavity is usually operated near the edge of its stability range. This ensures that the laser mode is focussed very tightly within the gain medium. Operation of a laser near the edge of its stability range results in a system that is susceptible to external perturbations and requires accurate alignment procedures. Although the lasers developed as part of this project were not deliberately designed to fully exploit the optical Kerr effect, the combined effects of self-phase modulation and self-focussing still play a role in the formation and

stabilisation of the optical pulse. The lasers developed during the course of this project relied on the use of an intracavity saturable absorber mirror for modelocking, as described in the next section.

1.3 Modelocking with saturable absorber mirrors

For broadband lasers, the output will not be monochromatic but will contain a series of very closely spaced longitudinal modes, with a spectral separation of,

$$\Delta\nu = \frac{c}{L_{\text{eff}}} \quad (17)$$

Here c is the speed of light and L_{eff} is the effective optical length of a round-trip of the laser cavity. If these oscillating modes can be phase-locked together, then as justified by Fourier theory, a periodic train of very short pulses will be emitted by the laser. Phase locking can be achieved by using a periodic perturbation that originates outside the laser cavity, so-called ‘active modelocking’ [26]. This can be done through synchronous pumping [27], gain modulation [28], or through the use of acoustic [29] or electro-optic modulators [30].

Modelocking can also be achieved using the fluctuating intracavity intensity to achieve self amplitude modulation (SAM) [29]. Any technique relying on the intracavity radiation controlling the modelocking mechanism is termed ‘passive modelocking’. The lasers developed as part of this project used an intracavity mirror to initiate the SAM required for stable passive modelocking. Two terminologies are used for the types of semiconductor absorber mirrors typically used for modelocking. These are: (i) the semiconductor saturable absorber mirror (SESAM) [31] and (ii) the saturable Bragg reflector (SBR) [32]. These two types of saturable absorber mirror are shown in figure 1.5. The anti-resonant Fabry-Perot saturable absorber (A-FPSA), a type of SESAM, is shown in the lower diagram and the SBR is shown in the upper diagram. An A-FPSA is used to modelock the lasers discussed in chapters 3, 4, and 5 of this thesis and an SBR is used to modelock the lasers described in chapter 4. The SESAM structure consists of a Bragg mirror followed by a half wavelength layer into

which an absorber has been grown, typically in the form of a single quantum well. The SBR, on the other hand, is simply a series of quarter wavelength layers operating as a high reflector that contains a single quantum well within the final quarter wavelength layer. The SESAM shown in figure 1.5 is operated at anti-resonance to ensure broadband reflectivity and low GDD in reflection, whereas the SBR has sharper associated spectral features. As the quantum well is positioned within a half-wavelength layer in the case of the A-FPSA a degree of control over the saturation parameters, not possible with the SBR structure, is available.

The SESAM absorber layer tends to be grown at a low temperature (~ 300 degrees Celsius), whereas the SBR is grown at significantly higher, more conventional temperatures. This has significant implications for the spectral and temporal response of the modelocking element but this difference in response is related to the growth temperature and not to the structure of the device, so classification in terms of structure can in some ways be rather misleading.

Bleaching of a semiconductor saturable absorber is controlled by both the duration and intensity of the incident pulses, the recovery of such a device is governed purely by the carrier dynamics in the absorber. This will result in a bitemporal response with an initial fast component, due to intraband thermalisation (~ 100 femtoseconds), and a slow response due to interband trapping and recombination (picosecond to nanosecond scale) [33]. This combination of slow and fast recovery times allows for the generation of femtosecond pulses. In general, the fast recovery time controls the pulse shaping, and the slow recovery time aids in the establishment of modelocking. There are several different modelocking theories that describe pulse formation in lasers using SESAMs and SBRs. Each theory places a different emphasis on each component of the bitemporal response. Some of these theories are SESAM-assisted Kerr-lens modelocking, fast saturable absorber modelocking, and soliton modelocking.

Kerr-lens modelocking is usually regarded as a fast saturable absorber technique because the intracavity loss changes nonlinearly with intensity, and so the net gain window is of the order of the duration any pulse that is formed. The time taken for a pulse to develop from noise is known to be inversely proportional to the final pulse duration; this has the implication that any system producing

pulses which last several femtoseconds is unlikely to be self-starting. This means that such a laser cavity must be subject to an external perturbation to initiate modelocking. This perturbation subsequently plays no further part in the pulse formation such that the KLM process can be free to form the shortest pulses. The ‘slow’ component of the bitemporal response of an SBR/SESAM device is ideal for this purpose. However, the device must have suitably broadband reflectivity to allow the bandwidth required for these ‘hypershort’ pulses to oscillate. The authors of reference [34] show how gold can be integrated into the mirror structure to ensure broadband reflectivity.

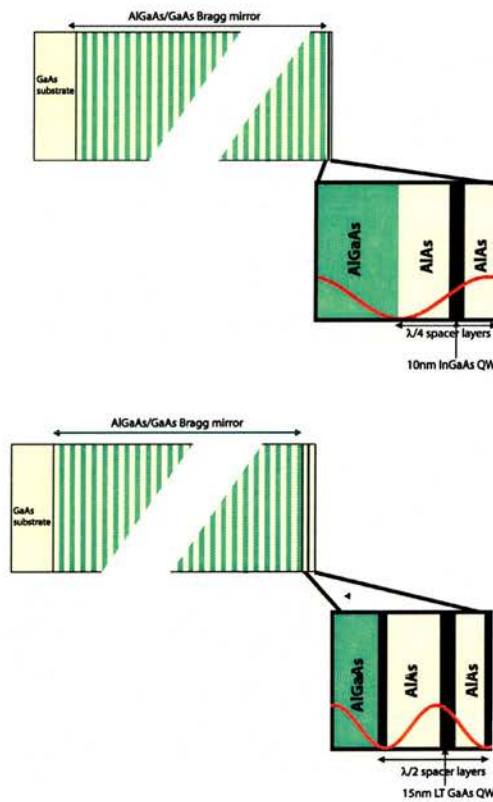


Figure 1.5: Diagram showing the structure of a high-temperature grown SBR (upper), and a SESAM where the absorber layer has been grown at a lower temperature (lower). Red lines indicate the induced standing-wave electric field distribution.

In fast saturable absorber modelocking theories the recovery time of the absorber plays an important role in the shaping of the pulse [35]. A schematic showing the gain and loss characteristic of a laser containing a fast saturable absorber can be seen in figure 1.6.

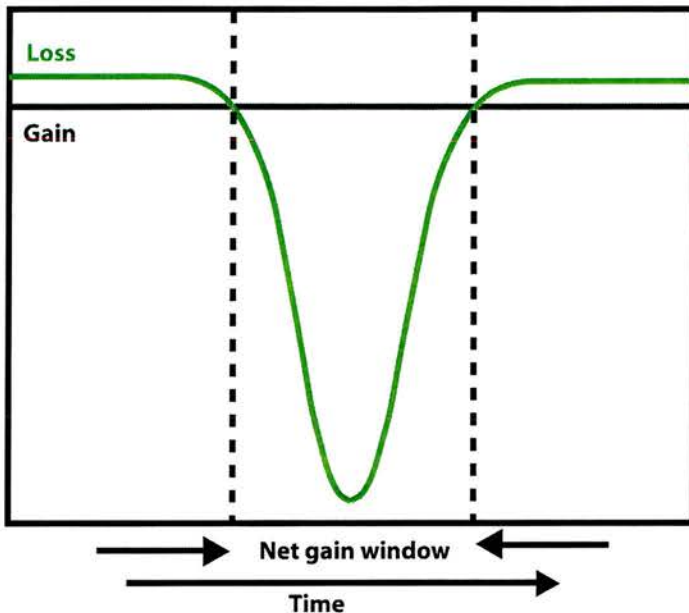


Figure 1.6: Schematic showing the action of a saturable absorber under conditions of fast saturable absorber modelocking

From reference [32] it is deduced that modelocking results when the net gain window occurs during the fast response of the saturable absorber. The major limitation of relying on the fast component of the absorption is the tunability of the response. The authors of reference [32] indicated that the centre wavelength of their laser was tunable over 20nm and their measurements on the modelocking element suggest that the fast component of the nonlinearity was at its strongest over this wavelength range. Conversely the authors of reference [36] demonstrate a laser where the centre wavelength of the laser was only tunable over a few nanometres. This narrow tunability is due to the use of Gires-Tournois interferometer (GTI) mirrors for dispersion compensation. As discussed more fully in chapter 2, these mirrors offer negative dispersion but it extends over a relatively limited spectral range.

The spectral and temporal response of a saturable absorber can be altered using low temperature growth. The A-FPSA used to modelock the lasers discussed in chapters 3, 4, and 5 was grown at 300 degrees Celsius. This SESAM structure had been used previously to modelock a Cr: LiSAF laser producing 45fs pulses

with a centre wavelength tunability of 50nm [37]. This tunability was limited by the reflectivity of the back mirror of the modelocking element and not on the saturable absorption. These results show that the fast response of the absorber is not responsible for the pulse shaping in this laser, as this tunability would not be expected from a saturable absorber utilising the fast component of the response. Keller and co-workers explained the pulse stabilisation process in this laser as an incidence of ‘soliton modelocking’[38]. In much the same way as described earlier for SESAM-assisted KLM operation, this process is started by the bleaching and subsequent recovery of the saturable absorber. After the pulse formation has been initiated by the slow response of the absorber the interplay between SPM and GDD in the laser cavity stabilises the pulse. This is very similar to the effects responsible for a ‘dispersion managed’ soliton in which the spectral broadening and negative group delay dispersion occur in discrete locations. This ‘dispersion managed’ soliton is not as fragile as a classical soliton, such as that described by the authors of [39], which cannot cope with large changes in pulse shape from the SPM and GDD present in the laser cavity. When utilising a SESAM to initiate soliton modelocking the main purpose of the modelocking element is to distinguish between a cw or long pulse regime and a short pulse regime. This long pulse, in the nanosecond regime, is what is known in soliton theory as the ‘continuum’. The continuum pulse will see higher gain than the ultrashort pulse due to the lack of gain dispersion. The purpose of the saturable absorber is to destabilise this long pulse and so prevent it from reaching threshold, since its recovery time is in the picosecond regime. In other words, the SESAM is simply present to start and stabilise modelocking through self-amplitude modulation. The shaping of the optical pulse is then due to SPM and GDD [40, 41]. The action of the SESAM can be seen schematically in figure 1.7.

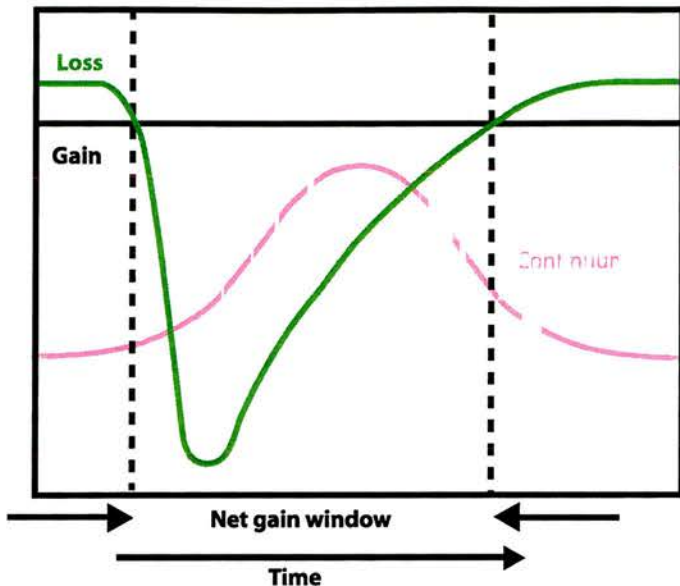


Figure 1.7: Schematic showing the action of a saturable absorber under conditions of soliton modelocking

Although the soliton modelocking theory describes the stabilisation of bandwidth-limited pulses in a laser very well, it lacks consideration for pulse-shaping from the fast component of the saturable absorber. It also lacks consideration for higher-order dispersion terms that will become more important as the pulse duration becomes shorter. A theory to rigorously describe the mechanisms responsible for pulse formation and stabilisation in SESAM-modelocked lasers is still the topic of ongoing research.

From a laser engineering perspective it is important to understand what the main operating parameters of a SESAM are, and what implications these parameters will have when such an absorber is incorporated into a laser. The key parameters are:

- 1.Recovery time
- 2.Modulation depth and non-saturable loss
- 3.Saturation fluence

The bitemporal recovery time of a typical saturable absorber has already been described in this chapter when making the distinction between fast saturable absorber modelocking and soliton modelocking theories.

The modulation depth of a saturable absorber, usually represented by ΔR , is simply the amount of loss that can be bleached in the saturable absorber. Across a range of modelocking theories it has been shown that the minimum achievable pulse duration with any laser system is inversely proportional to the modulation depth of the absorber used. In references [42] and [41] the authors show that the minimum pulse duration possible from a laser is given by the reciprocal of the modulation depth raised to some power, where the power depends on the details of the model used. So one might expect ΔR to be made as large as possible as it also encourages self-starting operation [33]. However, if it is made too large the laser will lapse into Q-switching instabilities [43]. A more thorough investigation of this particular instability is given in chapter 3.

The non-saturable loss, ΔR_{ns} , is simply the residual loss exhibited by the device after it has been bleached. This will depend on the device structure and on the specific growth parameters. For instance, a device grown at high temperatures (e.g. reference [44], will exhibit less non-saturable loss than the same device grown at low temperatures (e.g. reference [31]). The non-saturable loss and modulation depth can be seen more clearly in figure 1.8 where the reflectivity of such a device is shown schematically as a function of incident pulse fluence.

The saturation fluence is the pulse fluence (energy per unit area) that is required to be incident on the absorber such that the reflectivity is altered by an amount equal to the modulation depth multiplied by $(1-e^{-1})$. The saturation fluence should be sufficiently small to allow operation under conditions of complete saturation. Operation at full saturation will minimise the residual loss in the cavity from the modelocking element.

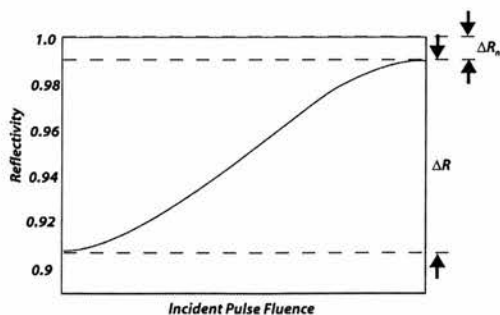


Figure 1.8: Diagram showing the response of the saturable absorber under increasing pulse fluence. Shown are the important parameters modulation depth, ΔR , and non-saturable loss, ΔR_{ns} .

There is a limit to how small the saturation fluence can be made. If the incident pulse fluence is too high in comparison to the saturation fluence then the laser will operate in a multi-pulse regime where there is more than one pulse present in the cavity. This is because if the transition from single pulse to multi-pulse operation does not significantly alter the level of saturation on the absorber then multi-pulse operation will be favoured [33]. The saturation fluence condition can be easily met by altering the radius of the laser spot incident on the saturable absorber.

Pulses originating from a passively modelocked laser cannot presently be locked to an electrical clock signal. Realisation of this will be important for many systems applications because the electronics used to encode information on an optical pulse train require such a signal. The results presented in chapter 6 of this thesis show that a degree of control can be maintained over the pulse formation process through injection of an electrical current to the saturable absorber. This is seen as a first step towards the locking of ultrashort optical pulses to an external clock signal.

1.4 Measurement of ultrashort optical pulses

Throughout the project work detailed in this thesis, the technique of 2-photon autocorrelation is used to infer the duration of the pulses produced by laser oscillators. Direct measurement of an ultrashort optical pulse through comparison with a smaller quantity is impossible, so the overlap of the pulse with itself is used to infer the pulse duration [45]. The scheme typically used to measure the autocorrelation is shown in figure 1.9. The pulse intensity is separated into two replicas. The moving mirror that forms one end of the Michelson-type delay line scans the relative overlap between the two sub-components.

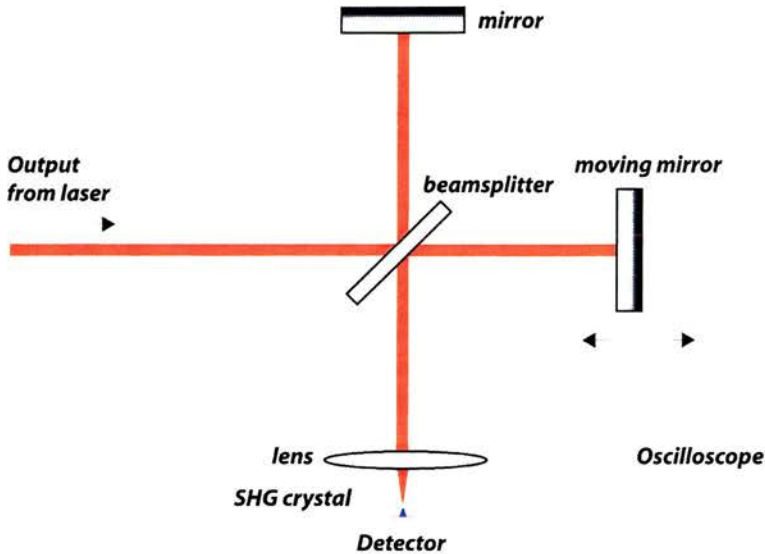


Figure 1.9: Schematic showing the optical scheme of an autocorrelator setup.

The field generated in the crystal will have a quadratic dependence on intensity if the pulses are overlapped. If the detection system is fast enough to resolve the periodic oscillations originating from the central carrier frequency then the signal measured at the detector will be given by:

$$g(\tau) = \frac{\int_{-\infty}^{\infty} ((E(t) + E(t + \tau))^2)^2 dt}{2 \int_{-\infty}^{\infty} |E(t)|^4 dt} \quad (18)$$

This is called the fringe resolved, or interferometric autocorrelation. If the detection system is not fast enough to resolve this periodic oscillation then the time-averaged, or intensity autocorrelation will be recorded, this has the form:

$$G(\tau) = 1 + \frac{2 \int_{-\infty}^{\infty} I(t)I(t - \tau)dt}{\int_{-\infty}^{\infty} I(t)^2} \quad (19)$$

$E(t)$ in equation 19 is the mathematical description of the optical pulse given in equation 1 and $I(t)$ in equation 20 is its associated intensity. Calculated intensity

and interferometric autocorrelation functions of 10fs Gaussian pulses are shown in figure 1.10.

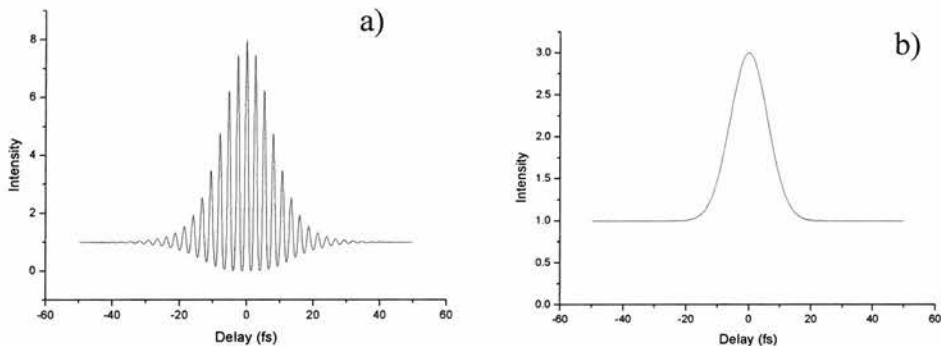


Figure 1.10: Interferometric autocorrelation (a), and intensity autocorrelation (b), of 10fs Gaussian pulses

Provided the pulse being measured is nearly transform limited, the interferometric autocorrelation trace is self-calibrating because the time period between each fringe is well-defined (2.67fs for a pulse centred at 800nm). As can be seen from the plot in figure 1.10 (a), the maximum value of the autocorrelation function is 8 and is found when the relative delay between the two pulses, τ , is equal to zero. The autocorrelation function tends to equal 1 when τ tends to $+\/- \infty$, i.e. delays that are long compared to the pulse duration, and so this means that the autocorrelation trace has a contrast ratio of 8:1. Similarly, figure 1.10 (b) shows that the ideal contrast ratio for the intensity autocorrelation is 3:1. The intensity autocorrelation is not self-calibrating and so accurate measurement of the signal relies on translation of one of the mirrors to calibrate the measurement system in space, and therefore time.

To calculate the pulse duration from the autocorrelation a pulse shape must be assumed. This is because the actual pulse duration is equal to the duration of the autocorrelation trace divided by a pulse shape dependent conversion factor. This factor provides the relationship between the FWHM of the autocorrelation and the pulse duration. Table 1.1 outlines the conversion factors for Gaussian and sech^2 pulse profiles along with the time bandwidth product associated with each pulse shape.

Pulse Profile	Conversion factor (interferometric)	Conversion factor (intensity)	Time/bandwidth product ($\Delta\nu\Delta\tau$)
Gaussian	1.697	1.414	0.441
Sech ²	1.897	1.543	0.315

Table 1.1: Conversion factors and time/bandwidth products for Gaussian and sech^2 temporal profiles.

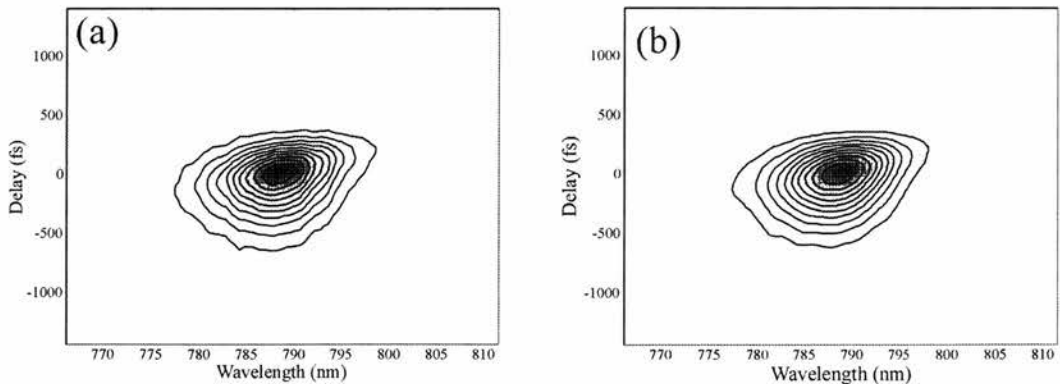
For chirped pulses the electric field envelopes will only interfere with each other perfectly at the centre of the trace, when $\tau = 0$. This implies that the interferometric autocorrelation does contain some phase information and attempts have been made to retrieve this information [46]. However, these techniques are susceptible to experimental error because it is difficult to infer direct pulse durations from the interferometric trace due to the envelope distortion in the pulse arising from frequency chirp. The intensity autocorrelation contains no phase information but is not susceptible to pulse distortion. It is for this reason that the intensity autocorrelation is used throughout this thesis to infer the duration of optical pulses.

Recent developments have helped reduce the complexity and cost of a typical autocorrelator setup. In particular, the combination of a photomultiplier tube and a SHG crystal can be replaced with a semiconductor device, such as a laser diode or light emitting diode (LED) [47]. If the energy of the incident photons is greater than the energy associated with the bandgap then the induced photocurrent follows a near linear dependence on the incident pulse intensity. In contrast, when the photon energy is less than the bandgap energy a two-photon absorption process occurs. Given that this two-photon absorption process has a quadratic dependence on intensity this detector arrangement is rendered ideal for large bandwidth optical pulses. This detector arrangement is also polarisation insensitive and immune to other effects such as group velocity mismatch [48]. A detector based around this two-photon absorption process was used throughout

this project as it provided the simplest, most cost-effective way of inferring the duration of the femtosecond optical pulses.

With the pulse spectrum and autocorrelation measured, the pulse is still not fully characterised. If the pulse is chirped it may be important to know the degree of the frequency chirp. An aspect of ultrafast diagnostics has opened up relatively recently where the objective is to provide a more comprehensive characterisation of ultrashort optical pulses. One of the most influential pieces of work into the full characterisation of ultrashort optical pulses was due to Trebino and co-authors [49-51]. These researchers realised that if the autocorrelation function of an ultrashort laser pulse could be spectrally resolved to produce a two-dimensional spectrogram, a computational procedure could be introduced to retrieve the spectral phase of the pulse. This technique is known as a frequency-resolved optical gating (FROG) process.

Another spectrogram-based technique exists, which is perhaps rather more intuitive in its resulting spectrogram, and this is called a sonogram [52, 53]. This technique relies on cross-correlating the pulse with its frequency-filtered replica for a number of different centre frequencies. An example of the resultant spectrogram is shown in figure 1.11. A similar computational procedure is then applied to retrieve the spectral phase.



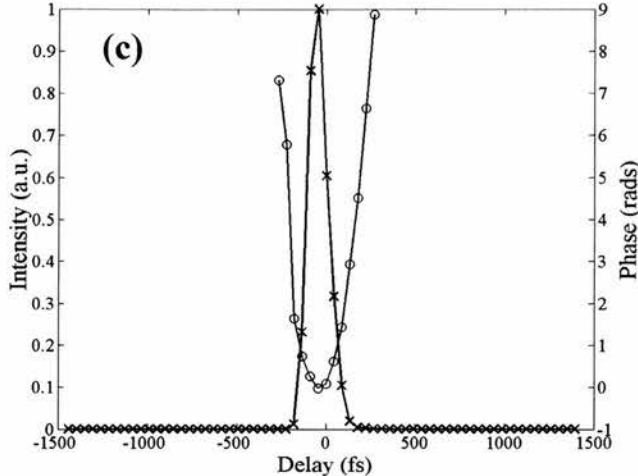


Figure 1.11: Example of a sonogram trace. (a) the acquired sonogram trace, (b) the retrieved sonogram trace (after a retrieval algorithm), and (c) The temporal intensity (crosses) and the phase (circles). This pulse exhibits a positive linear chirp. (Diagram courtesy of Dr. Iain Cormack.)

Recent years have seen the development of very powerful phase measurement techniques. A sonogram setup without any moving parts that is capable of measuring the spectral phase of an ultrashort optical pulse in a single shot has been developed [54]. Measurement of the spectral phase of a single ultrashort optical pulse provides an invaluable insight into the pulse formation process and has the potential to allow for optical pulses which a ‘designer’ spectral phase [55]. It has also been shown that the detector arrangement in a FROG setup can be replaced with a crystal which can amplify the incident signal [56]. This technique can measure the spectral phase of very low intensity pulses and will allow for the measurement of the spectral phase associated with ultrashort bursts of fluorescence. These phase measurement techniques will form an important part of many future applications of ultrashort optical pulses

1.5 Conclusions

The work presented in the later chapters of this thesis builds on the science presented in this chapter. In particular, techniques through which the adaptability of femtosecond lasers can be improved are presented. In chapter 2,

methods for measuring the dispersion of a multilayer dielectric mirror are described and implemented. Chapter 2 also deals with the design of multilayer dielectric coatings for dispersion compensation. The mirror designs presented in chapter 2 allowed for the construction of the SBR-modelocked Ti: sapphire lasers with very high repetition-rates that are described in chapter 4. Chapter 2 also deals with mirrors that offer dispersion compensation over a broad spectral bandwidth. These are used in chapter 3 to demonstrate that the centre wavelength of a compact, low-threshold, femtosecond laser can be tunable over tens of nanometres without the use of intracavity prisms. Chapter 5 details the design and construction of a compact, low-threshold Ti: sapphire laser pumped by an inexpensive green laser. This laser represents a non-incremental step in femtosecond laser development as it shows that Ti: sapphire lasers do not require a bulky pump source with water-cooling and large amounts of external electronics. In chapter 6 the results of a series of experiments using electrical injection to a saturable absorber mirror are presented. The work presented in chapter 6 is a first step towards realising a scheme whereby the output of a passively modelocked femtosecond laser can be locked to an external clock signal and this may prove useful in optical data communications. The project work described in this thesis goes some way to showing that, through in-depth design considerations, femtosecond lasers need not be a sophisticated laboratory device but rather a highly adaptable tool capable of opening up new avenues in science.

References

- [1] J. K. Ranka, R. S. Windeler, and A. J. Stentz, "Visible continuum generation in air-silica microstructure optical fibers with anomalous dispersion at 800 nm," *Optics Letters*, vol. 25, pp. 25-27, 2000.
- [2] H. N. Paulsen, K. M. Hilligsoe, J. Thogersen, S. R. Keiding, and J. J. Larsen, "Coherent anti-Stokes Raman scattering microscopy with a photonic crystal fiber based light source," *Optics Letters*, vol. 28, pp. 1123-1125, 2003.
- [3] Y. M. Wang, J. S. Nelson, Z. P. Chen, B. J. Reiser, R. S. Chuck, and R. S. Windeler, "Optimal wavelength for ultrahigh-resolution optical coherence tomography," *Optics Express*, vol. 11, pp. 1411-1417, 2003.
- [4] Y. M. Wang, Y. H. Zhao, J. S. Nelson, Z. P. Chen, and R. S. Windeler, "Ultrahigh-resolution optical coherence tomography by broadband continuum generation from a photonic crystal fiber," *Optics Letters*, vol. 28, pp. 182-184, 2003.
- [5] A. Bartels and H. Kurz, "Generation of a broadband continuum by a Ti : sapphire femtosecond oscillator with a 1-GHz repetition rate," *Optics Letters*, vol. 27, pp. 1839-1841, 2002.
- [6] W. H. Knox, "Ultrafast technology in telecommunications," *IEEE Journal of Selected Topics in Quantum Electronics*, vol. 6, pp. 1273-1278, 2000.
- [7] M. Drescher, M. Hentschel, R. Kienberger, G. Tempea, C. Spielmann, G. A. Reider, P. B. Corkum, and F. Krausz, "X-ray pulses approaching the attosecond frontier," *Science*, vol. 291, pp. 1923-1927, 2001.
- [8] R. Kienberger, M. Hentschel, C. Spielmann, G. A. Reider, N. Milosevic, U. Heinzmann, M. Drescher, and F. Krausz, "Sub-femtosecond X-ray pulse generation and measurement," *Applied Physics B-Lasers and Optics*, vol. 74, pp. S3-S9, 2002.
- [9] A. Baltuska, T. Udem, M. Uiberacker, M. Hentschel, E. Goulielmakis, C. Gohle, R. Holzwarth, V. S. Yakovlev, A. Scrinzi, T. W. Hansch, and F. Krausz, "Attosecond control of electronic processes by intense light fields," *Nature*, vol. 421, pp. 611-615, 2003.
- [10] R. Kienberger, M. Hentschel, M. Uiberacker, C. Spielmann, M. Kitzler, A. Scrinzi, M. Wieland, T. Westerwalbesloh, U. Kleineberg, U. Heinzmann, M. Drescher, and F. Krausz, "Steering attosecond electron wave packets with light," *Science*, vol. 297, pp. 1144-1148, 2002.

- [11] A. Siegman, *Lasers*: University Science Books, 1986.
- [12] I. Walmsley, L. Wexler, and C. Dorrer, “The role of dispersion in ultrafast optics,” *Review of Scientific Instruments*, vol. 72, pp. 1-29, 2001.
- [13] O. E. Martinez, J. P. Gordon, and R. L. Fork, “Negative Group-Velocity Dispersion Using Refraction,” *Journal of the Optical Society of America a-Optics Image Science and Vision*, vol. 1, pp. 1003-1006, 1984.
- [14] J. P. Gordon, R. L. Fork, and O. E. Martinez, “Negative Dispersion From Prisms,” *Journal of the Optical Society of America B-Optical Physics*, vol. 1, pp. 437-437, 1984.
- [15] R. L. Fork, O. E. Martinez, and J. P. Gordon, “Negative Dispersion Using Pairs of Prisms,” *Optics Letters*, vol. 9, pp. 150-152, 1984.
- [16] J. P. Gordon and R. L. Fork, “Optical-Resonator With Negative Dispersion,” *Optics Letters*, vol. 9, pp. 153-155, 1984.
- [17] P. F. Curley, C. Spielmann, T. Brabec, F. Krausz, E. Wintner, and A. J. Schmidt, “Operation of a Femtosecond Ti-Sapphire Solitary Laser in the Vicinity of Zero Group-Delay Dispersion,” *Optics Letters*, vol. 18, pp. 54-56, 1993.
- [18] R. E. Sherriff, “Analytic expressions for group-delay dispersion and cubic dispersion in arbitrary prism sequences,” *Journal of the Optical Society of America B-Optical Physics*, vol. 15, pp. 1224-1230, 1998.
- [19] S. Akturk, M. Kimmel, P. O’Shea, and R. Trebino, “Measuring pulse-front tilt in ultrashort pulses using GRENOUILLE,” *Optics Express*, vol. 11, pp. 491-501, 2003.
- [20] “<http://phys.strath.ac.uk/12-370/>” .
- [21] D. E. Spence and W. Sibbett, “Femtosecond Pulse Generation By a Dispersion-Compensated, Coupled-Cavity, Mode-Locked Ti-Sapphire Laser,” *Journal of the Optical Society of America B-Optical Physics*, vol. 8, pp. 2053-2069, 1991.
- [22] D. E. Spence, P. N. Kean, and W. Sibbett, “60-Fsec Pulse Generation From a Self-Mode-Locked Ti-Sapphire Laser,” *Optics Letters*, vol. 16, pp. 42-44, 1991.
- [23] M. Piche, “Beam Reshaping and Self-Mode-Locking in Nonlinear Laser Resonators,” *Optics Communications*, vol. 86, pp. 156-160, 1991.
- [24] M. Piche and F. Salin, “Self-Mode Locking of Solid-State Lasers Without Apertures,” *Optics Letters*, vol. 18, pp. 1041-1043, 1993.

- [25] J. Herrmann, "Theory of Kerr-Lens Mode-Locking - Role of Self-Focusing and Radially Varying Gain," *Journal of the Optical Society of America B-Optical Physics*, vol. 11, pp. 498-512, 1994.
- [26] H. L. Statz and C. L. Tang, *Journal of Applied Physics*, vol. 36, pp. 3923, 1995.
- [27] C. Spielmann, F. Krausz, T. Brabec, E. Wintner, and A. J. Schmidt, "Femtosecond Pulse Generation From a Synchronously Pumped Ti- Sapphire Laser," *Optics Letters*, vol. 16, pp. 1180-1182, 1991.
- [28] L. A. Glasser, *Electronics Letters*, vol. 14, pp. 25, 1978.
- [29] M. DiDomenico, J. E. Geusic, H. M. Marcos, and R. G. Smith, *Applied Physics Letters*, vol. 8, pp. 180, 1966.
- [30] D. J. Kuizenga and A. E. Siegman, *IEEE Journal of Quantum Electronics*, vol. 11, pp. 709, 1970.
- [31] U. Keller, K. J. Weingarten, F. X. Kartner, D. Kopf, B. Braun, I. D. Jung, R. Fluck, C. Honninger, N. Matuschek, and J. A. derAu, "Semiconductor saturable absorber mirrors (SESAM's) for femtosecond to nanosecond pulse generation in solid-state lasers," *IEEE Journal of Selected Topics in Quantum Electronics*, vol. 2, pp. 435-453, 1996.
- [32] S. Tsuda, W. H. Knox, S. T. Cundiff, W. Y. Jan, and J. E. Cunningham, "Mode-locking ultrafast solid-state lasers with saturable Bragg reflectors," *IEEE Journal of Selected Topics in Quantum Electronics*, vol. 2, pp. 454-464, 1996.
- [33] U. Keller, "Semiconductor nonlinearities for solid-state laser modelocking and Q-switching," in *Nonlinear Optics in Semiconductors I*, vol. 59, *Semiconductors and Semimetals*, 1999, pp. 211-286.
- [34] D. H. Sutter, L. Gallmann, N. Matuschek, F. Morier-Genoud, V. Scheuer, G. Angelow, T. Tschudi, G. Steinmeyer, and U. Keller, "Sub-6-fs pulses from a SESAM-assisted Kerr-lens modelocked Ti : sapphire laser: at the frontiers of ultrashort pulse generation," *Applied Physics B-Lasers and Optics*, vol. 70, pp. S5-S12, 2000.
- [35] H. A. Haus, "Mode-locking of lasers," *IEEE Journal of Selected Topics in Quantum Electronics*, vol. 6, pp. 1173-1185, 2000.
- [36] A. Robertson, U. Ernst, R. Knappe, R. Wallenstein, V. Scheuer, T. Tschudi, D. Burns, M. D. Dawson, and A. I. Ferguson, "Prismless diode-pumped mode-locked femtosecond Cr : LiSAF laser," *Optics Communications*, vol. 163, pp. 38-43, 1999.

- [37] D. Kopf, A. Prasad, G. Zhang, M. Moser, and U. Keller, "Broadly tunable femtosecond Cr:LiSAF laser," *Optics Letters*, vol. 22, pp. 621-623, 1997.
- [38] F. X. Kartner, I. D. Jung, and U. Keller, "Soliton mode-locking with saturable absorbers," *IEEE Journal of Selected Topics in Quantum Electronics*, vol. 2, pp. 540-556, 1996.
- [39] F. M. Mitschke and L. F. Mollenauer, "Stabilizing the Soliton Laser," *IEEE Journal of Quantum Electronics*, vol. 22, pp. 2242-2250, 1986.
- [40] R. Paschotta and U. Keller, "Passive mode locking with slow saturable absorbers," *Applied Physics B-Lasers and Optics*, vol. 73, pp. 653-662, 2001.
- [41] F. X. Kartner, J. A. D. Au, and U. Keller, "Mode-locking with slow and fast saturable absorbers - What's the difference?," *IEEE Journal of Selected Topics in Quantum Electronics*, vol. 4, pp. 159-168, 1998.
- [42] H. A. Haus, J. G. Fujimoto, and E. P. Ippen, "Structures For Additive Pulse Mode-Locking," *Journal of the Optical Society of America B-Optical Physics*, vol. 8, pp. 2068-2076, 1991.
- [43] C. Honninger, R. Paschotta, F. Morier-Genoud, M. Moser, and U. Keller, "Q-switching stability limits of continuous-wave passive mode locking," *Journal of the Optical Society of America B-Optical Physics*, vol. 16, pp. 46-56, 1999.
- [44] H. D. Sun, G. J. Valentine, R. Macaluso, S. Calvez, D. Burns, M. D. Dawson, T. Jouhti, and M. Pessa, "Low-loss 1.3-mu m GaInNAs saturable Bragg reflector for high- power picosecond neodymium lasers," *Optics Letters*, vol. 27, pp. 2124-2126, 2002.
- [45] J. A. Armstrong, "Measurement of picosecond laser pulse widths," *Applied Physics Letters*, vol. 10, pp. 16-18, 1967.
- [46] J. C. M. Diels, J. J. Fontaine, I. C. McMichael, and F. Simoni, "Control and Measurement of Ultrashort Pulse Shapes (in Amplitude and Phase) With Femtosecond Accuracy," *Applied Optics*, vol. 24, pp. 1270-1282, 1985.
- [47] D. T. Reid, M. Padgett, C. McGowan, W. E. Sleat, and W. Sibbett, "Light-emitting diodes as measurement devices for femtosecond laser pulses," *Optics Letters*, vol. 22, pp. 233-235, 1997.
- [48] A. M. Weiner, "Effect of group-velocity mismatch on the measurement of ultrashort optical pulses via 2nd harmonic generation," *IEEE journal of quantum electronics*, vol. 19, pp. 1276-1283, 1983.
- [49] D. J. Kane and R. Trebino, "Single-Shot Measurement of the Intensity and Phase of an Arbitrary Ultrashort Pulse By Using Frequency-Resolved Optical Gating," *Optics Letters*, vol. 18, pp. 823-825, 1993.

- [50] K. W. Delong, R. Trebino, J. Hunter, and W. E. White, "Frequency-Resolved Optical Gating With the Use of 2nd-Harmonic Generation," *Journal of the Optical Society of America B-Optical Physics*, vol. 11, pp. 2206-2215, 1994.
- [51] R. Trebino, K. W. DeLong, D. N. Fittinghoff, J. N. Sweetser, M. A. Krumbiegel, B. A. Richman, and D. J. Kane, "Measuring ultrashort laser pulses in the time-frequency domain using frequency-resolved optical gating," *Review of Scientific Instruments*, vol. 68, pp. 3277-3295, 1997.
- [52] I. G. Cormack, W. Sibbett, R. Ortega-Martinez, and D. T. Reid, "Ultrashort pulse characterization using a scanning Fabry-Perot etalon enabling rapid acquisition and retrieval of a sonogram at rates up to 1.52 Hz," *Review of Scientific Instruments*, vol. 72, pp. 4071-4079, 2001.
- [53] I. G. Cormack, W. Sibbett, and D. T. Reid, "Rapid measurement of ultrashort-pulse amplitude and phase from a two-photon absorption sonogram trace," *Journal of the Optical Society of America B-Optical Physics*, vol. 18, pp. 1377-1382, 2001.
- [54] D. T. Reid and I. G. Cormack, "Single-shot sonogram: a real-time chirp monitor for ultrafast oscillators," *Optics Letters*, vol. 27, pp. 658-660, 2002.
- [55] J. Garduno-Mejia, A. H. Greenaway, and D. T. Reid, "Designer femtosecond pulses using adaptive optics," *Optics Express*, vol. 11, pp. 2030-2040, 2003.
- [56] J. Y. Zhang, A. P. Shreenath, M. Kimmel, E. Zeek, R. Trebino, and S. Link, "Measurement of the intensity and phase of attojoule femtosecond light pulses using optical-parametric-amplification cross- correlation frequency-resolved optical gating," *Optics Express*, vol. 11, pp. 601-609, 2003.

Chapter 2 - Dispersion of multilayer dielectric mirrors: measurement and analysis

2.1 Introduction

Compensation for dispersion is a key element in the design and operation of femtosecond lasers. In recent years many advances have been made in the development of mirror designs that can ensure both a very short pulse duration and a decrease in the overall cavity dimensions [1]. Many applications of femtosecond lasers require a resonator that does not incorporate intracavity prisms for dispersion compensation. The use of prisms may not be a viable option for several reasons, including ease of alignment, stability, or perhaps minimisation of the round-trip time for high-repetition rate systems (see chapter 4).

This chapter is divided into two sections. The first part deals with the measurement of dispersion in general and measurements using a technique based on white-light interferometry [2] are detailed and explained. The second part of this chapter deals with the analysis of multilayer mirrors; in particular multilayer mirrors that can be used for dispersion compensation in a femtosecond laser. These mirrors are analysed using two different pieces of software, namely an extended version of the “LTR” method [3] devised by Dr. Michael Mazilu of the University of St Andrews and the “Essential McLeod” thin films package [4]. Both of these tools were used to gain a fuller understanding of the dispersive properties of mirrors used in laser cavities. They were also used to design mirrors that allowed the high-repetition rate Ti:sapphire lasers discussed in chapter 4 to be constructed. A thorough description of dispersion and its origins can be found in chapter 1.

2.2 Measurement of Dispersion

Several different approaches can be taken to the measurement of the dispersion of an optical component or a laser cavity as a whole. Some of these techniques will be outlined briefly in this section before describing the technique used to

measure the dispersive properties of a multilayer mirror which was thought to provide adequate dispersion compensation in a femtosecond Cr: LiSAF laser.

2.2.1 Interferometric and intracavity dispersion measurement techniques

Interferometric techniques use interference fringes created from a broadband light source to determine the group delay (GD). The group delay is related to the induced change in spectral phase between the frequency components of the light source. This technique was initially used to calculate the dispersion of a single mode fibre [5] but was later used to measure the dispersion of intracavity optical components [6].

Interferometric techniques allow the measurement of the relative group delay using a frequency-filtered broadband source and a Michelson interferometer (see figure 2.1). The change in group delay can be inferred by measuring the change in fringe position with differing centre wavelength. Specifically, white light is incident on the Michelson interferometer and the fringe pattern is formed. It is then passed through a tunable frequency bandpass filter and the frequency-dependent fringe pattern is measured using a photomultiplier tube and lock-in amplifier. This technique and its derivatives have a disadvantage in that the spectral characteristics of the incident light must be determined before the measurement is made. One technique that does not suffer from this disadvantage is a Fourier transform cross-correlation technique and consequently this was used in the work described in section 2.2.3 [7].

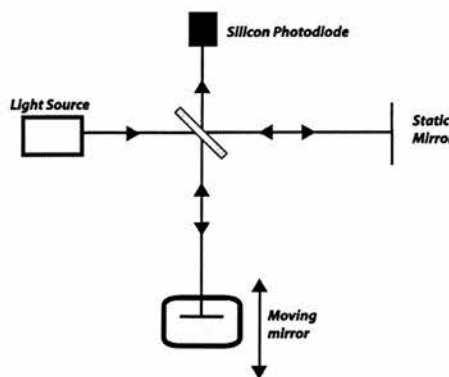


Figure 2.1: Michelson interferometer setup used in many dispersion measurements.

A second group of techniques exist for measuring dispersion and are based around the use of the laser cavity in question as a measurement device. One technique uses a laser operating below threshold [8], the other involves measurements of the repetition-rate of the modelocked laser to calculate the group delay dispersion (GDD) present in the laser cavity [9].

2.2.2 Motivation and measurement of the dispersion of multilayer mirrors using white light interferometry

2.2.2.1 Motivation

A Cr: LiSAF laser that was modelocked without any deliberately inserted source of negative dispersion (the characteristics of this laser are shown in figure 2.2) had been constructed previously at the University of St Andrews [10]. Through a process of elimination, it was found that when a different set of cavity mirrors was utilised the laser no longer modelocked. This raised the possibility that the dichroic high reflectors, which had only been specified for high reflectivity at 860nm and high transmissivity at 660nm, had a fortuitous phase change associated with reflection that could compensate for pulse broadening through the laser crystal. The mirrors were manufactured by QTF Ltd. (*Oldsmar, FL*) and will be referred to as the QTF mirror set.

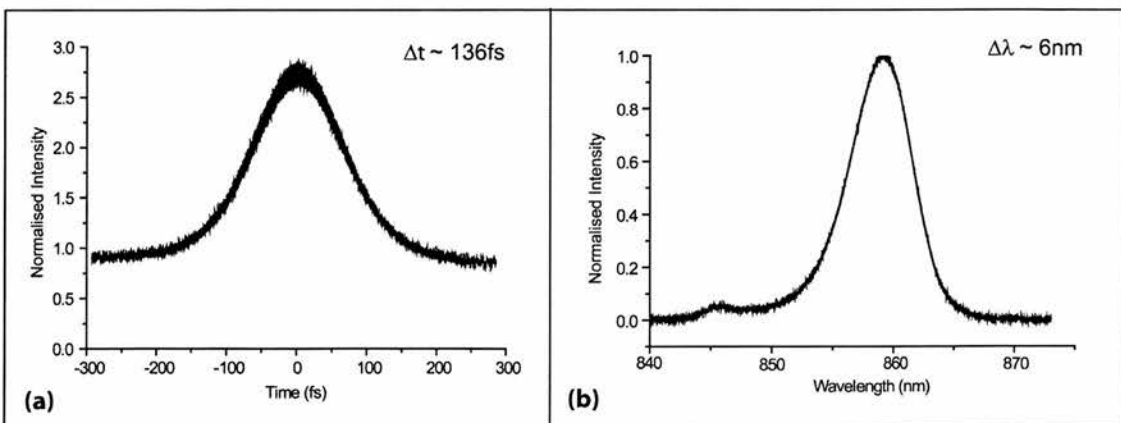


Figure 2.2: (a), Autocorrelation and (b), spectrum of the Cr: LiSAF laser that incorporated the QTF mirror set.

White light interferometry [3] was used to measure the dispersion of these QTF mirrors and the details of this experiment are covered in the next section.

2.2.2.2 Dispersion measurement using white-light interferometry

This method for determining the GDD of a particular sample (whether it is a mirror, laser crystal, or any optical component) relies on the relation, shown in equation 1, between the GDD and change in spectral phase on reflection:

$$GDD = \frac{\delta^2 \phi}{\delta \omega^2} \quad (1)$$

where ϕ is the spectral phase and ω is the angular frequency. The phase is determined from the interferogram created by a Michelson interferometer (see figure 2.1). If one arm of the interferometer is scanned around the zero path difference then an interferogram will be formed at the photodiode. If another interferogram is measured with a sample of unknown dispersion in one of the arms the shape of the interferogram will be affected. If the difference in phase difference between the two interferograms is measured this can be used in conjunction with equation 1 to determine the magnitude of the GDD.

The photodiode measures the total field, that is the combination of the field from the reference arm, $E_r(t)$ and the time delayed field from the arm containing the moving mirror, $E_s(t-\tau)$ so the total signal measured by the photodiode is given by,

$$I(\tau) = \int_{-\infty}^{\infty} |E_r(t - \tau) + E_s(t)|^2 dt \quad (2)$$

The phase difference between the two arms can be written as,

$$e_s(\omega) = e_r(\omega) \cdot \exp[i\phi(\omega)] \quad (3)$$

Where $e(\omega)$ is the Fourier transform of $E(t)$. Equation 2 can thus be rewritten

$$I(\tau) = \int_{-\infty}^{\infty} 2.I_r(t)dt + \int_{-\infty}^{\infty} [E(t).E^*(t - \tau) + E^*(t).E(t - \tau)]dt \quad (4)$$

where

$$I_r(t) = |E_r(t)|^2 \quad (5)$$

Combining equations 3 and 4 gives

$$\begin{aligned} I(\tau) &= 2. \int_{-\infty}^{\infty} I_r(t)dt + FT^{-1}\{i(\omega).\exp[i.\phi_s(\omega) + \pi]\} + \\ &FT^{-1}\{i(-\omega).\exp[-i.\phi_s(-\omega) - \pi]\} \end{aligned} \quad (6)$$

where FT^{-1} corresponds to an inverse Fourier transform and:

$$i(\omega) = |e_r(\omega)|^2 = |e_s(\omega)|^2 \quad (7)$$

After the interferogram has been measured, the Fourier transform may be taken and this will result in a dc component corresponding to zero frequency and two intensity components that are symmetric about the zero frequency line. These correspond to the power spectrum of the light source coupled with the reflectivity of the mirror. If two interferograms are taken, one with a mirror of known dispersion (e.g. a silvered mirror with negligible dispersion) and another with the sample mirror in place, subtraction of their spectral phases will result in calculation of the phase change resulting purely from the mirror structure. From this, equation 1 may then be used to determine the GDD.

The experimental set-up is shown in figure 2.3 and can be understood as two different interferometers. The top and bottom halves of this experimental setup are separated by a mirror on a piezo-electric stage. The top half of the diagram is a calibration interferometer and the bottom half is the measurement interferometer. The calibration interferometer is used to determine the time axis

as displayed on the oscilloscope. Knowing the time calibration for this oscilloscope trace allows the delay of the white light fringes to be deduced. The fringes measured on the photodiode in the calibration interferometer from the HeNe laser may be used to determine the delay axis of the sample interferometer trace as successive fringes will be generated when the delay is equal to λ/c . The measurement interferometer must be aligned to micron-level accuracy because the coherence length of the light from the Halogen lamp is very short. Once these two interferometers are aligned, the white-light interference fringes can be measured against delay by recording both the sample and HeNe interference patterns simultaneously. By counting the number of HeNe fringes across the white-light interference pattern the delay across the trace can be determined.

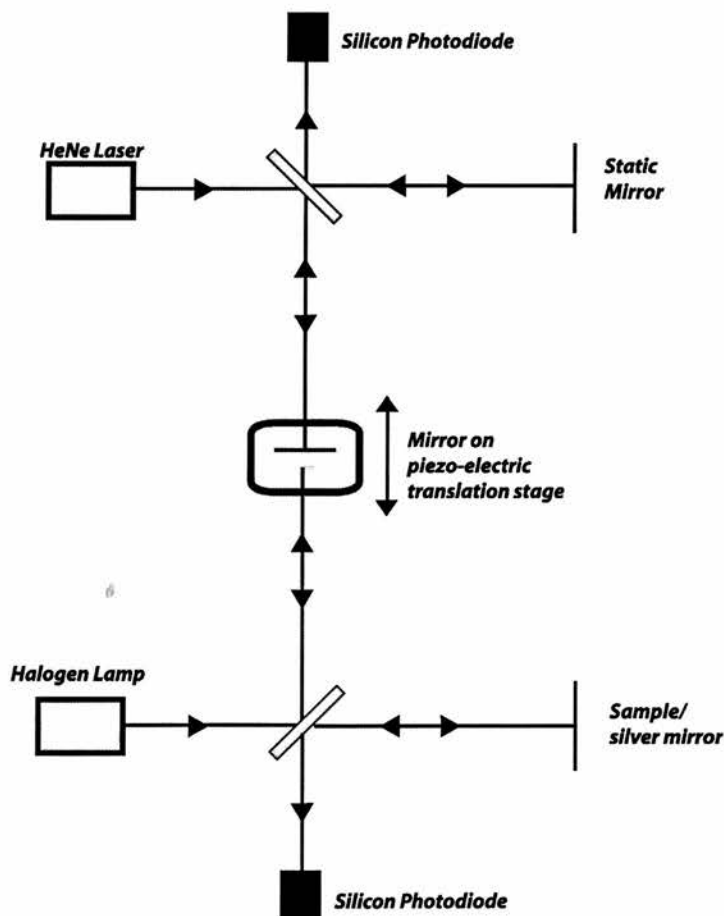


Figure 2.3: The experimental setup for dispersion measurements using white-light interferometry.

Examples of the measured reflectivity spectrum of the silver mirror (green), a regular dichroic mirror (blue) and the QTF mirror (red) are shown in figure 2.4. These do not look like the expected reflectivity curves for a number of reasons. To obtain regular reflectivity curves these traces would have to be normalised against the power spectrum of the lamp.

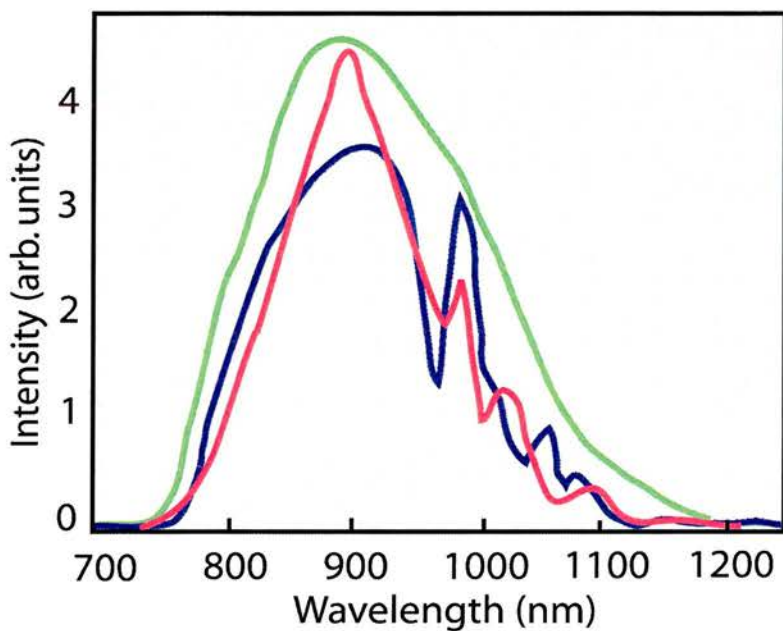


Figure 2.4: The reflectivity spectrum, or the real part of the Fourier transform of the calibrated interference patterns of the silver mirror (green), the regular dichroic mirror (blue) and the QTF mirror (red).

After obtaining the Fourier transform of both the QTF mirror and the silver mirror interferograms, the phase associated with the silver mirror interferogram is subtracted from that of the sample interferogram to obtain the phase change associated with the dispersion of the sample mirror. From equation 1, the second derivative can be calculated to obtain the group delay dispersion associated with the sample. This can be seen, in the case of the QTF mirror in figure 2.5 along with a detail of the spectral region in which modelocking was achieved.

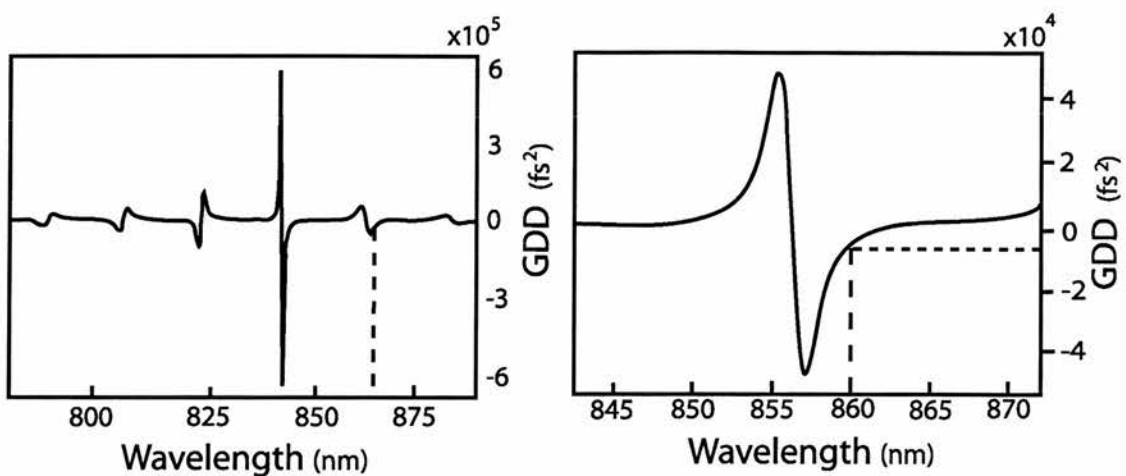


Figure 2.5: Group delay dispersion as a function of wavelength for the QTF mirrors with phase anomaly. The range 800nm to 900nm (left) and a detail of the spectral region over which modelocking was obtained (right).

From figure 2.5 it can be seen that there is significant group delay dispersion over the spectral region around 860nm in which modelocking was achieved. This result can be compared to the group delay dispersion measured from a single reflection off one of the mirrors that did not allow the laser to produce femtosecond pulses shown in figure 2.6.

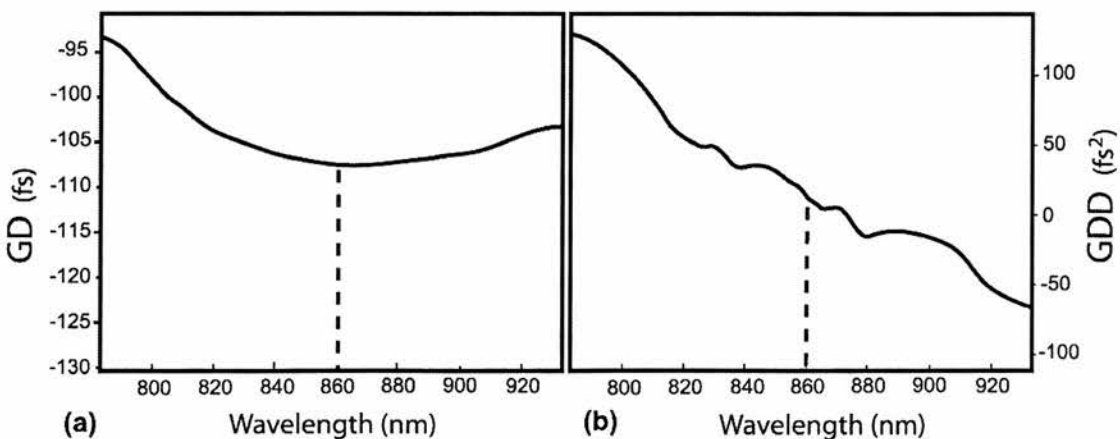


Figure 2.6: The group delay (a) and group delay dispersion (b) in reflection of the “regular” mirror.

Comparison of the graphs in figure 2.5 and 2.6 show that the laser which could produce femtosecond pulses did have a significant contribution of negative group delay dispersion from the cavity mirrors, whereas the laser which did not produce femtosecond pulses did not have any such contribution. Although the magnitude of the dispersion calculated for the QTF mirror seems quite large ($\sim 10^5 \text{ fs}^2$) when compared to the several hundreds of fs^2 expected from a round trip of the laser cavity, it seems clear that operating in the wings of the resonance may allow for an amount of negative GDD closer in magnitude to that of the cavity. A birefringent filter (see chapter 4) was used to determine the tunability of the laser with these dispersive mirrors. It was found that the centre wavelength of the laser could only be tuned over 3nm with the spectrum deviating significantly from a usual Gaussian shape over this range. This shows that the QTF mirror set provided dispersion compensation for the other intracavity components over a limited spectral range.

2.3 Analysis and design of dispersive mirrors

2.3.1 Introduction

This section deals with the design of a specific dispersive mirror for use in high-repetition rate Ti: sapphire lasers (see chapter 4). This mirror was required to produce a large amount of negative dispersion per reflection with very low transmission loss. It also had to have high transmission of the pump light at 532nm. To facilitate this design, it was necessary examine some different dispersive mirror designs and to determine the advantages and disadvantages associated with each one.

2.3.2 Gires-Tournois interferometer mirrors and multiple-cavity Gires-Tournois interferometer mirrors

The simplest mirror structure that can compensate for significant dispersion through a laser crystal is the Gires-Tournois interferometer mirror (GTI-mirror) [11]. This consists of a typical high-reflectivity quarter-wavelength stack with a single half wavelength layer within the structure (see figure 2.7). This forms a Fabry-Perot structure in the high-reflector and so introduces delays in the

spectral feature that corresponds to the thickness of the half-wavelength layer by an amount strongly dependent on the finesse of the etalon. All the mirror structures detailed in this section have a high index material of TiO_2 ($n= 2.25$) and a low index material of SiO_2 ($n=1.48$). This, and all the mirrors detailed in this section, were designed using the McLeod thin film package [4]

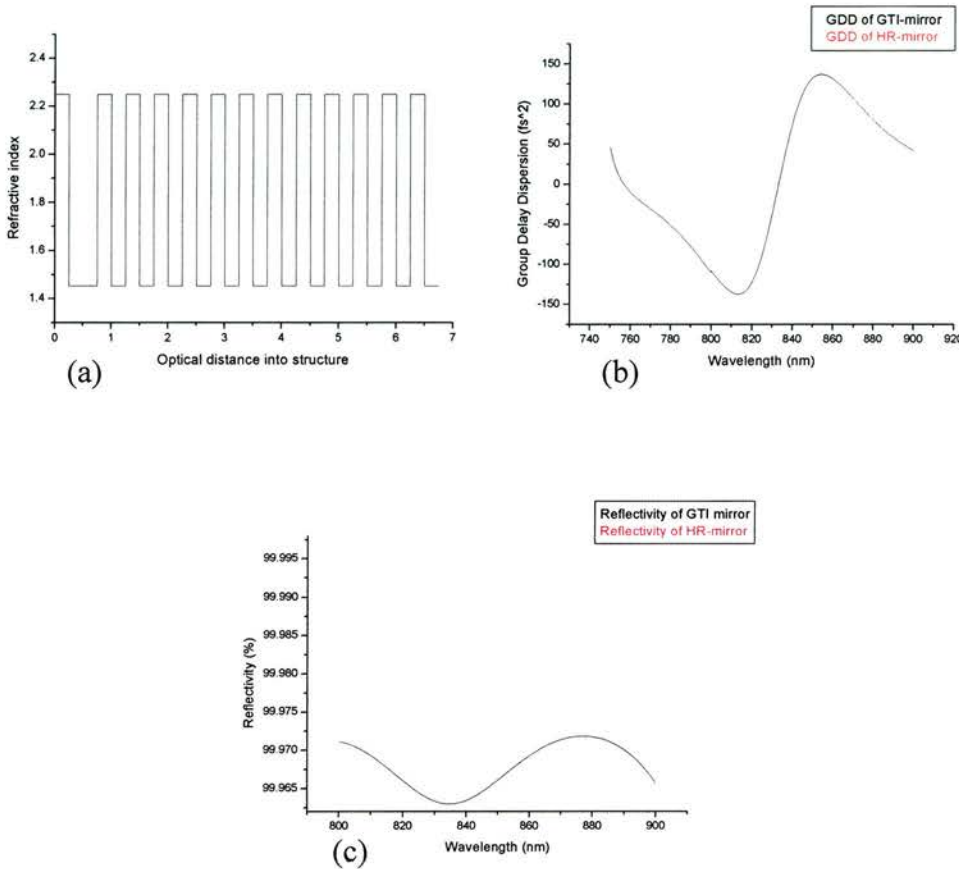


Figure 2.7: (a) The structure of a GTI-mirror, (b) the reflectance group delay dispersion of such a structure compared with a high-reflector, (c) and the overall reflectivity of a GTI-mirror compared to that of a high reflector. As calculated by the McLeod Thin Films package.

By moving the position of the half wavelength layer within the structure, the sharpness of the dispersion feature can be altered. The feature can be made sharper by placing the half wavelength layer further into the structure, hence increasing the finesse of the associated resonance or vice versa. This is shown in figure 2.8.

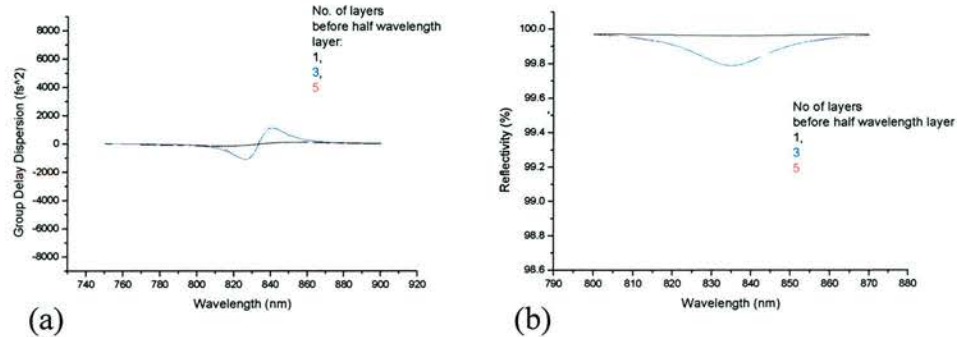


Figure 2.8: The effect on GDD, (a), and reflectivity, (b), of increasing the number of mirror pairs before the half wavelength no. layers=1 (black), =3 (blue), and =5 (red).

As calculated by the McLeod Thin Films package.

This increase in finesse also has implications for the reflectivity of the structure. For instance, if the dispersive feature is made increasingly large, a dip in reflectivity grows accordingly due to transmission of the Fabry-Perot filter. The GTI mirror can also be thought of as a way of trapping light, such that light of a certain frequency takes longer to traverse the mirror structure than light at other frequencies. This can be seen in figure 2.9 where the electric field inside the structure is plotted for both a dielectric quarter-wavelength layer stack and for the GTI structure. As is evident, the magnitude of the field, corresponding to the centre wavelength of the reflectivity bandwidth, is higher in the half-wavelength layer than anywhere else.

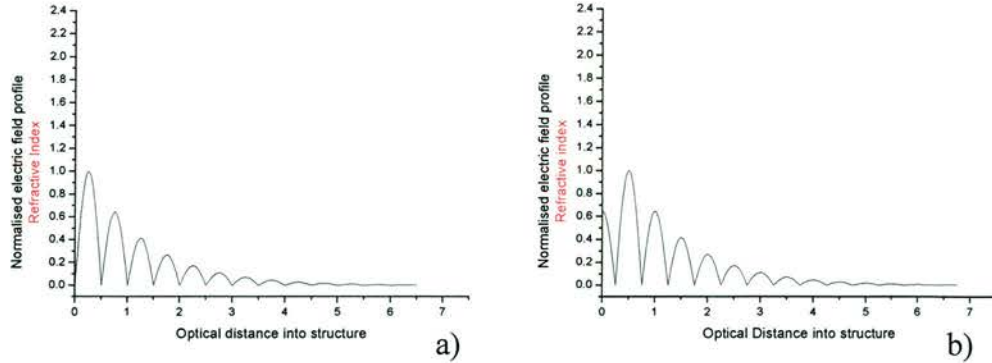


Figure 2.9: The refractive index profile and the magnitude of the electric field for an HR structure (a) and a GTI-mirror structure (b). As calculated by the McLeod Thin Films package.

If a GTI is used as a dispersion-compensating element in a laser cavity, it does afford some degree of tunability of the centre wavelength. By rotating the mirror off normal incidence, the spectral position of the resonance can be shifted to shorter wavelengths. This is shown in figure 2.10. This effect can be used to tune the centre wavelength of a femtosecond laser system.

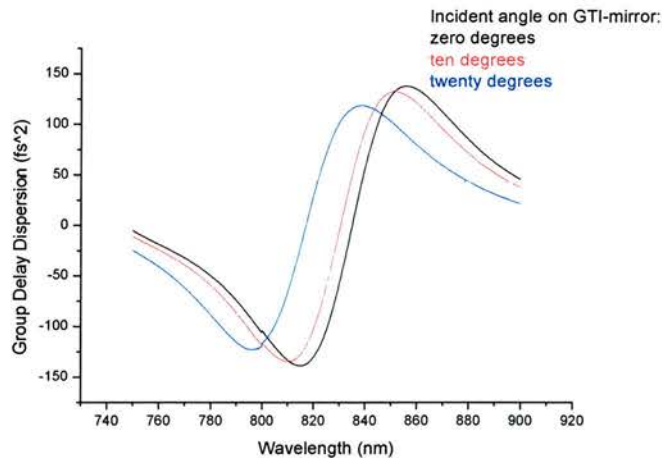


Figure 2.10: Effect of angle tuning the dispersive response of a GTI-mirror. As calculated by the McLeod Thin Films package.

By building up several of these Fabry-Perot cavities, a superstructure can be created that has broadband reflectivity coupled with very low insertion losses. Thus a practicable element for use in low-threshold but broadly-tunable lasers can be designed. This type of structure is called a multiple cavity Gires-Tournois interferometer mirror (MCGTI) mirror [12]. A design for such a mirror is shown in figure 2.11. It contains two slightly detuned half-wavelength layers that provide an almost flat dispersion of around -40fs^2 over a bandwidth of around 100nm. The fact that the dispersive properties of this mirror are provided by the first few layers means that there is essentially no drop in reflectivity compared to a high reflector mirror [13].

The dispersion provided from a single bounce from this mirror is shown in figure 2.12. There are a number of advantages and disadvantages associated with MCGTI mirrors and GTI mirrors. These include:

- MCGTI mirrors have a lower magnitude of GDD than a GTI-mirror due to the overlapping of the resonances.
- MCGTI mirrors require a higher degree of precision during the manufacturing process for the two half wavelength layers because the tolerance on layer thickness is more demanding than that for GTI mirrors.

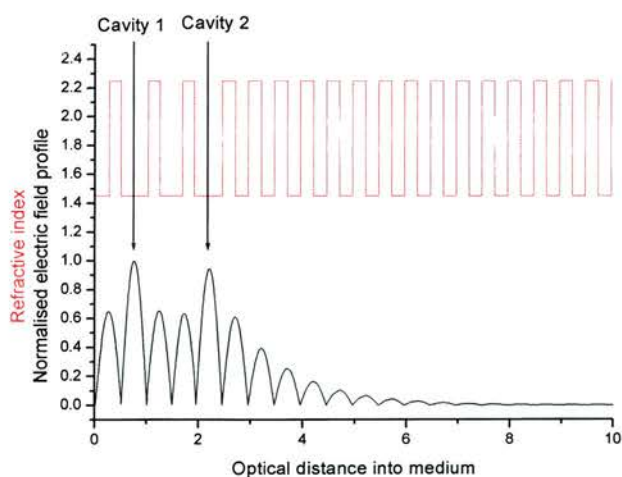


Figure 2.11: Electric field profile (black) and structure (red) of the MCGTI mirror. As calculated by the McLeod Thin Films package.

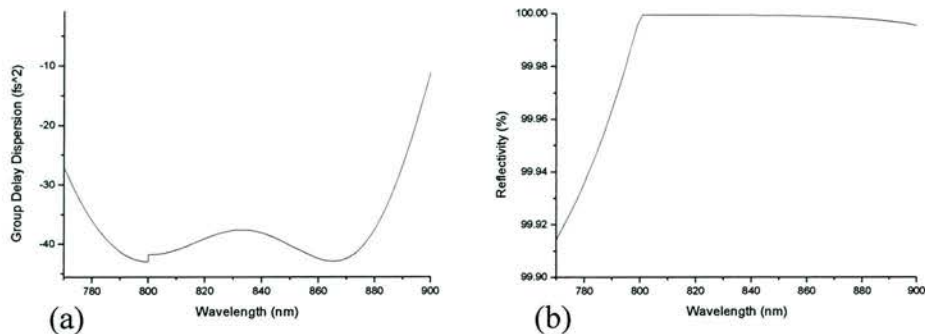


Figure 2.12: Group delay dispersion in reflection, (a), and reflectivity, (b), of the MCGTI structure shown in figure 2.11. As calculated by the McLeod Thin Films package.

[The discontinuity at 800nm in the plot shown in figure 2.12 arises from a discontinuity in the Sellmeier equations used by the program at that point.] If the MCGTI mirror is to be used as an intracavity folding mirror then it is important to know the effect of changing the incident angle on the magnitude of the dispersion.

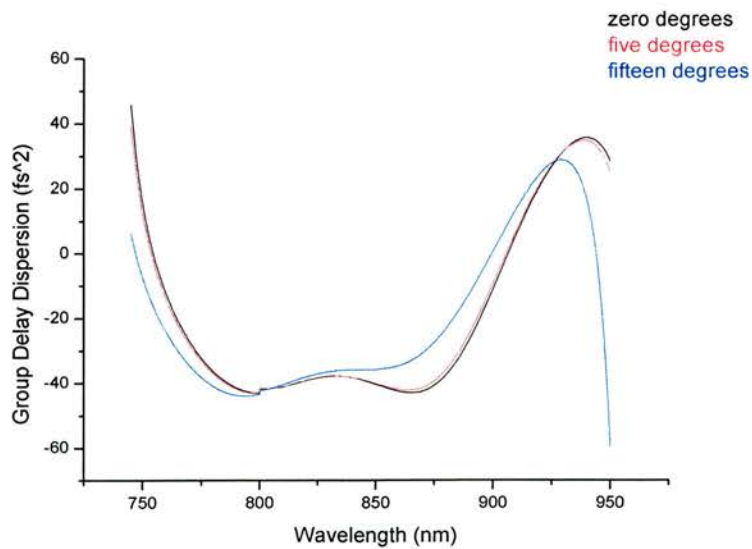


Figure 2.13: The effect of angle tuning the MCGTI mirror. As calculated by the McLeod Thin Films package.

From figure 2.13 it is immediately evident that angle tuning this particular MCGTI structure will not significantly alter the magnitude of the dispersion experienced by the incident light. Only when the incident angle has been increased to more than five degrees does the dispersion curve look significantly different.

2.3.3 Chirped mirrors as a source of negative dispersion

Another, more widely used, technique for achieving the necessary negative dispersion for stable modelocking is to use chirped mirrors [14]. Chirped mirrors were developed in 1986 when it was realised that negative GDD could be achieved by tuning the centre wavelength of the laser off the centre wavelength of the reflectivity of the mirror stack. This caused the longer wavelengths to penetrate deeper into the layer structure than the shorter wavelengths, thereby inducing a frequency-dependent group delay [15]. Chirped mirrors rely on a frequency-dependent penetration depth such that the lower frequency components from the optical pulse penetrate deeper into the mirror structure and are hence delayed with respect to the higher frequency components. This is shown schematically in figure 2.14.

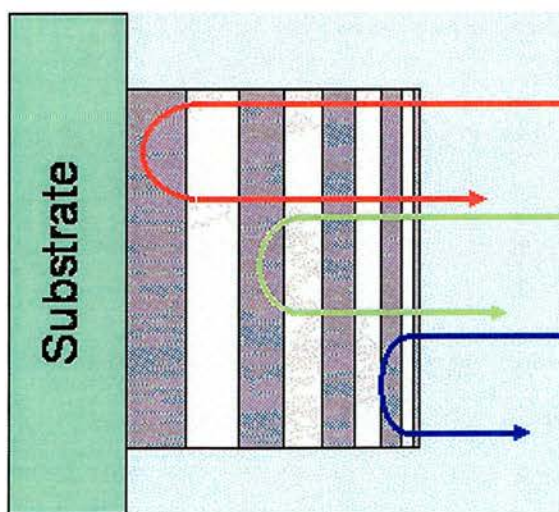


Figure 2.14: Simplified diagram showing the structure of a chirped mirror.

The design of a chirped mirror is a relatively involved procedure, which must be undertaken in the spectral domain because they usually comprise more than 50 layers which, in the spatial domain, implies 50 constants for refinement. This parameterisation is simplified significantly in the spectral domain if the change in layer thickness throughout the structure follows a well-defined function. It should be pointed out that there have been major problems in increasing the bandwidth of chirped mirrors. The main difficulty is the interference between the air/mirror interface and the light reflected off the Bragg stacks. This results in an undesirable modulation in the GDD from the mirror. However, this is only important in the generation of very short pulses. The use of double-chirped mirrors (DCM) along with AR coatings has served to reduce this modulation quite substantially [16]. In a double-chirped mirror the high refractive index layers at the front of the structure are allowed to change thickness more slowly than the low refractive index layers. This eliminates the unwanted modulation in GDD which has been shown to be caused by poor impedance matching [17].

There are several advantages and disadvantages associated with the resonance methods (MCGTIs and GTIs), and the frequency-dependent penetration depth methods (chirped mirrors). These are:

- MCGTIs and GTIs are much easier to design and implement than chirped mirrors.
- MCGTIs and GTIs have reflectivities that are limited by the back mirror characteristics whereas the frequency dependent penetration depth of a chirped mirror can reduce its overall reflectivity.
- Chirped mirrors can be designed to compensate for higher orders of dispersion, notably, 3rd and 4th order, to generate very short pulses.

2.3.4 Design of a dispersive mirror for use in high repetition rate Ti: sapphire lasers

2.3.4.1 Introduction

The purpose of this section is to detail the choice and design of a mirror for use in a high repetition-rate Ti: sapphire laser. The choice of mirror is important

because there must be as much negative dispersion as possible associated with each reflection so as not to increase the length of the cavity through excessive reflections. It would also be advantageous if the final laser were as efficient as possible to facilitate a modest power pump source. These criteria can be met by using mirrors with very high reflectance characteristics.

A pulse traversing through the titanium-doped sapphire gain medium will experience a significant amount of pulse broadening. This can be seen in figure 2.15 which shows the dispersion per millimetre of material for both Ti: sapphire and Cr: LiSAF crystals.

The typical length of the Ti: sapphire rod to be used in the high repetition-rate experiments was around 2.5mm (see chapter 4) and so the magnitude of the round-trip dispersion (neglecting pulse broadening through self-phase modulation) will be around 275fs^2 . With this magnitude of the dispersion in mind, and the desire to keep the number of reflections to a minimum, the choice was made to use GTI-type mirrors.

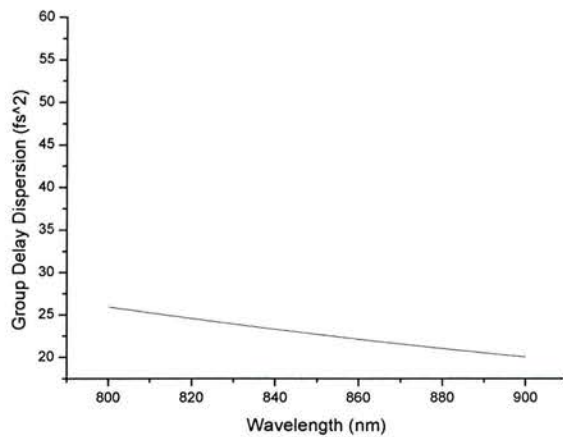


Figure 2.15: Group Delay Dispersion per mm associated with Ti: sapphire (red) and Cr: LiSAF (black).

2.3.4.2 The LTR method

From the literature, it becomes evident that there are two main methods for calculating the reflectivity and other optical properties of thin-film multilayer structures. These are the matrix and the recursive methods [18]. The matrix

method allows the structure to be built up in a modular fashion and the recursive method allows the structure to be built up layer by layer.

The matrix method characterises each layer by a matrix whose elements are derived from the thickness and the refractive index of the layer. The matrix method allows another layer to be added to the structure through simple multiplication of the matrices that describe each layer. The final matrix defines a system of equations that will relate to the transmission and reflection of the system of layers. The recursive method makes use of the fact that the reflectivity of a multilayer structure will depend on the reflectivity of the top layer and the reflectivity of the structure underneath. The reflectivity of a single layer can be calculated using the Fresnel equations and this can be added to a larger structure using a complex mathematical formula. In this way the reflectivity of a multilayer structure is calculated by adding a layer at a time.

A third method exists called the LTR method. It is a modular method developed in the University of St Andrews by Dr. Michael Mazilu for calculating the reflectivity and transmission of a multilayer structure [3, 19]. It differs from the other methods in that it contains a multiplication operator. This is extremely useful when calculating the performance of a multilayer mirror as it typically repeats a single unit a number of times. This method combines the advantages of both the matrix and recursive methods while keeping the calculations relatively simple. To do this, a layer is described by a three-component column vector. The first component describes the amplitude reflectivity of light incident from the left (L). The second describes the amplitude transmission of the layer (T). The third component describes the amplitude reflectivity of light incident from the right (R). These three components are chosen because L and R are typically not the same, however T is the same regardless of whether the light is incident from the left or from the right. It is then possible to define an LTR vector for light incident, of wavelength λ , on a single layer of refractive index n and physical width z as,

$$\begin{pmatrix} r \frac{1-p^2}{1-p^2r^2} \\ p \frac{1-r^2}{1-p^2r^2} \\ r \frac{1-p^2}{1-p^2r^2} \end{pmatrix} \quad (8)$$

where,

$$r = \frac{1-n}{1+n} \quad (9)$$

$$p = e^{i \frac{2\pi n z}{\lambda}} \quad (10)$$

This layer is described with reference to a surrounding vacuum. We can then devise an addition operator for the calculation of an LTR vector for a pair of layers as follows.

$$\begin{pmatrix} L_1 \\ T_1 \\ R_1 \end{pmatrix} \oplus \begin{pmatrix} L_2 \\ T_2 \\ R_2 \end{pmatrix} = \begin{pmatrix} L_1 + \frac{L_2 T_1^2}{1 - R_1 L_2} \\ \frac{T_1 T_2}{1 - R_1 L_2} \\ R_2 + \frac{R_1 T_2^2}{1 - R_1 L_2} \end{pmatrix} \quad (11)$$

This means that the structure can be made up layer by layer until finally a three-component vector that describes the entire system is calculated. As mentioned previously, one of the most interesting properties of the LTR method (when compared to the matrix and recursive methods) is the existence of a very simple multiplication operator that can calculate directly the properties of a periodic structure. The LTR vector for m repeats of a unit is thus given by,

$$m \begin{pmatrix} L \\ T \\ R \end{pmatrix} = \begin{pmatrix} ca \frac{1-b^{2m}}{1-a^2 b^{2m}} \\ b^m \frac{1-a^2}{1-a^2 b^{2m}} \\ \frac{a}{c} \frac{1-2^{bm}}{1-a^2 b^{2m}} \end{pmatrix} \quad (12)$$

where

$$a = \frac{1 - RL + T^2 + \sqrt{(1 - RL + T^2)^2 - 4RL^2}}{2\sqrt{RL}} \quad (13)$$

$$b = \frac{T^2 - RL + \sqrt{RLa}}{T} \quad (14)$$

$$c = \sqrt{\frac{L}{R}} \quad (15)$$

Mazilu and co-workers have successfully implemented an extension to this LTR formalism to describe dispersive effects associated with reflection. This relies on having a six-component vector that contains both L, T and R as well as their derivatives with respect to the wavenumber, k ($2\pi/\lambda$). This allows the phase change associated with reflection to be calculated. A multiplication operator has yet to be devised but can be replaced with successive applications of the addition operator.

In the next section, some useful shorthand is used to describe the multilayer structures under analysis. In this shorthand, H stands for a quarter wave layer of the high index material and L stands for a quarter wave layer of low index material. The structures in the next section all use silica ($n=1.48$) as the low index material and titania ($n=2.25$) as the high index material. So, for example, HL^4 is a series of four pairs of titania and silica quarter wavelength layers.

2.3.4.3 GTI mirrors for high repetition-rate Ti: sapphire lasers

For the construction of a high repetition-rate Ti: sapphire laser, where the number of intracavity components must be kept to a minimum, it is worthwhile to consider the coating of GTI structures onto curved substrates which will allow both dispersion control and mode control. The first stage in this analysis is to look at the dispersive properties of the GTI structure itself. The structure analysed first was a GTI-mirror on loan to the University of St Andrews from the University of Strathclyde [20]. The structure implemented was slightly different but the reflectivity and dispersion profile did not differ significantly from the Strathclyde structure. The structure under analysis is,

$$\text{Substrate H(LH)}^{15}(2L)\text{H Air} \quad (16)$$

The design centre wavelength was 850nm. The reflectivity and dispersive properties of this structure are shown in figure 2.16. The dispersive properties are essentially identical to those provided by the Strathclyde GTI with dispersion values approaching 150fs^2 at about 830nm.

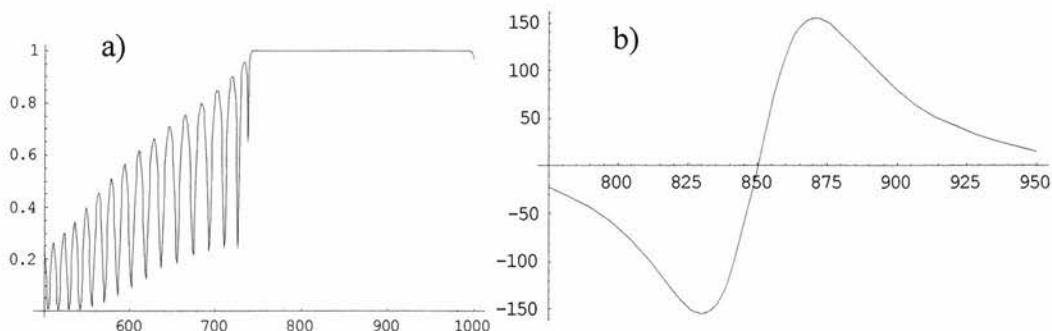


Figure 2.16: (a) The reflectivity, and (b) group delay dispersion, associated with a reflection from the GTI-mirror described in equation 15. The Abscissae are in nm and the ordinates are in fractional reflectivity and fs^2 respectively. As calculated using the LTR method.

Another interesting feature of these GTI mirrors in the context of high repetition rate Ti: sapphire lasers is their transmission in the visible region. As figure 2.17 shows, although the reflectivity profile around 532nm is heavily structured, the

transmission is only compromised by a few per cent. This design can therefore be used to couple pump light directly into the laser cavity. (It is this mirror structure that is used for high-repetition rate Ti: sapphire lasers described in chapter 4). The final mirror purchased also had a dual-band AR coating on the rear for both 830nm and 532nm regions.

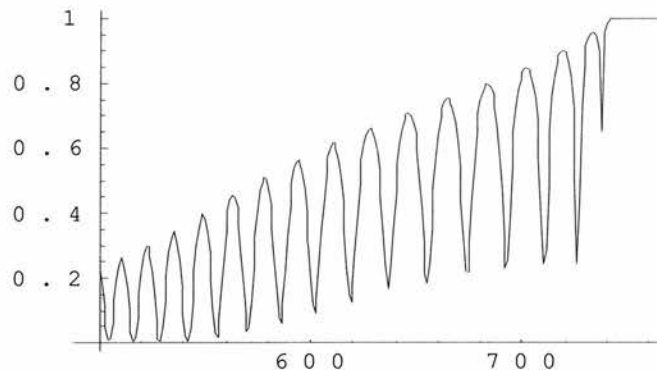


Figure 2.17: Reflectivity in the visible for the GTI mirror described in equation 15. Abscissae are in nm and ordinates are in fractional reflectivity. As calculated using the LTR method.

Although this mirror was satisfactory for use in the high repetition-rate Ti: sapphire lasers, this project continued in order to see if significant improvement could be made to the mirror design. To do this an investigation was made into the design of dichroic high reflectors. Two methods of generating dichroic structures were examined [17]. The first involves a structure of alternating half-wavelength high index layers and quarter-wavelength low index layers to produce what amounts to a long-wavelength bandpass filter. This reduces the amplitude of the subsidiary maxima in the transmission band as compared to a standard quarter wavelength stack high reflector. On examining the following structure

$$((2H)L)^8 \quad (17)$$

it was found that the amplitude of the subsidiary maxima could be suppressed to the 5% level, as shown in figure 2.18. Although this particular structure is a long wave pass filter, it is interesting to note with reference to the QTF mirrors that a

high precision dichroic structure can be constructed using half wavelength layers. This method may enforce a periodic group delay onto an incident pulse centred around the reference wavelength, similar to that measured in section 2.2.3.2. Further suppression of the subsidiary maxima can be achieved by introducing higher-order structures but the dispersive response of such a mirror will be very complicated.

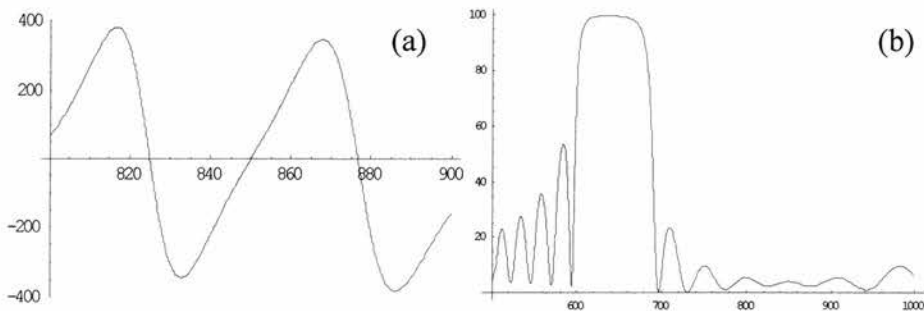


Figure 2.18: The group delay dispersion in the transmission band, (a), and the reflectivity, (b), of the structure described in equation 16 with a design wavelength of 850nm. The abscissae are in nm and the ordinates are in fs^2 and fractional reflectivity respectively. As calculated using the LTR method.

A simpler alternative to this method of constructing a dichroic filter is to produce what is known as an edge filter. In the case of laser mirrors, such a low pass filter would transmit the pump light and reflect the laser light. This can be realised by putting eighth wavelength layers on either side of the quarter wavelength stack that would otherwise finish on a high index quarter wavelength layer. For example:

$$((L/2)H(L/2))^7 \quad (18)$$

This structure consists of standard Bragg mirror with eighth-wavelength layers at the air/mirror and air/substrate boundaries. This structure was modelled using the LTR method and the improvement in pump transmission can be seen in figure 2.19. The structure in equation 17 decreases the reflectivity in the stop band to such an extent that transmissions greater than 90% can be obtained between 500nm and 660nm. The group delay dispersion remains relatively

unaffected by the addition of these eighth-wavelength layers, as shown in figure 2.20.

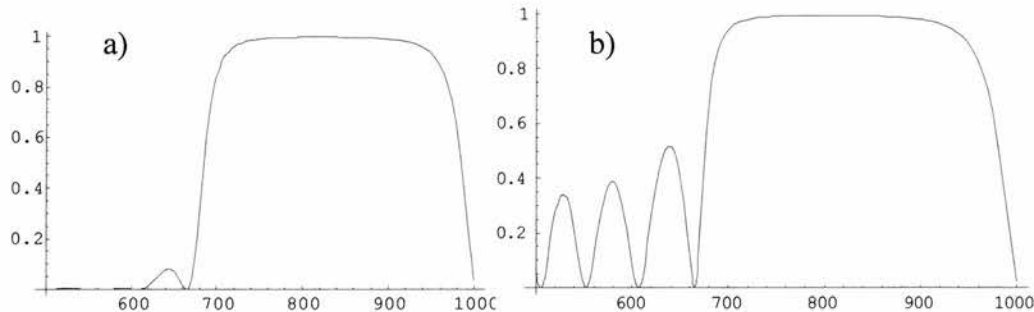


Figure 2.19: Comparison of the reflectivity spectrum of the dichroic mirror described in equation 17(a) and a standard quarter wavelength stack (b). The ordinates are in fractional reflectivity and the abscissae are in nm. As calculated using the LTR method.

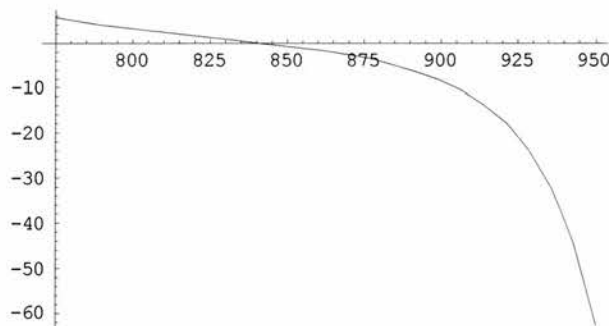


Figure 2.20: The group delay dispersion of the edge filter described in equation 17. The ordinates are in fs² and the abscissae are in nm. As calculated using the LTR method.

To increase the functionality of this mirror by introducing the potential for dispersion compensation, one can consider introducing a half-wavelength layer into the structure to determine whether a GTI-like response can be obtained. To meet this objective, the following structure was considered.

$$((L/2)H(L/2))^{10}(L/2)(2H)LH(L/2) \quad (19)$$

The performance of this dispersive dichroic mirror is shown in figure 2.21. It should be noted that the design wavelength has been changed from 850nm to 820nm in the case of figure 2.21. This change was required in order to place a minimum in reflectivity at 532nm. The insertion of the half-wavelength layer does lead to some deterioration in the suppression of subsidiary maxima in the transmission band. Nonetheless, a transmissivity exceeding 90% is achieved at 532nm. The dispersive properties of this mirror are essentially identical to the properties associated with a standard GTI-mirror. For this structure, negative dispersion up to $\sim 200\text{fs}^2$ is achieved in the spectral band around 800nm. These two properties combine to give a mirror capable of both dispersion control and pump transmission. When combined with a curved substrate this mirror could also provide suitable control of the laser mode.

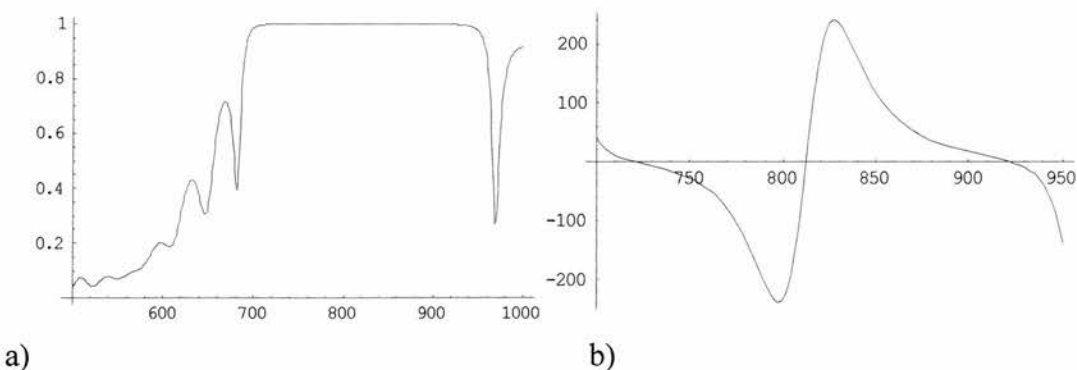


Figure 2.21: The reflectivity spectrum, (a), and group delay dispersion, (b), associated with reflection for the mirror described in equation 18. The Abscissae are in nm and the ordinates are in fractional reflectivity in the case of the reflectivity curve and in the case of the dispersion curve fs^2 . As calculated using the LTR method.

2.4 Conclusions

The project work detailed in this chapter has been concerned with measurement and analysis of dispersive mirrors that are appropriate for the resonators of femtosecond lasers. Following a brief review of the techniques used to measure the dispersion of optical components there was a discussion on how to implement a technique for the measurement of dispersion of optical components known as white-light interferometry. This was used to measure the dispersion of

both a regular dichroic mirror and a mirror containing an anomaly that led to significant negative group delay dispersion. The different types of dispersive mirrors detailed in the literature were then described and analysed using the Essential McLeod thin film modelling software. Particular emphasis was placed on MCGTI-mirrors and GTI-mirrors because of their ease of optimisation. Finally, the LTR method was described and used to design the mirror used in the high-repetition rate, experimental Ti: sapphire lasers that are described in chapter 4. These laser systems produced highly chirped pulses. It may be that these chirped pulses arise from a discrepancy between the saturable absorption offered by the SBR and negative dispersion from the mirrors. This can be seen more clearly in figure 2.22 where the saturable absorption from the SBR is shown alongside the GDD from a single reflection from the GTI-mirrors designed as part of the project work discussed in this chapter. Figure 2.22 also shows the mismatch between these two spectral regions should the GTI-mirrors have a 5% deviation from the designed layer thicknesses. This deviation, and its implications for the net GDD in the laser cavity, could lead to the highly chirped pulses observed in the results reported in chapter 4 of this thesis.

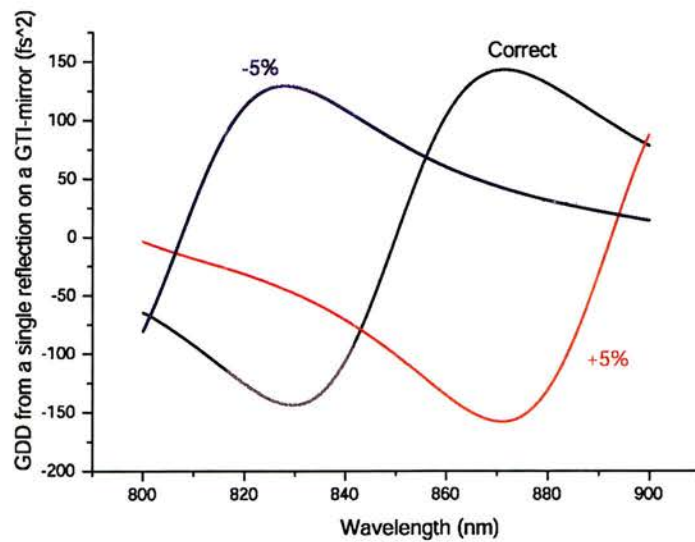


Figure 2.22: Plot of GDD for the correct design and a +/-5% error in layer thickness.

Box shows the measured saturable absorption initiated by the SBR.

References

- [1] E. J. Mayer, J. Möbius, A. Euteneuer, W. W. Ruhle, and R. Szipocs, “Ultrabroadband chirped mirrors for femtosecond lasers,” *Optics Letters*, vol. 22, pp. 528-530, 1997.
- [2] I. G. Cormack, F. Baumann, and D. T. Reid, “Measurement of group velocity dispersion using white light interferometry: A teaching laboratory experiment,” *American Journal of Physics*, vol. 68, pp. 1146-1150, 2000.
- [3] M. Mazilu, A. Miller, and V. T. Donchev, “Modular method for calculation of transmission and reflection in multilayered structures,” *Applied Optics*, vol. 40, pp. 6670-6676, 2001.
- [4] www.thinfilcenter.com
- [5] M. Tateda, N. Shibata, and S. Seikai, “Interferometric Method For Chromatic Dispersion Measurement in a Single-Mode Optical Fiber,” *IEEE Journal of Quantum Electronics*, vol. 17, pp. 404-407, 1981.
- [6] W. H. Knox, N. M. Pearson, K. D. Li, and C. A. Hirlmann, “Interferometric Measurements of Femtosecond Group Delay in Optical-Components,” *Optics Letters*, vol. 13, pp. 574-576, 1988.
- [7] K. Naganuma, K. Mogi, and H. Yamada, “Group-Delay Measurement Using the Fourier-Transform of an Interferometric Cross-Correlation Generated By White-Light,” *Optics Letters*, vol. 15, pp. 393-395, 1990.
- [8] K. Naganuma and Y. Sakai, “Interferometric Measurement of Wavelength Dispersion On Femtosecond Laser Cavities,” *Optics Letters*, vol. 19, pp. 487-489, 1994.
- [9] W. H. Knox, “Insitu Measurement of Complete Intracavity Dispersion in an Operating Ti - Sapphire Femtosecond Laser,” *Optics Letters*, vol. 17, pp. 514-516, 1992.
- [10] B. Agate, B. Stormont, A. J. Kemp, C. T. A. Brown, U. Keller, and W. Sibbett, “Simplified cavity designs for efficient and compact femtosecond Cr : LiSAF lasers,” *Optics Communications*, vol. 205, pp. 207-213, 2002.
- [11] P. Gires and P. Tournois *C.R. de L'Acad Sci*, vol. 258, p. 6112, 1964.

- [12] R. Szipocs, A. Kohazi-Kis, S. Lako, P. Apai, A. P. Kovacs, G. DeBell, L. Mott, A. W. Louderback, A. V. Tikhonravov, and M. K. Trubetskoy, “Negative dispersion mirrors for dispersion control in femtosecond lasers: chirped dielectric mirrors and multi-cavity Gires-Tournois interferometers,” *Applied Physics B-Lasers and Optics*, vol. 70, pp. S51-S57, 2000.
- [13] B. Golubovic, R. R. Austin, M. K. Steiner-Shepard, M. K. Reed, S. A. Diddams, D. J. Jones, and A. G. Van Engen, “Double Gires-Tournois interferometer negative-dispersion mirrors for use in tunable mode-locked lasers,” *Optics Letters*, vol. 25, pp. 275-277, 2000.
- [14] R. Szipocs and A. KohaziKis, “Theory and design of chirped dielectric laser mirrors,” *Applied Physics B-Lasers and Optics*, vol. 65, pp. 115-135, 1997.
- [15] M. Yamashita, M. Ishikawa, K. Torizuka, and T. Sato, “Femtosecond-Pulse Laser Chirp Compensated By Cavity-Mirror Dispersion,” *Optics Letters*, vol. 11, pp. 504-506, 1986.
- [16] N. Matuschek, F. X. Kartner, and U. Keller, “Analytical design of double-chirped mirrors with custom- tailored dispersion characteristics,” *IEEE Journal of Quantum Electronics*, vol. 35, pp. 129-137, 1999.
- [17] F. X. Kartner, N. Matuschek, T. Schibli, U. Keller, H. A. Haus, C. Heine, R. Morf, V. Scheuer, M. Tilsch, and T. Tschudi, “Design and fabrication of double-chirped mirrors,” *Optics Letters*, vol. 22, pp. 831-833, 1997.
- [18] H. A. MacCleod, *Thin film optical filters*: Institute of Physics, 2000.
- [19] M. Mazilu, “Chromatic interaction between light and optoelectronic multilayer structures,” PhD. Thesis, University of St Andrews, 1999.
- [20] A. Robertson, U. Ernst, R. Knappe, R. Wallenstein, V. Scheuer, T. Tschudi, D. Burns, M. D. Dawson, and A. I. Ferguson, “Prismless diode-pumped mode-locked femtosecond Cr : LiSAF laser,” *Optics Communications*, vol. 163, pp. 38-43, 1999.

Chapter 3 - Tuning of compact Cr: LiSAF lasers using a novel birefringent filter

3.1 Introduction

Cr: LiSAF is a versatile laser crystal that has a high stimulated emission cross-section upper state lifetime product. This crystal has been used in the construction of a range of low-threshold and efficient laser systems [1-3] and such lasers have been operated at gigahertz repetition rates (see chapter 4) [4], kilowatt peak power levels and in single pass extracavity frequency-doubled configurations used to generate femtosecond pulses in the blue spectral region [5]. These laser configurations were designed to have a fixed centre wavelength whereas for many applications, such as nonlinear optics and pump-probe spectroscopy, there is a requirement to tune the centre wavelength of the femtosecond pulses over tens of nanometres. In this chapter, three different techniques for tuning a modelocked laser are discussed and two different techniques of tuning a modelocked Cr: LiSAF laser are implemented and compared. Firstly, a single prism is used in a Cr: LiSAF laser cavity as both a tuning element and as the source of negative dispersion required for stable cw modelocking. Secondly, a combination of multiple cavity Gires-Tournois interferometer (MCGTI) mirrors for dispersion compensation and a specially designed birefringent filter (BRF) are used to tune the centre wavelength.

3.2 Three techniques for tuning a modelocked laser

Three common methods of tuning a modelocked laser are shown in figure 3.1, these are (i) the use of a single-prism [6], (ii) a combination of two prisms and a slit [7], and (iii) the use of a dispersive mirror to compensate for pulse broadening through the crystal and a birefringent filter (BRF) to tune the centre wavelength of the modelocked laser [8]. The first technique, shown in the figure 3.1(a), relies on slight decollimation of the long arm of the laser cavity. A prism is inserted into this arm and hence the beam is angularly dispersed when it reaches the output coupler. This angular dispersion means that when either the

prism or the output coupler is tilted the laser will be subject to wavelength selective feedback and hence the centre wavelength of the laser can be selected. The negative dispersion is geometric in origin and relies on the crossing of the rays before the prism to cause the same effect as having the apex of a second prism at the crossing point, hence this technique is intrinsically the same as using two prisms. This is more fully described in reference [6].

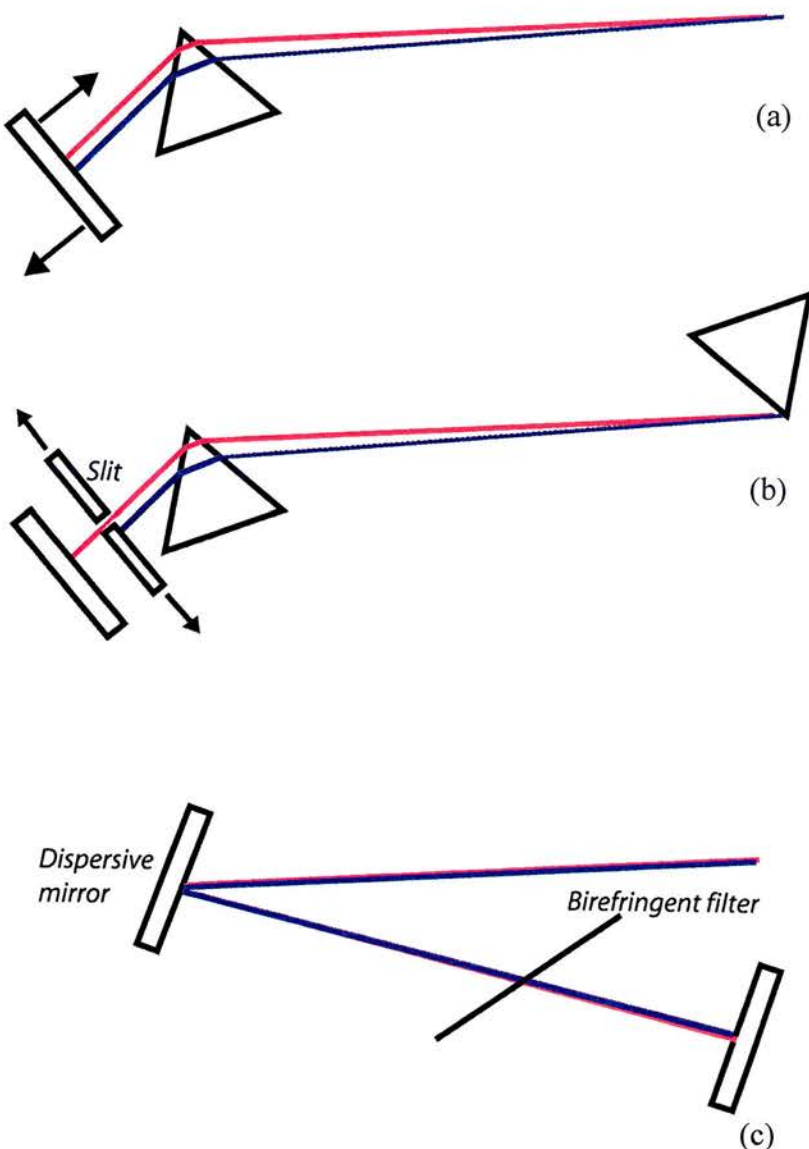


Figure 3.1: Three techniques employed to tune the centre wavelength of a modelocked laser. (a), a single prism may be used for both negative dispersion and tuning, (b), two prisms and a slit, (c), the combination of a dispersive mirror and birefringent filter.

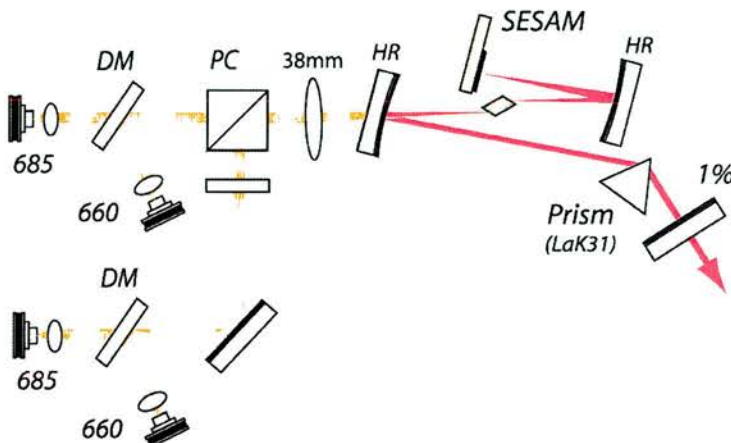


Figure 3.2: A cavity configuration for the tuning of a Cr: LiSAF laser over 50nm, [HR-highly reflecting mirror, DM-dichroic mirror, PC-polarising cube].

The laser shown in figure 3.2 was constructed to investigate single prism tuning. Tuning of the centre wavelength of around 50nm was observed and this was believed to be limited by the reflectivity of the back mirror of the SESAM rather than by dispersion. The change in pulse properties as the laser is tuned can be seen in figure 3.3 along with the reflectivity of the SESAM back mirror [9].

The second technique, in figure 3.1(b), relies on the use of two prisms and ensures that the beam is collimated, but spatially dispersed after the second prism. Thus translation of a slit of appropriate width allows frequency selective feedback and so the centre wavelength of the laser can be changed. The origin of the negative dispersion in this arrangement is discussed in chapter 1.

The third technique, illustrated in figure 3.1(c), involves the separation of the two requirements of tuning and dispersion compensation into two discrete intracavity components. The dispersion compensation, in the case of the work discussed in this chapter, comes from the use of broadband dispersive mirrors known as multiple-cavity Gires-Tournois interferometer mirrors, or MCGTI mirrors, and the frequency selection is provided by the use of a specially designed birefringent filter.

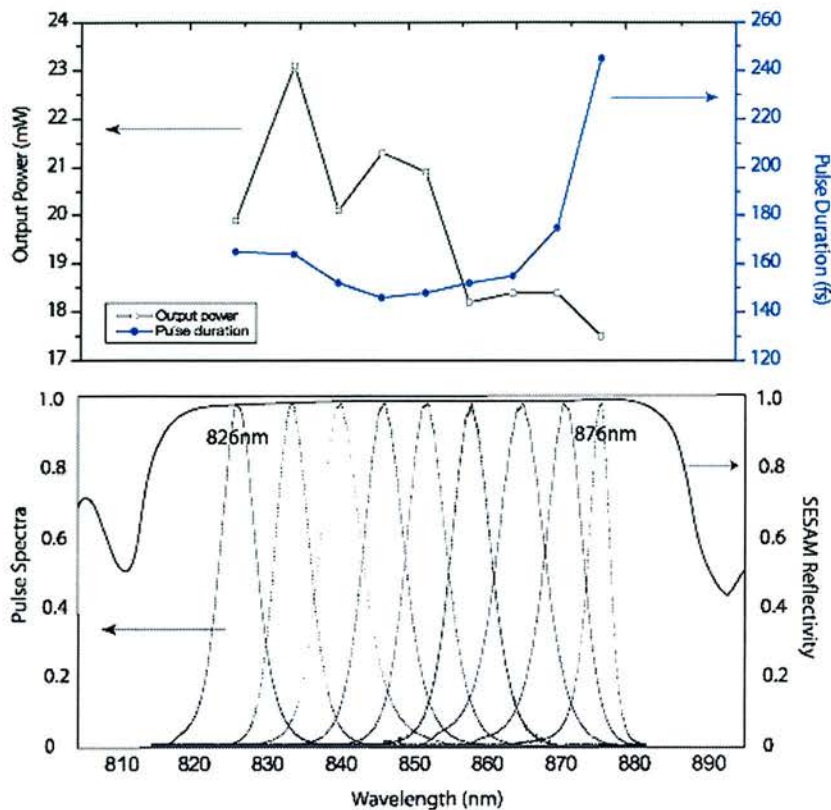


Figure 3.3: The change in pulse properties as the laser is tuned over 50nm, shown alongside the reflectivity of the SESAM back mirror.

There are several advantages and disadvantages associated with each technique; Tuning with a single prism has the advantage that it keeps the cavity length relatively short and thus the footprint of the laser system can be relatively compact. It also has the advantage that by translating the prism, i.e. inserting more or less glass into the laser cavity, one can increase or decrease the GDD it contributes. It is very difficult, however, to compensate for higher-order dispersion using this technique. Using two prisms increases the footprint of the cavity somewhat, but it does allow some compensation for higher-order dispersion through appropriate selection of the prism material [10]. The use of a BRF and a dispersive mirror has the obvious disadvantage of not being able to adjust the magnitude of the dispersion compensation to the same extent as the other techniques. However, this method does have the valuable advantage of removing the prism separation requirement altogether and thus the size of the laser cavity can be further reduced.

Conventional birefringent filter design [11] provides excellent tuning elements for single frequency lasers. The challenge of tuning a femtosecond laser, where one wishes to modify the centre wavelength of a larger spectral width, potentially several nanometres to several tens of nanometres, is clearly rather different. Naganuma and co-workers [12] have demonstrated that by utilising a birefringent plate where the optic axis dives into surface of the plate, a birefringent filter of improved utility for colour centre lasers can be designed. It is this idea that is adapted and studied in the remainder of this chapter.

A birefringent filter has allowed Golubovic et al. [8] to demonstrate an 80MHz Kerr-Lens modelocked (KLM) Ti: Sapphire laser tunable over 100nm. A conventional birefringent filter consisting of a 2mm thick birefringent plate, was used to tune the centre wavelength of this laser. In the context of a low-threshold system, this plate would have suppressed lasing in the region around the central pass-band to a very high degree. This means that if this plate had been used in a Cr: LiSAF laser, it would not have produced femtosecond pulses. This idea is outlined conceptually in figure 3.4.

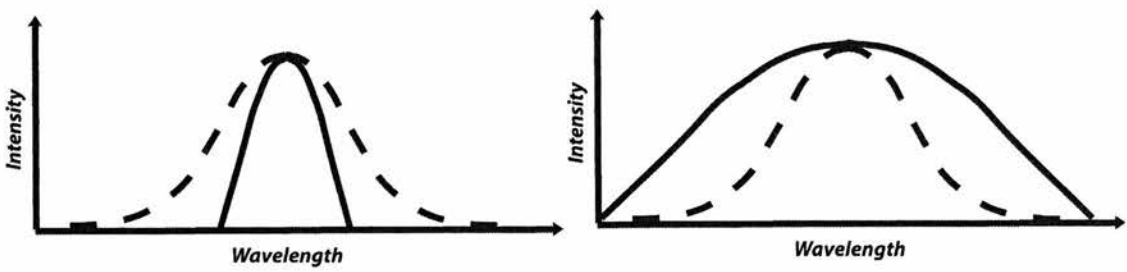


Figure 3.4: The difference in oscillating bandwidth of a standard filter (left) and a filter with a steeply diving optic axis (right) of the same thickness. Free running spectral bandwidth is shown as a dotted line and the passband of the BRF is shown as the solid line.

The constriction of optical bandwidth is the main limitation that must be overcome when tuning a low-gain laser with a birefringent filter. The next section discusses the design of the filter and the adaptations to existing filter designs that have been made to achieve this goal.

3.3 Tuning using a birefringent filter and multiple cavity Gires-Tournois interferometer mirrors

3.3.1 Introduction: how tunability and negative GDD is achieved

A birefringent filter is a thin birefringent crystal coupled with some polarisation dependent loss [13]. It is arranged such that the incident light is not polarised perpendicularly or parallel to the crystal axis which means that light entering the crystal will have both extraordinary and ordinary components. Figure 3.5 shows a birefringent filter made from two polarisers and a birefringent plate. The polarisation state of the light entering the plate can be decomposed into a superposition of components representing the magnitude of the light polarised along the crystal axis and that polarised along the axis orthogonal to the crystal axis. As the light propagates through the crystal there is a change of phase between these two beams. Only wavelengths for which this phase change is an integral multiple of 2π have an unaltered polarisation state. Hence only such light will experience maximum transmission through the polarisers. Rotation of the plate will alter the refractive indices experienced by the components and so the effective birefringence offered by the plate will be changed. This means a different group of wavelengths will experience a full-wave plate as they propagate through the crystal. The polarisers in the case of the Brewster-angled plate are inherent in the plate itself, since p-polarised light will see no reflection loss whereas s-polarised light will. Thus, tuning of the laser is achieved.

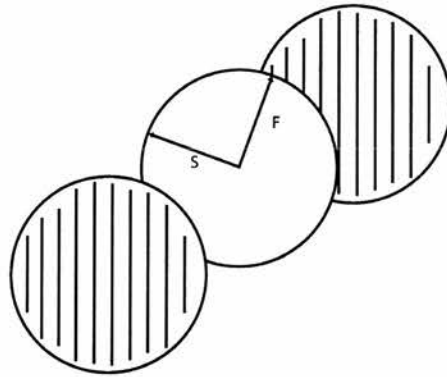


Figure 3.5: Two polarisers in series with a birefringent plate to act as a birefringent filter. F and S designate the axes defining the birefringence of the plate.

Although the tunability is supplied by the BRF, a source of negative group delay dispersion (GDD) is still required to compensate for pulse temporal broadening through the crystal and allow the stabilisation of femtosecond pulses. Extensive research by a number of groups has led to the development of mirror-based dispersion compensation schemes, such as chirped mirrors and Gires-Tournois interferometer mirrors (GTIs) [14] that have a number of advantages over prism-based dispersion compensation. These mirror-based dispersion compensation schemes are discussed more fully in chapter 2 of this thesis. The MCGTI mirrors used in this project were provided by Prof. Robert Szipocs (*R&D Lezer-Optika Bt., Budapest*) as part of an on-going collaboration.

3.3.2 Modelling of the filter using Jones matrix algebra

The study of optical systems which act on the polarisation state of incident light, such as birefringent filters, can be eased by decomposing the incident field into its polarisation components that can be represented in vector form [14,15]. A Jones matrix, M, can then be used to describe the action of each element in an optical system on the polarisation state of the light, as shown in equation 1.

$$\begin{pmatrix} E_{p,out} \\ E_{s,out} \end{pmatrix} = M \begin{pmatrix} E_{p,in} \\ E_{s,in} \end{pmatrix} \quad (1)$$

Where $E_{p,out}$, $E_{s,out}$ are the output electric field components polarised in the p and s direction. M, the Jones' matrix for the system, is a 2 x 2 matrix that describes the effect of the optical element or elements on the polarisation. $E_{p,in}$ and $E_{s,in}$ are the input electric field components polarised in the direction parallel to the Brewster surface, p, and the perpendicular, s, direction.

Previous work on tuning a modelocked laser with a birefringent filter was based upon the use of high gain materials such as a colour centre [12] or Ti: sapphire [8] crystals. However, choosing a filter for use in low-gain modelocked lasers such as diode-pumped Cr: LiSAF lasers is a rather involved process. It is not necessary for a filter to impose high losses on wavelengths far away from the central pass-band because the gain is insufficient for lasing in that region. Similarly, it is not appropriate to reference the pass-band to half maximum transmission, since lasing will be suppressed at significantly higher transmissions. A typical output coupling for these lasers is around 1%, so the 99% transmission widths are a more realistic and useful reference for compact, low-threshold Cr: LiSAF lasers.

Steeply diving optic axis filters [12] have a number of advantages over the case where the crystal axis of the filter is in the plane of the crystal. These are, (i) there are a number of filter properties that can be adjusted through sufficient azimuthal rotation of the filter to access different tuning characteristics, (ii) for the same filter bandwidth, the required thickness of a non diving axis filter to maintain the same wide transmission peaks is five times thinner. Use of a thicker filter will reduce etalon effects. It will also improve handling, and (iii) very broad tunability is possible without deterioration in the depth of the stop band, through appropriate selection of the dive angle.

In a regular birefringent filter arrangement, if the phase difference between the extraordinary and ordinary components, for a particular centre wavelength, is equal to an integral number of 2π then that wavelength will experience high transmission. In a conventional device there is no real difference between $2\pi, 4\pi, 2m\pi$, etc., but in a filter that has a steeply diving optic axis, the filter properties will depend on the integer, m [12]. This manifests itself in a different spectral pass bandwidth and a different tuning velocity associated with each value of m. In turn, this means that a filter such as this can be used to force the

laser to oscillate with a certain bandwidth and so affect the output pulse duration.

Naganuma et al. [12] define a quality factor for birefringent filters. This quality factor is a measure of how the stop band deteriorates as the centre wavelength of the pass-band is changed. They show that a maximum in this quality factor is found at a dive angle of 66 degrees. However, the manufacture of these plates was likely to be expensive, and as Leysop Ltd. produce plates with a dive angle of 57 degrees, it was thought this cheaper alternative was a viable option. Also, as discussed later, the 57 degree filter is also more appropriate in terms of its tuning velocity for use in a low threshold femtosecond laser system.

Naganuma et al. [12] show that properties of such a filter can be modelled by constructing the Jones matrix of a round-trip of a linear cavity containing the filter together along with the loss associated with the Brewster surfaces. Figure 3.6 contains a diagram showing the important angles used to construct this matrix. The plate has a thickness L . Intracavity light will enter the plate with an incidence angle denoted by ϕ , which is a constant in later calculations. The optic axis is not in the plane of the plate, as is the case in standard birefringent filters, but rather makes the angle θ with the surface of the plate. Tuning is achieved through azimuthal rotation of the plate, a change in the angle α . As α is increased the optic axis will trace out a cone with an apex in the plane of the filter.

The plates described in this chapter are made from crystalline quartz, a uniaxial crystal, and so an increase in the angle θ will decrease the effective birefringence of the plate. This decrease occurs because an increase in θ will make the difference between the refractive index experienced by the extraordinary ray more similar in magnitude to that experienced by the ordinary ray. As the angle α is changed, through azimuthal rotation of the plate, the refractive index experienced by the extraordinary ray is also changed. This, in turn, changes the birefringence offered by the plate. It is through changing the angle α that continuous tuning is achieved.

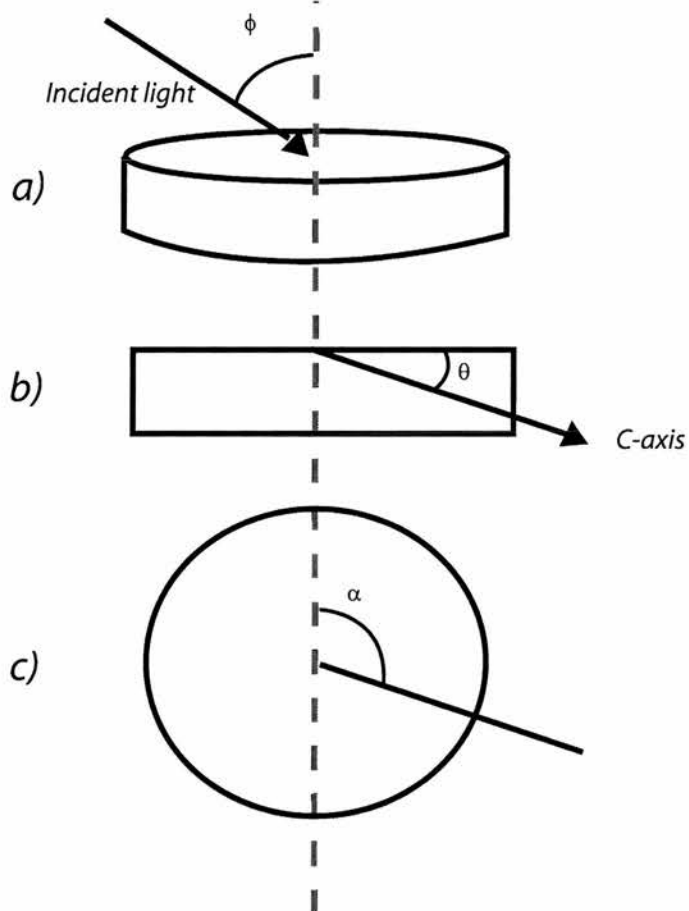


Figure 3.6: a) Isometric view showing incident light entering the plate with incidence angle ϕ , b) side elevation showing that the optic axis makes an angle θ with the surface of the plate, c) plan view showing the definition of the azimuthal angle α which allows tuning of the filter.

In order to construct the required Jones matrix that describes the filter, M, first consider the phase difference incurred between the extraordinary and ordinary components as the light propagates through the birefringent filter. This situation is confused because the extraordinary polarisation is no longer in the plane of the crystal. Naganuma shows that the phase change between the extraordinary component and the ordinary component through the crystal can be given by,

$$\Theta = f_b \cdot (k \cdot \delta \cdot L / \cos \phi) \quad (2)$$

here k is the wavenumber, δ is the magnitude of the birefringence, and f_b is given by

$$f_b \equiv \sin^2 \gamma = \cos^2 \theta \sin^2 \alpha + (\cos \phi \cos \theta \cos \alpha - \sin \phi \sin \theta)^2 \quad (3)$$

where γ is the angle between the direction of propagation and the c-axis of the crystal. Each filter order (the number of full wave retardations between the extraordinary and ordinary polarisation components) must be an integer and this means that a solve block can be used to determine the wavelength which will experience maximum transmission through the effective filter system. However, to determine the spectral width of each filter maximum the eigenvalues of Naganuma's full Jones matrix must be determined and this is given by,

$$M = \begin{pmatrix} 1 & 0 \\ 0 & q \end{pmatrix} \begin{pmatrix} \sin \alpha_{eq} & \cos \alpha_{eq} \\ -\cos \alpha_{eq} & \sin \alpha_{eq} \end{pmatrix} \begin{pmatrix} 1 & 0 \\ 0 & e^{i\Theta} \end{pmatrix} \begin{pmatrix} \sin \alpha_{eq} & -\cos \alpha_{eq} \\ \cos \alpha_{eq} & \sin \alpha_{eq} \end{pmatrix} \begin{pmatrix} 1 & 0 \\ 0 & q \end{pmatrix} \quad (4)$$

The first term in this expanded Jones matrix defines the loss experienced by the s-polarisation on entry and exit from the crystal. The factor q is the regular Fresnel transmission coefficient,

$$q = \frac{2n}{(n^2 + 1)} \quad (5)$$

where n is the refractive index experienced by the polarisation that is subject to high loss. The second and fourth terms are the rotation matrices which decompose the incoming light into extraordinary and ordinary components and α_{eq} is given by,

$$\cos \alpha_{eq} = (\cos \phi \cos \theta \cos \alpha - \sin \phi \sin \theta) / \sin \gamma \quad (6)$$

and α_{eq} is the equivalent azimuthal angle which takes into account ray propagation through the crystal. It should be noted that this model does not take into account the birefringence of the gain medium although this could be done with some adaptation [18]. The third term in this expanded Jones matrix describes the phase change between the extraordinary and ordinary ray on

propagation through the crystal. The results for several different plates can be seen in figure 3.7.

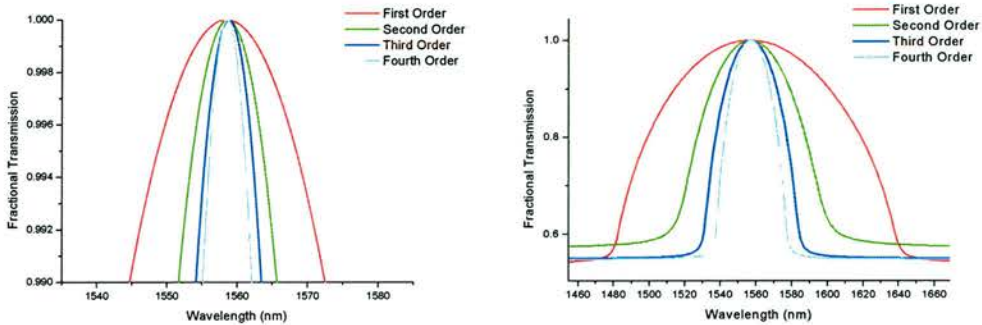


Figure 3.7 a) Spectral widths of the first four filter orders of a 1.85mm thick birefringent plate with a 66 deg optic axis dive angle, the filter described in Naganuma et al. [12].

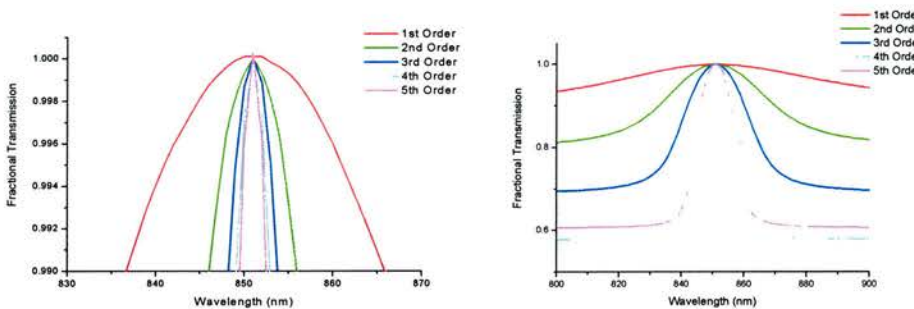


Figure 3.7 b) The spectral widths associated with the first six filter orders of a 0.66mm thick birefringent plate with a 57 deg. optic axis dive angle. The plate used to tune the lasers described in this chapter.

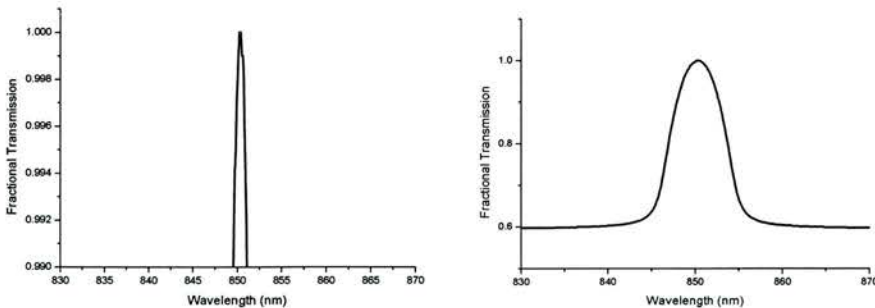


Figure 3.7 c) The spectral width of the pass-band associated with a 1mm thick plate with a zero degree optic axis dive angle (i.e. no dive)

Figure 3.7 (b) relates to the filter designed for Cr: LiSAF lasers which is a 0.66mm quartz plate with an optic axis which dives into the plate at an angle of 57 degrees. It has transmission widths of the first to sixth filter orders of 29nm, 10nm, 6nm, 4nm, 3nm, and 4nm. The wider transmission bandwidth correspond to a lower filter order whereas the narrower transmission bandwidths correspond to the higher filter orders.

Figure 3.7 c) relates to the expected transmission from a regular birefringent plate, i.e. a 1mm thick plate in which the optic axis is in the plane of the filter. Figure 3.7 (a) relates to a filter design for a $1.5 \mu\text{m}$ colour centre laser, specifically a 1.85mm thick quartz plate with a optic axis which dives at an angle of 66 degrees, designed in [12]. The filter properties shown in figure 3.7 (a) have spectral widths of the first to fourth filter orders of 28nm, 14nm, 8nm, and 6nm.

The model was then used to predict the tuning velocity of the first six filter orders of the 57 degree plate and this is shown in figure 3.8. Starting with the known phase change, i.e. $2m\pi$, and calculating which wavelength will experience that phase change at a particular filter rotation allowed the tuning velocity to be calculated. As can be seen from figure 3.8 there is a correlation in tuning velocity and pass-band. Namely, the lower the filter order, the broader its associated pass-band and the faster the centre wavelength of this pass-band tunes with respect to azimuthal filter angle.

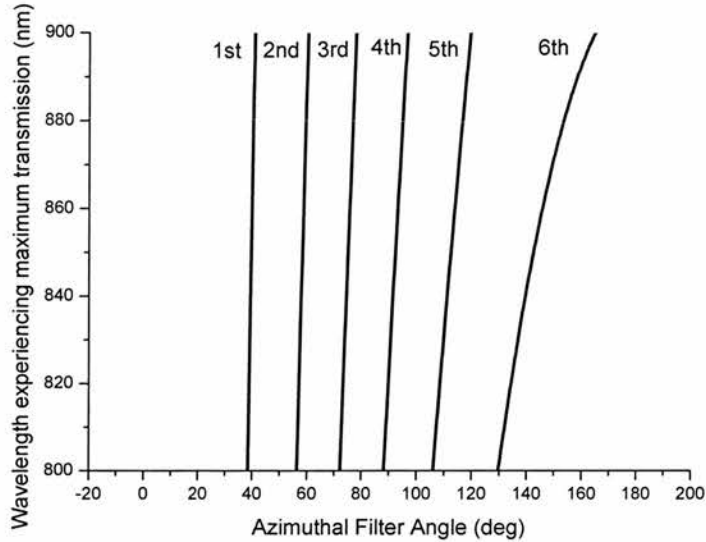


Figure 3.8: Theoretical tuning velocities for the first six filter orders of a 0.66mm thick quartz plate with a 57 degree optic axis. First order 40 nm/deg, second order 25 nm/deg, third order 17 nm/deg, fourth order 12 nm/deg, fifth order 7nm/deg, sixth order 3 nm/deg.

In terms of tuning velocity the 57 degree dive angle filters are superior to the 66 degree dive angle filters in the context of low gain femtosecond lasers. Each filter order tends to tune at a much lower rate with the 57 degree filter than with the 66 degree filter. For example, the first order of the Naganuma filter tunes at 45 nm/deg whereas the 57 degree filter tunes at 40 nm/deg, the second order of the Naganuma filter tunes at 36 nm/deg whereas the second order of the 57 degree filter tunes at 25 nm/deg. This makes the lower filter orders of the 57 degree filter more usable than those of the Naganuma filter, since a lower degree of precision will be required when rotating the 57 degree filter.

3.3.3 Conclusions

In this section Jones matrix algebra has been explained and introduced as useful tool when it comes to understanding the polarisation changes undergone by light when it traverses an optical system. It has explained how a thin birefringent plate, in conjunction with some polarisation dependent loss, can be used as a wavelength selective element. The specific case of a steeply diving optic axis filter was shown to be superior to the non-diving optic axis filter. A number of

factors influenced the choice of filter for the modelocked Cr: LiSAF laser, among them cost, constriction of optical bandwidth, and tuning velocity. The filter used in the experimental work was a 0.66mm thick quartz plate with a 57 degree diving optic axis. The following section details the successful use of this plate as a tuning element in a modelocked Cr: LiSAF laser.

3.4 Steeply diving optic axis birefringent plate as an intracavity tuning element

3.4.1 Tuning of a cw laser

The laser shown schematically in figure 3.9 was constructed as described in [3]. The laser had a total incident pump power of 180mW and an overall electrical-to-optical efficiency of around 4%. The data in figure 3.10 show the change in centre wavelength and output power of the cw laser as the filter is rotated, i.e. with a high-reflecting mirror in place of the SESAM. The theoretical predictions of the tuning velocity, in terms of nm/deg, for the first and second orders are 40nm/deg and 25nm/deg respectively, but the experimentally obtained tuning velocities are 10nm/deg and 19nm/deg. This discrepancy is most likely caused by the fact that these two filter orders have the widest 99% pass widths (29nm and 10nm). Hence, the centre wavelength is not tightly constrained by the filter, at least around the centre of the pass band, and may be more considerably influenced by the gain-loss balance characteristic of the free-running laser, particularly towards the edges of the tuning range. This poor definition is evident in the ‘s-shape’ of the lower order tuning curves. This shape demonstrates only weak constraint on the oscillating wavelengths. It should be noted that the model used to describe the filter does not contain any wavelength dependent gain and loss, in other words it is a ‘cold cavity’ model. Filter orders 3-6 show very good agreement between the theoretical tuning velocity and that obtained experimentally. It should also be noted that these orders have the slowest tuning velocities and narrowest pass-bands. This means that there will be a higher degree of constraint on the oscillating wavelength.

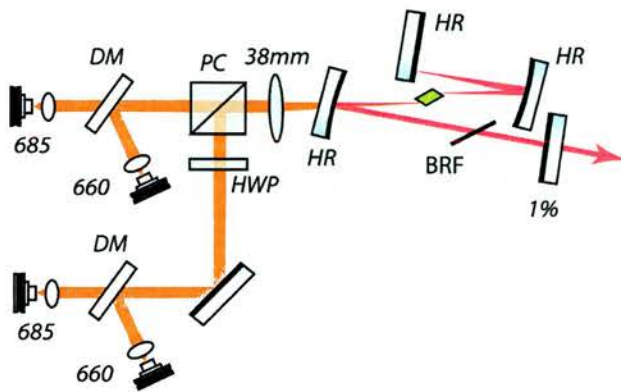


Figure 3.9: Schematic of laser used in the cw tuning experiments

A comparison between theoretical and experimentally obtained tuning velocities can be found in table 3.1. In this table, direct correlation between the theoretical and experimental tuning velocities for the higher filter orders can be seen whereas for the lower filter orders the agreement is not so good.

It can be seen from the data presented in figure 3.10 that in a cw laser configuration these birefringent filters can tune the Cr: LiSAF laser over a spectral region of over 80nm in most cases. This is certainly influenced by the reflectivity bandwidth of the mirror set used and the wavelength-dependent change in stimulated emission cross-section associated with the crystal.

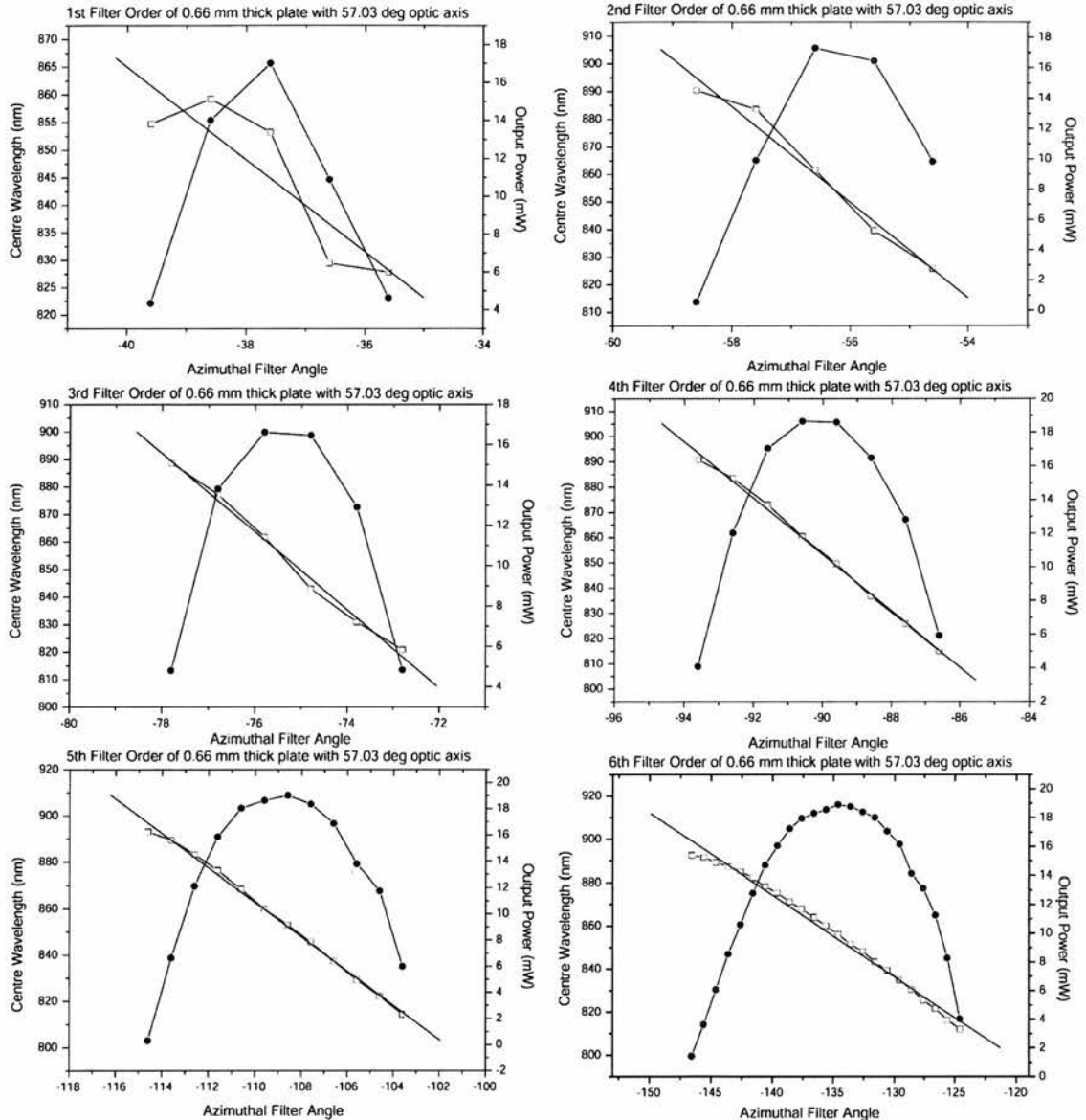


Figure 3.10: Measured cw tuning characteristics together with the best-fit straight line.

Filter Order	Tuning Velocity (Experimental)	Tuning Velocity (Theoretical)
1	10 nm/deg	40 nm/deg
2	19 nm/deg	25 nm/deg
3	14 nm/deg	17 nm/deg
4	11.6 nm/deg	12 nm/deg
5	7.4 nm/deg	7 nm/deg
6	3.7 nm/deg	3 nm/deg

Table 3.1: Direct comparison between the theoretical and experimental tuning characteristics for a 0.66mm quartz plate with a 57 degree optic axis dive angle.

3.4.2 Tuning of a modelocked laser

3.4.2.1 Preliminary work on tuning of a modelocked laser

Before modelocking was initiated, a simple mathematical model was built up from the round-trip dispersion of the laser cavity. This was constructed using the dispersion data from the LTR predictions of the SESAM [19], the measured dispersion data of the MCGTI-mirrors provided by Prof. Szipocs, the theoretical dispersion data associated with the laser crystal [20] and the well known Sellmeier equations for quartz. This provided a good basis in understanding the change in the optical spectrum of the output when tuning these low-threshold lasers. An interesting example is the laser system shown schematically in figure 3.11.

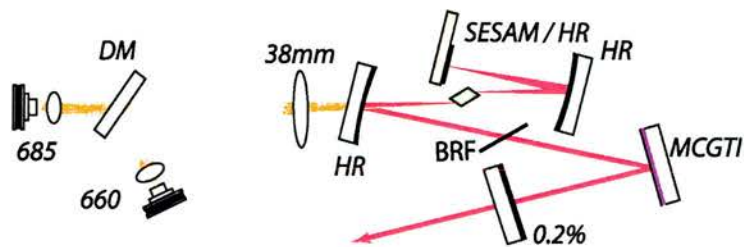


Figure 3.11: Schematic of the laser cavity used in preliminary tuning experiments on a modelocked Cr: LiSAF laser.

This laser system provided the broadest tuning range of any of the lasers that will be discussed subsequently, despite its modelocked output power being less than any of the later systems which made use of two pairs of pump diodes and higher fractional output couplings. This meant that the temporal characterisation that was carried out on subsequent systems could not be achieved using the laser cavity in figure 3.11.

The measured cw tuning characteristics indicated that the third filter order was used. This may have constricted the modelocked bandwidth somewhat but the results are interesting nonetheless.

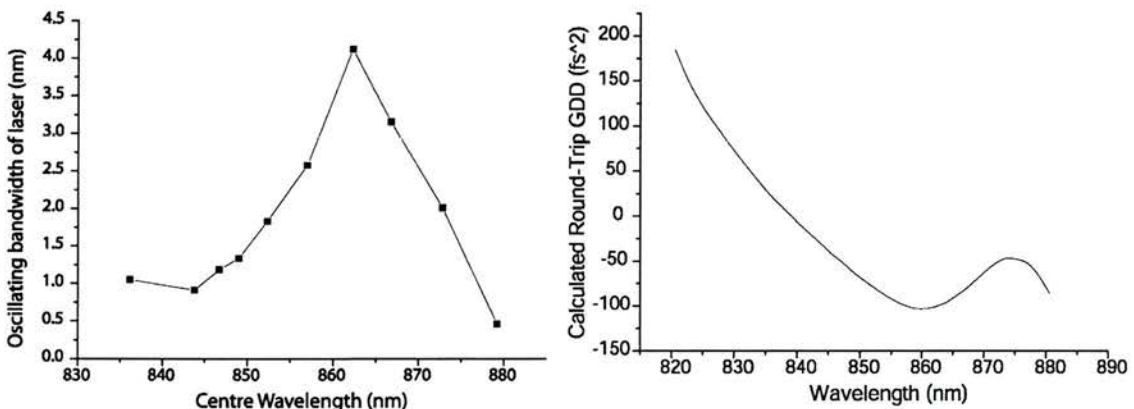


Figure 3.12: Tuning characteristics and corresponding round-trip GDD

As can be seen from figure 3.12 the laser modelocked over a very broad tuning range, extending from 850nm to ~875nm indicated by broadening of the output spectral bandwidth. As the laser was tuned, the bandwidth increased as the net GDD decreased until it reached the minimum in GDD at just over 860nm. This

point represents zero third-order dispersion (TOD) and is also the point where the optical bandwidth of the modelocked laser changes from 2.5nm to over 4nm. This behaviour shows a clear dependence of the maximum bandwidth, achievable with any particular laser setup, on the round-trip dispersion. It should be noted that the filter bandwidth had not changed across this tuning range and had a 99% width of 6nm.

3.4.2.2 Tuning the ‘double-pumped’ modelocked Cr: LiSAF laser

The laser that offered the broadest tuning range using two pairs of pump diodes was the laser shown in figure 3.13. With the SESAM in place, the laser modelocked and allowed for around 20nm of tunability of the centre wavelength. This tuning range is limited by dispersion and not by the back mirror or saturable absorption associated with the SESAM. The result noted earlier where 50nm of tunability was achieved with a single prism is clear evidence of this.

The same model used in the previous section was used to calculate the net round-trip dispersion of the laser cavity. As can be seen from the plots in figure 3.14, the round-trip dispersion in the cavity is significantly negative.

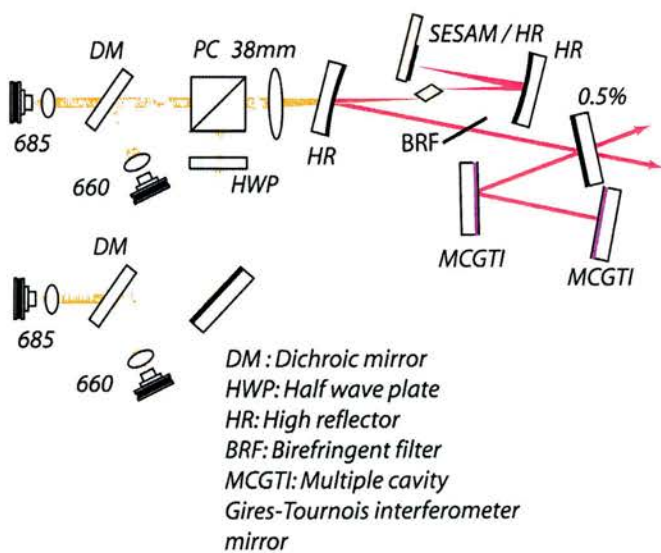


Figure 3.13: Schematic of laser used in modelocked tuning experiments

The large magnitude of this negative GDD is due to the lack of consideration for pulse broadening due to self phase modulation. This does, however raise the question of whether or not the pulses would be significantly shorter if the laser could be tuned to around 865nm, where the gradient of the GDD and hence the net third-order dispersion (TOD) approaches zero. It should be noted that optimisation of both the GDD and TOD for sub-100fs pulses will prove extremely difficult, and may require further reflections on MCGTI/GTI mirrors to negate the excess GDD and TOD. These extra reflections would increase the threshold pump power for lasing in a low-gain Cr: LiSAF laser.

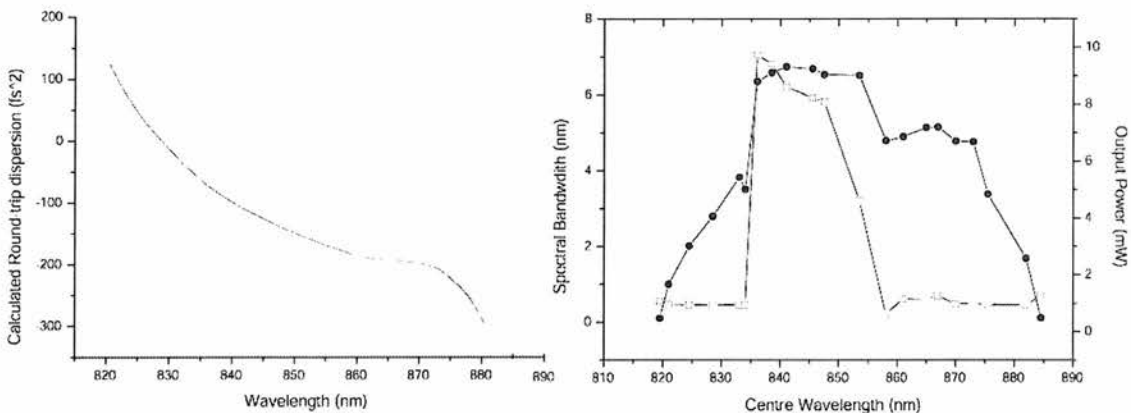


Figure 3.14: Calculated round-trip dispersion (left) and the change in pulse properties (right) over 20nm of centre wavelength tuning

Also shown in figure 3.14 is the change in spectral bandwidth and output power over 20nm of tuning with the second filter order. In this case the laser is modelocked between 840nm and 860nm, where the spectral bandwidth and output power increase significantly.

The effect of constriction of optical bandwidth using higher filter orders was then investigated. From the filter model, see 3.3.2, it can be seen that as the filter order increases, the spectral width of the pass-band decreases. For each filter order the SESAM was replaced by an HR mirror and its cw tuning velocity was then measured. This tuning velocity was then used to identify the filter order using table 3.1. The maximum bandwidth achieved was then monitored as the laser was tuned over its entire tuning range. Figure 3.15 shows the maximum spectral bandwidth that could be achieved when tuning with each filter order

plotted alongside the theoretical 99% width of each pass band. As can be seen from figure 3.14 the 99% width does constrict the modelocked bandwidth of the laser to a value similar to the 99% width of a given filter order and so can be used to force the laser to oscillate with a desired spectral bandwidth and hence desired pulse duration.

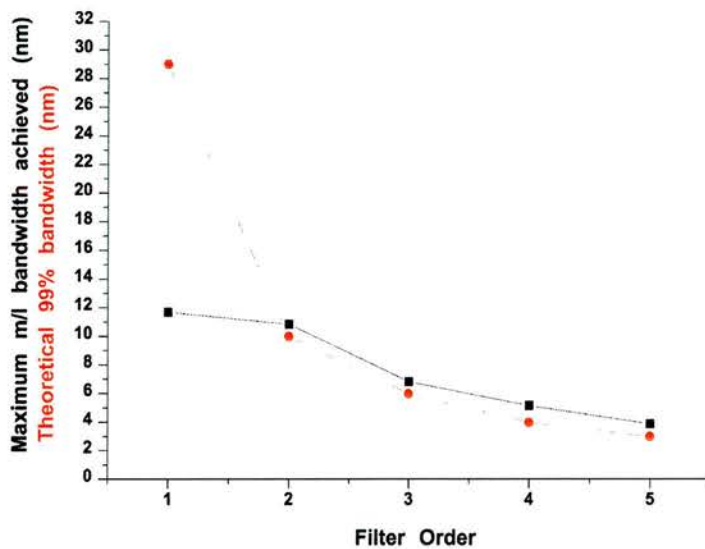


Figure 3.15: Maximum bandwidth achieved with each filter order shown alongside the 99% width of the filter order.

The free-running modelocked bandwidth of the laser is significantly less than the 99% width of the first filter order and so the laser could not ‘fill’ the bandwidth provided by the first filter order.

An autocorrelator was then used to measure the pulse duration over ~20nm of tuning in order to investigate the change in pulse duration and general pulse properties as the laser is forced to change its centre wavelength and hence alter the round-trip dispersion experienced by the pulse. Figure 3.16 shows the difference in pulse duration over ~20nm of centre wavelength tuning when tuning using the second filter order in comparison to the fourth filter order. As is immediately evident, the pulse duration achieved with the second filter order (which allowed the greater bandwidth to be transmitted) is significantly shorter than the pulse duration achieved with the fourth filter order. In the case of the second filter order the minimum pulse duration that could be achieved was around 130fs whereas the minimum pulse duration that could be achieved with

the fourth filter order was 260fs. Shown on the same graph is the duration-bandwidth product measured over this tuning range. Although this fluctuates as the laser is tuned over 20nm in both cases it does have the same excursion in both cases, which means that the filter order used has very little effect on the chirp of the output pulse. This appears to be determined by the net dispersion seen by the pulse and is strongly dependent on centre wavelength and bandwidth.

The results shown here do not seem to correlate with the theory of soliton modelocking in [21] which describes a dependence of pulse duration on the magnitude of the round-trip dispersion but does not allow for the chirped pulses (duration/bandwidth product = 0.44) seen in these experiments. One explanation is that this modelocking theory does not account for third order dispersion or any pulse shaping that may occur through fast time gating of the pulse by the saturable absorber.

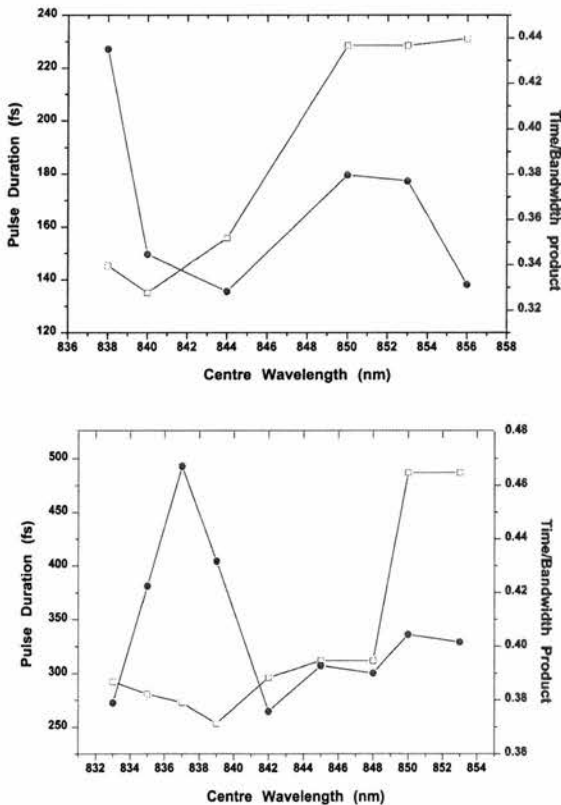


Figure 3.16: The change in pulse duration when tuning with the second filter order (upper) and with the fourth filter order (lower).

3.5 Conclusions

In this chapter, two methods of tuning modelocked Cr: LiSAF lasers have been implemented and discussed. One method used a single prism to provide tuning of the centre wavelength over 50nm, limited by the reflectivity of the SESAM back mirror. The second technique uses the combination of MCGTI mirrors and a specifically designed birefringent filter to support femtosecond pulses with tunability of the centre wavelength over 20nm. This tuning range is limited by the round-trip dispersion provided by the MCGTI mirrors. The filter was designed with the low-gain Cr: LiSAF material in mind and so had very broad 99% transmission widths at the expense of the suppression of the neighbouring wavelengths. The properties of the filter were studied and it was found that the oscillating bandwidth of the laser could be controlled simply through the rotation of the intracavity plate. The implications of this rotation on pulse duration was investigated and found that the magnitude of the chirp on the pulse remains relatively unaffected when a different filter order is used. Constriction of the optical bandwidth, through selection of a specific filter order allows ‘designer’ pulse durations. These filters may open new avenues in pulse characterisation. A sonogram [22] setup cross-correlates a pulse with its frequency-filtered replica, so a birefringent filter similar to those described in this chapter could be designed and placed in one arm of a regular autocorrelator setup in order to acquire a sonogram trace quickly and easily.

References

- [1] J. M. Hopkins, G. J. Valentine, B. Agate, A. J. Kemp, U. Keller, and W. Sibbett, “Highly compact and efficient femtosecond Cr : LiSAF lasers,” *IEEE Journal of Quantum Electronics*, vol. 38, pp. 360-368, 2002.
- [2] J. M. Hopkins, G. J. Valentine, W. Sibbett, J. A. der Au, F. Morier-Genoud, U. Keller, and A. Valster, “Efficient, low-noise, SESAM-based femtosecond Cr³⁺: LiSrAlF₆ laser,” *Optics Communications*, vol. 154, pp. 54-58, 1998.
- [3] B. Agate, B. Stormont, A. J. Kemp, C. T. A. Brown, U. Keller, and W. Sibbett, “Simplified cavity designs for efficient and compact femtosecond Cr : LiSAF lasers,” *Optics Communications*, vol. 205, pp. 207-213, 2002.
- [4] A. J. Kemp, B. Stormont, B. Agate, C. T. A. Brown, U. Keller, and W. Sibbett, “Gigahertz repetition-rate from directly diode-pumped femtosecond Cr : LiSAF laser,” *Electronics Letters*, vol. 37, pp. 1457-1458, 2001.
- [5] B. Agate, A. J. Kemp, C. T. A. Brown, and W. Sibbett, “Efficient, high repetition-rate femtosecond blue source using a compact Cr : LiSAF laser,” *Optics Express*, vol. 10, pp. 824-831, 2002.
- [6] D. Kopf, G. J. Spuhler, K. J. Weingarten, and U. Keller, “Mode-locked laser cavities with a single prism for dispersion compensation,” *Applied Optics*, vol. 35, pp. 912-915, 1996.
- [7] J. P. Gordon and R. L. Fork, “Optical-Resonator With Negative Dispersion,” *Optics Letters*, vol. 9, pp. 153-155, 1984.
- [8] B. Golubovic, R. R. Austin, M. K. Steiner-Shepard, M. K. Reed, S. A. Diddams, D. J. Jones, and A. G. Van Engen, “Double Gires-Tournois interferometer negative-dispersion mirrors for use in tunable mode-locked lasers,” *Optics Letters*, vol. 25, pp. 275-277, 2000.
- [9] B. Stormont, B. Agate, A. J. Kemp, C. T. A. Brown, W. Sibbett, and R. Szipocs, “Tunable and Compact Femtosecond Cr: LiSAF Lasers: Single Prism and Prismless Approaches,” *LEOS Annual Meeting Paper WR3*, 2002.
- [10] B. E. Lemoff and C. P. J. Barty, “Cubic-Phase-Free Dispersion Compensation in Solid-State Ultrashort-Pulse Lasers,” *Optics Letters*, vol. 18, pp. 57-59, 1993.
- [11] A. Yariv, *Optical Electronics*: Saunders College Publishing, 1991.
- [12] K. Naganuma, G. Lenz, and E. P. Ippen, “Variable Bandwidth Birefringent Filter For Tunable Femtosecond Lasers,” *IEEE Journal of Quantum Electronics*, vol. 28, pp. 2142-2150, 1992.

- [13] O. Svelto, *Principles of Lasers*. New York: Plenum, 1998.
- [14] R. Szipocs, A. Kohazi-Kis, S. Lako, P. Apai, A. P. Kovacs, G. DeBell, L. Mott, A. W. Louderback, A. V. Tikhonravov, and M. K. Trubetskoy, “Negative dispersion mirrors for dispersion control in femtosecond lasers: chirped dielectric mirrors and multi-cavity Gires-Tournois interferometers,” *Applied Physics B-Lasers and Optics*, vol. 70, pp. S51-S57, 2000.
- [15] A. Yariv, in *Optical Electronics in Modern Communications*: Oxford University Press, 1997, pp. 17-30.
- [16] S. Lovold, P. F. Moulton, D. K. Killinger, and N. Menyuk, “Frequency tuning characteristics of a Q-switched Co:MgF₂ laser,” *IEEE Journal of Quantum Electronics*, vol. 21, pp. 202-208, 1985.
- [17] G. Holtom and O. Teschke, “Design of a birefringent filter for high power dye-lasers,” *IEEE Journal of Quantum Electronics*, vol. 10, pp. 577-579, 10.
- [18] A. J. Kemp, G. J. Friel, T. K. Lake, R. S. Conroy, and B. D. Sinclair, “Polarization effects, birefringent filtering, and single-frequency operation in lasers containing a birefringent gain crystal,” *IEEE Journal of Quantum Electronics*, vol. 36, pp. 228-235, 2000.
- [19] M. Mazilu, A. Miller, and V. T. Donchev, “Modular method for calculation of transmission and reflection in multilayered structures,” *Applied Optics*, vol. 40, pp. 6670-6676, 2001.
- [20] S. Uemura, “Dispersion compensation for a femtosecond Cr : LiSAF laser,” *Japanese Journal of Applied Physics Part 1-Regular Papers Short Notes & Review Papers*, vol. 37, pp. 133-134, 1998.
- [21] C. Honninger, R. Paschotta, F. Morier-Genoud, M. Moser, and U. Keller, “Q-switching stability limits of continuous-wave passive mode locking,” *Journal of the Optical Society of America B-Optical Physics*, vol. 16, pp. 46-56, 1999.
- [22] I. G. Cormack, W. Sibbett, and D. T. Reid, “Rapid measurement of ultrashort-pulse amplitude and phase from a two-photon absorption sonogram trace,” *Journal of the Optical Society of America B-Optical Physics*, vol. 18, pp. 1377-1382, 2001.

Chapter 4 - High repetition-rate near infra-red femtosecond lasers

4.1 Introduction

Femtosecond lasers have the facility to offer large optical bandwidths that are compatible with a range of applications. For instance, their intrinsically large bandwidths may provide an opportunity to replace the large number of discrete semiconductor laser sources used in wavelength division multiplexing (WDM) with a single laser source. If the repetition-rate of the femtosecond laser can be made high enough, there is the possibility to encode more data using optical time division multiplexing (OTDM) allowing even higher rates of data transmission. The highest repetition rates achieved with a passively modelocked solid-state laser are from a Nd: YVO₄ laser (See, for example, [1]) that produces pulses of several picoseconds duration and narrow bandwidths centred around 1064nm. These lasers have repetition rates of up to 160GHz, at which point the pulses begin to overlap [2]. They have sufficient output power to be used as the pump source for an optical parametric oscillator (OPO) [3] thus facilitating frequency down-conversion to the communications window at 1550nm. However, such configurations tend to be physically large and they lack practicality outside laboratory environments. One possible method of producing the broad optical bandwidths associated with femtosecond pulses is to use semiconductor sources, but such systems presently require relatively complex laser arrangements and external optical components [4] in order to compress the pulse to a minimum in duration.

In this chapter, the construction of high repetition rate Cr: LiSAF and Ti: sapphire lasers is described. The highest repetition rate achieved with a Cr: LiSAF-based laser was just over 1GHz and the highest repetition rate achieved with Ti: sapphire as a gain material was 2.3GHz. The laser designs outlined in this chapter are much less complicated and easier to align than previous examples of high repetition rate Ti: sapphire lasers [5]. In this chapter the issues that must be addressed when constructing a high repetition rate femtosecond laser are discussed in some detail. Particular issues in the design and

construction of an efficient laser are also highlighted as this becomes important when the intracavity pulse energy is reduced. Finally, the results obtained for laser configurations incorporating these two gain media are presented and discussed.

4.2 Avoidance of Q-switched modelocking

Should a laser lapse into Q-switching instabilities rather than stable modelocking then it could prove damaging to the modelocking element and the gain medium. This is because the peak intensity of this train of modelocked pulses underneath a wider Q-switched oscillation in intensity is higher than if the laser was stably modelocked.

Q-switched modelocking (QSML) is an instability arising from a low intracavity pulse energy [6] and the consequent failure of the modelocked optical pulse to fully saturate the absorber. It is caused by a fluctuation in intensity that saturates the absorber but is not fully suppressed by gain saturation. This causes the output of the laser to differ from that of a cw modelocked laser in that modelocked pulses are produced but under a wider Q-switched oscillation in intensity, see figure 4.1.

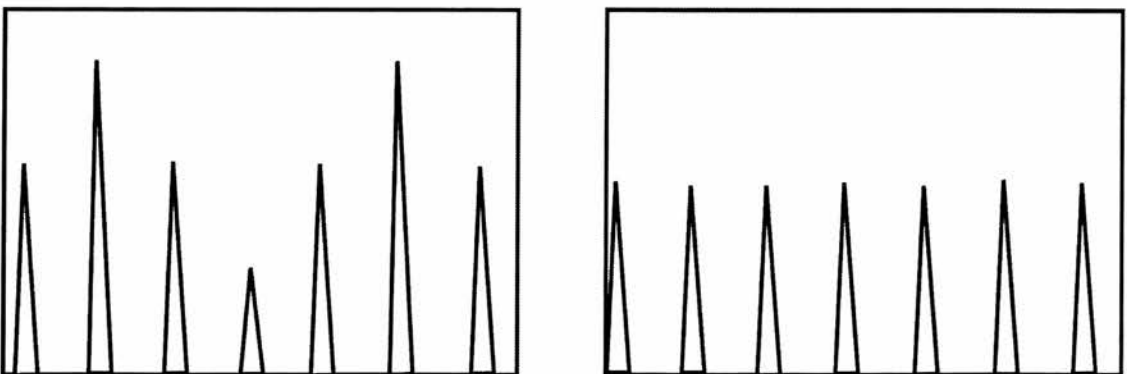


Figure 4.1: Schematic showing the change in the pulse train from Q-switched modelocking (left) to stable CW-modelocking (right)

The work carried out in reference [6] results in a number of experimentally confirmed guidelines for overcoming this problematic instability. These guidelines are summarised in the following equation:

$$E_p > \sqrt{E_{L,Sat} \cdot E_{A,Sat} \cdot \Delta R} \quad (1)$$

Where $E_{L,Sat}$ is the saturation energy of the gain material, $E_{A,Sat}$ is the saturation energy of the absorber, E_p is the pulse energy, and ΔR is modulation depth of the absorber, or the fractional amount of loss associated with the absorber that can be bleached. However the saturation fluence (or energy per unit area) of the gain material is strongly related to the stimulated emission cross-section of the gain material as shown in equation 2:

$$F_{L,Sat} = \frac{h\nu}{2\sigma} \quad (2)$$

The numerator is simply the photon energy of the laser, and σ is the stimulated emission cross-section. Some simple manipulation yields the following. For a given repetition rate, f , fractional output coupling, T , and mode area, A , the required output power that the laser must produce to avoid Q-switching instabilities, in the picosecond regime is given by:

$$P_o > \sqrt{F_{L,Sat} F_{A,Sat} \Delta R} A f T \quad (3)$$

This applies to a simplified case where the mode radius on the absorber and in the gain medium are the same. So for high repetition-rate operation of a SESAM modelocked laser the following properties can be identified as advantageous for stable modelocking,

- Gain medium with large stimulated emission cross-section to lower saturation fluence.
- Efficient, low-threshold parameters, such that a suitable output power can be realised.
- Small mode area on the laser crystal and the saturable absorber.
- Saturation fluence of the SESAM must be suitably low.
- Low intracavity losses together with a small fractional output coupling.

Consideration of the gain material is important. Figure 4.2 shows the output power levels required to overcome QSML for a number of different laser crystals. It is clear that some materials place very high output power demands on a laser system to maintain stable modelocking. In calculating the data for figure 4.2 it has been assumed that the spot size on both the laser crystal and the absorber are the same, and the laser is modelocked at a repetition-rate of 2GHz with a SESAM with saturation fluence of $110 \mu\text{J}/\text{cm}^2$, which is the saturation fluence of the SESAM used in the lasers described in section 4.4.

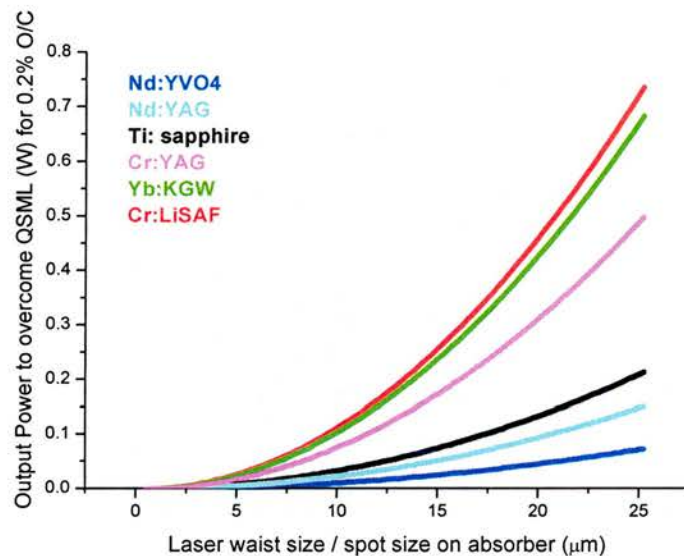


Figure 4.2: Output power needed to overcome QSML versus waist size for a selection of laser crystals.

The above is for the picosecond case. In the case of pulse durations in the several tens of femtoseconds regime this condition can be relaxed. Honniger et al [6] explain this in the following way for the case where dispersion compensation is in place: When the energy of the pulse is increased (perhaps due to relaxation oscillations) the magnitude of self phase modulation will increase and because of the finite gain bandwidth this will reduce the effective gain seen by the pulse. This effect provides some negative feedback that will decrease the critical pulse energy required for stable cw modelocking. Thus, the following relationship has been derived for the pulse energy to ensure stable operation:

$$E_{L,Sat} \cdot g \cdot K^2 \cdot E_p^3 + E_p^2 > E_{L,Sat} \cdot E_{A,Sat} \cdot \Delta R \quad (4)$$

Here g is the round-trip gain and K is the ratio of the change in pulse bandwidth with pulse energy to the gain bandwidth. These authors showed that this K factor can be approximated by:

$$K = \frac{4\pi n_2 L_K}{D_2 A \lambda \Delta v_g} \cdot \frac{0.315}{1.76} \quad (5)$$

and that the round-trip saturated gain, g , is given by,

$$g = \Delta R \cdot \frac{E_{A,Sat}}{E_p} \cdot (1 - e^{-\frac{E_p}{E_{A,Sat}}}) + loss \quad (6)$$

The first term on the right hand side of this equation corresponds to the loss that is introduced into the cavity from the insertion of the absorber and the second term is the parasitic loss associated with the mirrors, absorption of laser light in the crystal, etc. In equations 5 and 6, n_2 is the nonlinear refractive index, L_K is the propagation distance in the gain medium, D_2 is the magnitude of the negative group delay dispersion (GDD) required to balance self-phase modulation (SPM) as calculated through the soliton equation [7], and Δv_g is the FWHM of the fluorescence spectrum. However, this slight reduction only becomes important with sub-50fs pulses. This can be seen from figure 4.3, where the critical pulse energy to achieve stable cw modelocked operation in both the picosecond (i.e. equation 3) case and the femtosecond (i.e. equation 4) case are shown.

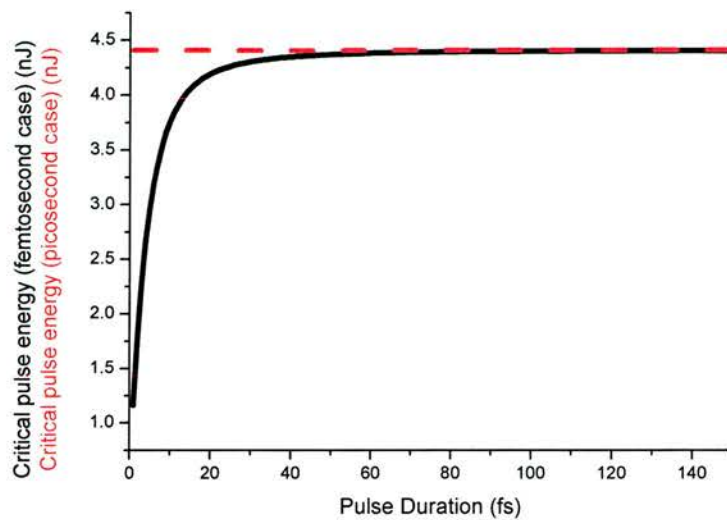


Figure 4.3: Critical pulse energy in the femtosecond case compared to the picosecond case where pulse shaping due to a broad optical bandwidth is neglected. This is for a 2GHz prf Ti: sapphire laser with absorber saturation fluence of $110 \mu\text{J}/\text{cm}^2$ and a spot size of $25 \mu\text{m}$ on both the laser crystal and on the absorber

In this section it has been shown that the drop in required pulse energy deduced from the expressions relating to a broad bandwidth pulse in a femtosecond laser is only important when the pulse has duration in the several tens of femtoseconds regime. It also dealt with the selection of the gain media for a high repetition-rate femtosecond laser. In the next section the key parameters for the construction of an efficient femtosecond laser are further elaborated.

4.3 Construction of an efficient laser

With the constraints put on the gain material discussed in section 4.2 it is clearly important to construct an efficient optical resonator around it. In addition to using high specification optical components, for example high quality laser crystals, mirrors with very high reflectivity at the laser wavelength, and so on, there are a number of cavity designs that can be implemented to ensure low threshold and efficient operation. In this section some of these details will be introduced and an explanation given as to why these determine the principal aspects of the laser design. Most of the work in this section follows on from the work by A.J. Alfrey [8].

One of the main factors determining the laser performance of a Ti: sapphire oscillator is the figure of merit (FOM) of the laser crystal itself. This number, typically several hundred in magnitude, is defined as,

$$FOM = \frac{\alpha_{\text{pump}}}{\alpha_{\text{laser}}} \quad (6)$$

Where α_{pump} is the absorption coefficient at the pump wavelength and α_{laser} is the absorption coefficient at the laser wavelength. When purchasing Ti: sapphire laser rods it is important to ensure this number is as high as possible to ensure maximisation of the pump absorption and minimisation of the laser light absorption and scatter.

Starting from the collinear propagation of gaussian modes and the rate equations, a model describing the laser can be built up in terms the pump and laser modes, [8] assuming that they propagate according to the equations,

$$\omega(z)_c^2 = \omega_{co}^2 \left(1 + \frac{(z - z_1)^2 \lambda_c^2}{\pi^2 \omega_{co}^4 n_c^2} \right) \quad (7)$$

for the laser mode. For the pump mode,

$$\omega(z)_p^2 = \omega_{po}^2 \left(1 + \frac{(z - z_1)^2 \lambda_p^2}{\pi^2 \omega_{po}^4 n_p^2} \right) \quad (8)$$

Here $\omega(z)_p$ is the beam radius for the pump mode and similarly $w(z)_c$ is the beam radius for the laser mode, λ_p and λ_c are the pump and laser wavelengths respectively, n_p and n_c are the refractive indices of the gain medium at the pump and laser wavelengths, z is the displacement, z_1 and z_2 are the positions of the pump and laser waists respectively, and ω_{po} and ω_{co} are the waist radii of the pump and laser mode respectively. If one were to plot the waist size against displacement over several lengths of the crystal then it would look similar to figure 4.4.

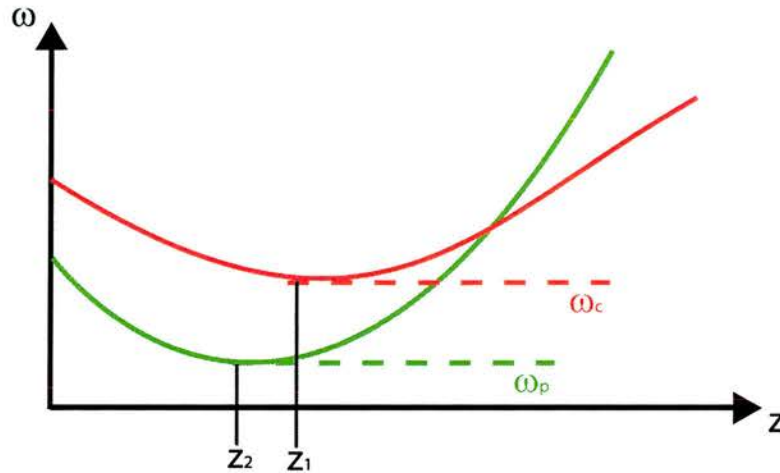


Figure 4.4: Plotting the waist size (ω) against propagation distance (z) for a collinear pump and laser modes in a laser crystal.

From this, and the balance of gain and loss in a laser cavity, an expression for the pump power required to achieve a particular intracavity power can be derived [8] which accounts for the Gaussian beam profile of the modes and for diffraction,

$$P_p = \frac{(T + \Lambda).h.c.\pi^2}{8.\sigma.\tau.\lambda_p.\alpha_p \int_0^L \frac{e^{-\alpha_p z}}{\omega_c^2(z).\omega_p^2(z)}.Q(z).dz} \quad (9)$$

Here z is the distance through the crystal, T is the output coupling used, Λ is the total parasitic loss in the cavity in a round trip, α_p is the pump absorption coefficient, σ and τ are the stimulated emission cross section and the upper-state lifetime respectively, and the spot sizes are determined by (8) and (7). $Q(z)$ is given by,

$$Q(z) = 2.\pi.\int_0^\infty \frac{e^{-Az^2}}{1 + Be^{-Dr^2}} \quad (10)$$

Where,

$$A = \frac{2(\omega_p(z)^2 + \omega_c(z)^2)}{\omega_p(z)^2 \cdot \omega_c(z)^2}, B = \frac{4.P_c}{\pi \cdot \omega_c(z)^2 \cdot I_s}, \text{ And } D = \frac{2}{\omega_c(z)} \quad (11)$$

Around threshold the intracavity intensity is very much smaller than the saturation intensity ($I_s \gg I_c$) so Alfrey [8] shows that the expression for threshold pump power can be simplified to,

$$P_{TH} = \frac{(T + \Lambda) \cdot h.c.\pi^2}{4 \cdot \sigma \cdot \tau \cdot \lambda_p \cdot \alpha_p \int \frac{e^{-\alpha_p \cdot z}}{\omega_c(z)^2 + \omega_p(z)^2} dz} \quad (12)$$

From 12, it can be seen that the stimulated emission \times upper state lifetime product ($\sigma\tau$) is crucial in minimising the threshold of a laser, as is the maximisation of the pump absorption (α_p). However maximisation of the pump absorption, through the use of a highly doped crystal, may also mean an increase in the parasitic losses due to scattering losses or laser light absorption. These parameters must obviously be minimised to ensure a low threshold and efficient operation. This chapter is concerned with Cr: LiSAF and Ti: sapphire gain media which have stimulated emission cross section \times upper state lifetime products of $32.2 \times 10^{-19} \text{ cm}^2 \mu\text{s}$ and $12.2 \times 10^{-19} \text{ cm}^2 \mu\text{s}$ respectively [9]. From (12), a lower threshold may therefore be expected from a Cr: LiSAF laser than from a laser based on Ti: sapphire. It is also the case that the pump absorption coefficient is higher in Cr: LiSAF than in a Ti: sapphire crystal.

The model presented by Alfrey [8] provides an interesting tool when investigating the parameter space available with a Ti: sapphire laser. Figure 4.5 shows the expected output power for 500mW of incident pump power for a Ti: sapphire laser. It shows a local maximum around 2.5mm crystal length for a spot size of 25μm.

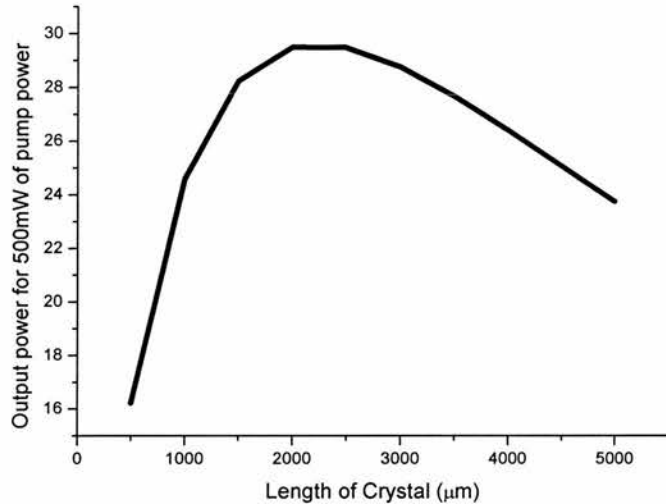


Figure 4.5: Expected output power for 500mW of absorbed pump power for a CW Ti: sapphire laser with $\alpha_p=4\text{cm}^{-1}$ and FOM=260. Both the pump and laser modes are focussed just inside the front face of the crystal and have a waist size of $2.5\mu\text{m}$.

Alfrey's model [8] and the equations which govern stable semiconductor mirror-based modelocking can be combined in order to get a feel for the pump requirements imposed when trying to modelock a Ti: sapphire laser at high repetition rates. In figure 4.6 the calculated pump power both to reach threshold and to overcome Q-switching instabilities have been plotted. This shows that the pump power requirements are not too restrictive and the laser will not have to be pumped too far above threshold to overcome Q-switching instabilities.

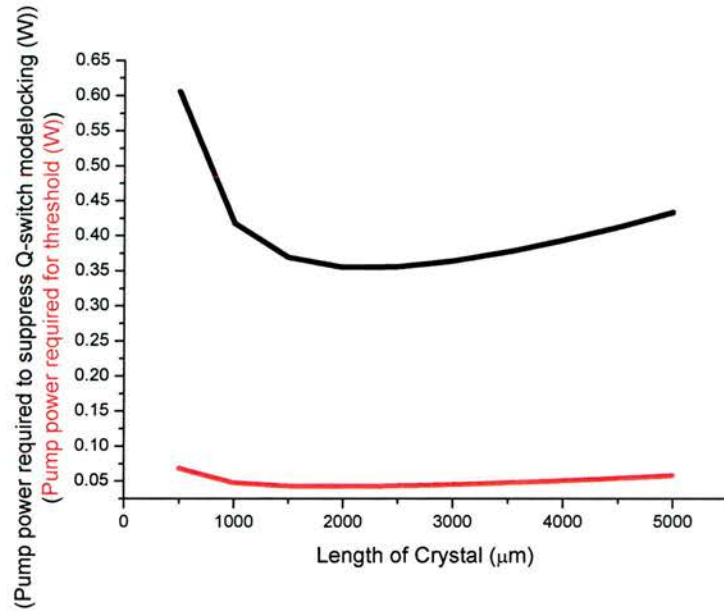


Figure 4.6: Pump power required for a 2GHz Ti: sapphire laser to reach threshold and to overcome Q-switching instabilities.

For the graphs plotted in figures 4.1 to 4.6 good mode matching of the pump and laser modes has been assumed and the beam waist of the pump and laser modes is around 25 μm , to ensure efficient operation. A very high degree of spatial quality of the pump light ($M^2 = 1$) has also been assumed. It can be seen for this particular crystal, $\text{FOM}=260$ and $\alpha_p=4\text{cm}^{-1}$, that the threshold pump power and threshold for overcoming Q-switching instabilities reach a local minimum for a crystal length of 2.5mm. This coincides with the maximum in output power for 500mW of incident pump power shown in figure 4.5.

This section has demonstrated that only with careful design and selection of the intracavity components can the repetition-rate of a femtosecond laser be increased to the multi-GHz level. The next sections detail the experimental realisation of high-repetition rate lasers developed around the Ti: sapphire and Cr: LiSAF materials.

4.4 1GHz repetition-rate Cr: LiSAF laser

The combination of the dispersion-compensating high reflectors (referred to as the QTF mirrors in the previous chapter), combined with the relatively low saturation fluence of the SESAM ($110 \mu\text{m}/\text{cm}^2$) meant that the regular ‘z-cavity’ configuration could be reduced in physical size with relative ease. Figure 4.7 and Table 4.1 show the cavity configuration that facilitated this high repetition-rate [10].

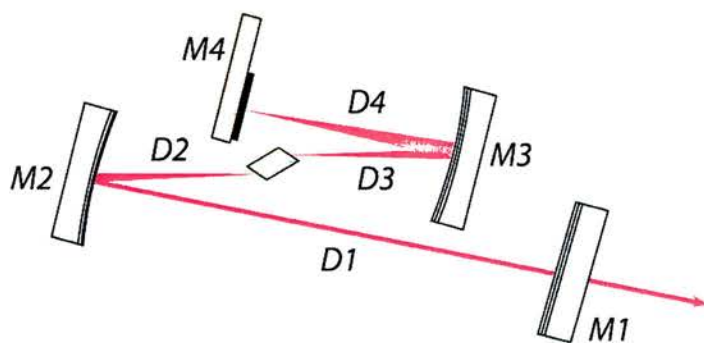


Figure 4.7: Cavity dimensions for the 1GHz Cr: LiSAF laser

Cavity Dimension	Value
D1	50mm
D2	15mm
D3	27mm
D4	31mm
Angle between D1 and D2	Very small
Angle between D3 and D4	14 degrees
M4	SESAM
M1, M2, M3	HR mirror (transmission <0.1%) RoC M2 = 30mm

Table 4.1: Cavity details for 1GHz Cr: LiSAF laser

This cavity provided a laser spot radius of around 30 μm on the SESAM, a repetition rate of 1GHz and an output power of 3mW, corresponding to a fluence of 150 $\mu\text{J}/\text{cm}^2$ on the SESAM. At this low fluence the laser had a tendency to lapse into Q-switching instabilities, but because the spot size was kept large there was little chance of damage to the SESAM from the higher intensities. In laser systems where the pulse energy is not quite so low (in this case 3pJ) the ‘rule of thumb’ to secure stable modelocking is to maintain a fluence on the SESAM which is 4-5 times its saturation fluence.

The pump source for this laser was four AlGaInP laser diodes, two diodes operating at 660nm and two diodes operating at 685nm. Each 660nm diode was wavelength coupled to a 685nm diode using a dichroic mirror. The two pairs of wavelength coupled diodes were then polarisation coupled in a polarising cube to give \sim 180mW of total pump power. The pump laser light was focussed onto the Cr: LiSAF crystal using a 37mm focal length lens to give a pump spot radius of 11 μm just inside the front face of the laser crystal.

The laser was modelocked at a repetition-rate of just over 1GHz and pulse durations of 146fs were deduced from autocorrelation measurements. The output power was only 3mW, due to the very low output coupling, for around 180mW of incident diode pump power. This meant that the autocorrelator used to determine the pulse duration had to be extremely sensitive. This sensitivity was achieved by using a x40 aspheric lens to focus tightly onto a GaAsP photodiode. The characteristics of the laser are shown in figure 4.8.

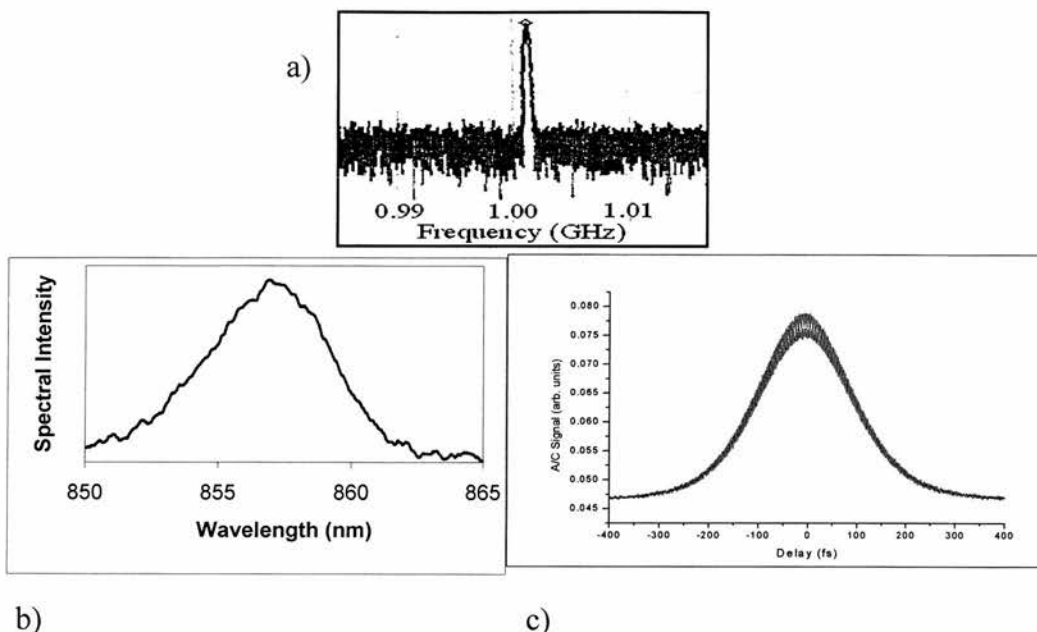


Figure 4.8: RF Spectrum (a), spectrum, (b), and autocorrelation, (c) indicating 146fs pulses from the 1GHz Cr: LiSAF laser.

The results achieved here are very encouraging for the design of lasers that have low pulse energies. The move from this low stimulated emission cross-section material to a material that has a significantly higher cross-section should allow even higher repetition-rates in the same spectral region. Ti: sapphire is an obvious contender in this regard and therefore high repetition rate lasers using this as a gain material are the subject of the next section.

4.5 High repetition-rate Ti: sapphire Lasers

4.5.1 Initial investigations of Ti: sapphire Lasers: 500 MHz repetition-rate

On the basis of the encouraging nature of the results achieved with the Cr: LiSAF laser, the decision was made to examine high repetition-rate sources based around a 2.5mm long Ti: sapphire crystal (0.25% doped and FOM >260). This crystal length was selected because the modelling discussed earlier predicts a local minimum in threshold with this crystal length. In addition, it reduces the requirement on intracavity dispersion compensation. Anti-reflection (AR)

coated plane/plane crystals were used in order to keep the number of restrictions on cavity configurations to a minimum. A cavity with a repetition-rate of around 500MHz was constructed in order to assess the quality of both the mirror set and the crystals purchased. [See figure 4.8 and table 4.2 for the cavity dimensions.]

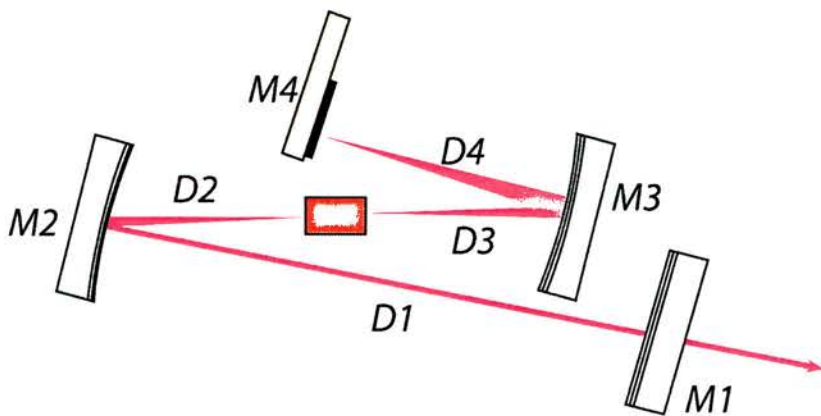


Figure 4.8: Schematic of the Ti: sapphire lasers as constructed

Cavity Dimension	Value
D1	100mm
D2	25mm
D3	68mm
D4	40mm
Angle between D1 and D2	2 degrees
Angle between D3 and D4	2 degrees
M4	SBR/HR mirror
M1, M2, M3	HR mirror (transmission <0.1%) RoC M2=M3= 50mm

Table 4.2: Cavity dimensions for the 500MHz Ti: sapphire laser

The ABCD matrix-modelling program “LCAV” was then used to calculate the spot radius in both the tangential and sagittal planes and ensure that the focussed arm would provide sufficient intensity on an intracavity modelocking element. The results of this calculation can be seen in figure 4.9.

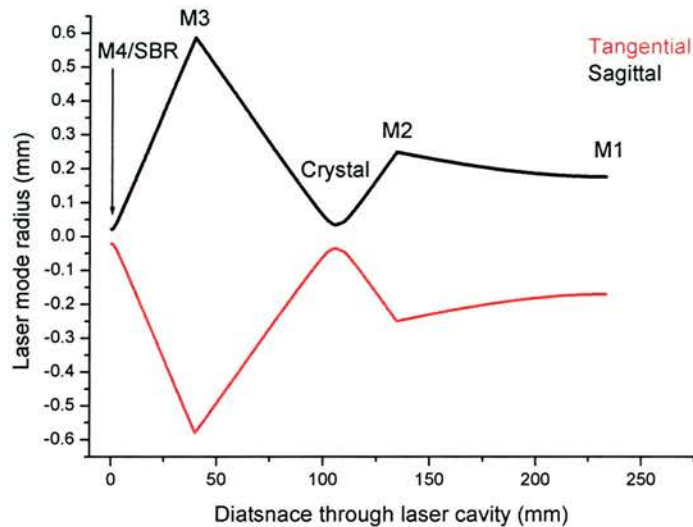


Figure 4.9: The laser spot radius through the cavity in the tangential and sagittal planes

This cavity design provided a spot radius of $25\mu\text{m}$ at the end of the focussed arm (M4). It also provided a focus of $40\mu\text{m}$ on the front face of the crystal. The former spot size was predicted to provide sufficient intensity to fully saturate the low temperature grown SESAM used in the Cr: LiSAF laser demonstrated in section 4.4. However, it should be noted, the absorber used here and in all Ti: sapphire based lasers discussed in future sections was a narrowband SBR from the Institute of Photonics at the University of Strathclyde with a designed centre wavelength of 835nm and it was expected that the saturation fluence of the SBR would be of the same order of magnitude.

The pump source used in these experiments was a Spectra-Physics Millennia Xs that produced up to 10W of pump power at 532nm. This pump source had an $M^2 \sim 1$ and the beam radius before the focussing lens was 1mm. Focussing of the pump light into this cavity was provided by a 125mm lens that provided a pump spot of $35\mu\text{m}$ near the front face of the crystal, so as to match the position of the laser mode focus. The cavity was constructed and the input power vs. output

power characteristic measured for a number of output couplings. This is illustrated in figure 4.10.

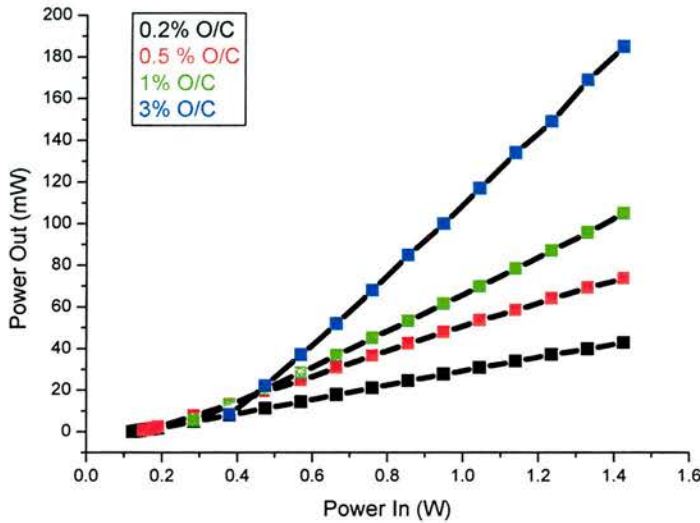


Figure 4.10: Power out as a function of incident power for various output couplings

These results allowed an estimation of the round-trip loss to be calculated through a Findlay and Clay loss analysis [11]. These authors show that the reflectivity and threshold pump power are related to one another through the relation,

$$-\ln R = 2KP_{th} - L \quad (13)$$

where R is the fractional reflectivity of the output coupling, K is a constant, P_{th} is the threshold pump power with each output coupler in place and L is the round-trip loss. From this equation it can be seen that, if the natural logarithm of the reflectivity of the output coupling is plotted as a function of the threshold pump power, the y-axis intercept will be the round-trip loss associated with the cavity. The data plotted in figure 4.11 allow this loss analysis to be carried out. From the intercept of the graph plotted in figure 4.11 it can be seen that this cavity has an associated round-trip loss of 1.5%. This would seem relatively high, in the context of a low threshold system, and this was attributed to the limited quality of the AR coatings on the crystal. Therefore an investigation into

the reflectivity of these crystal coatings was then carried out. At an incident angle of 3 degrees the coating reflected around 0.2% of the power from an incident 850nm laser beam and at an angle < 1 degree, it was found to reflect around 0.06%. This crude measurement illustrated the importance of crystal orientation in minimising the reflected laser light. To minimise this reflection, the pump and laser beam must meet the crystal as close to zero incidence as possible. This could be remedied in this cavity, but in systems with higher repetition-rates the close proximity of the opto-mechanical mounts made such adjustments very difficult to implement.

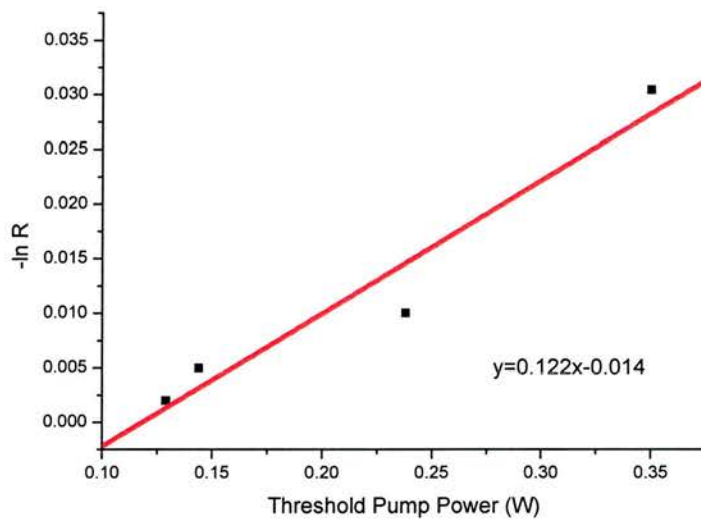


Figure 4.11: Natural logarithm of reflectivity of output coupling as a function of the threshold pump power used in the Findlay and Clay loss analysis[11]. Also shown is a best-fit straight line.

Out of interest, the power characteristic for the 0.2% output coupler was replotted alongside the Alfrey [8] prediction for this cavity with a loss per round-trip of around 1.5%. This should indicate the validity of this Findlay and Clay analysis [11]. As is immediately evident from figure 4.12, the method seems to give an extremely good correlation between the experimentally obtained data

and the combination of the Alfrey model and Findlay and Clay loss analysis, in this case.

The output spectrum of this laser was also recorded to determine whether any wavelength tuning would be required to force the laser onto the resonance of the SBR. This output spectrum is shown in figure 4.13, and shows that the free-running spectrum of this laser did not have to be altered as it oscillates with a centre wavelength of 835nm which coincides favourably with the SBR response.

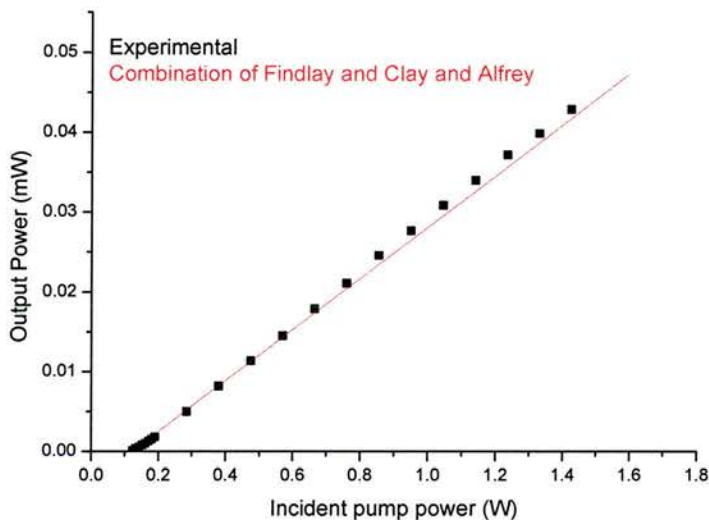


Figure 4.12: The experimentally obtained power characteristic shown alongside the Alfrey prediction with the calculated round-trip loss.

The SBR was then inserted as one of the end mirrors (M4 in figure 4.8) of the cavity in the focussed arm of the laser. This had very little effect on the power characteristic and this is an indication that the SBR was at least as good a reflector as the dielectric mirror that was previously in place. To investigate the response of the SBR, a single fused silica prism was inserted into the long, collimated arm. Such a prism leaves the beam angularly dispersed (see section 3.2) and so the oscillating wavelength can be altered by tilting the output coupler. The results of this are shown in figure 4.13 and illustrate that as the laser is tuned to 830nm the output is spectrally broadened. This is what might be expected from an SBR with a narrow spectral response because a change in the oscillating wavelength by only a few nanometres results in no spectral broadening. It should be noted that the laser did not modelock with this prism

material in place. This was due to the fact that the Ti: sapphire crystal contributes a significant amount of positive dispersion to the cavity ($\sim 275\text{fs}^2$) and this single prism arrangement provided insufficient dispersion compensation.

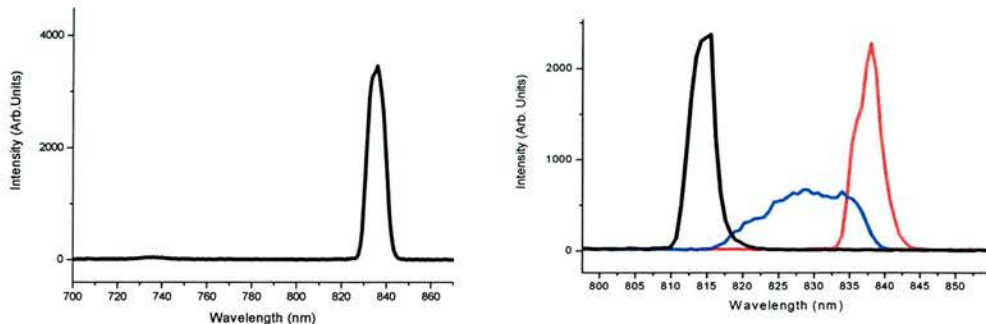


Figure 4.13: The free running output spectrum with HR mirror in place (left) and the tunability with the SBR and fused silica prism in place (right). Coloured lines in right hand plot show the change in output spectrum as the output coupler is tilted and the laser is tuned.

It then became immediately obvious from the proximity of the optical components that some integrated source of negative dispersion would be required for this laser to enable it to be modelocked. The minimum prism separation for a prism pair would increase the length of the cavity, and lower the repetition rate to such an extent that it would be detrimental to the project objectives. This meant that for the project to proceed, a form of mirror-based dispersion compensation had to be designed.

4.5.2 ~1GHz Ti: sapphire Laser

The conclusion drawn from the previous section is that for the project objectives to be realised using a gain medium as dispersive as a Ti: sapphire crystal a mirror-based dispersion compensation scheme would have to be implemented. [The methods and final design for this are the subject of the second half of chapter 2. A set of Gires-Tournois interferometer (GTI) mirrors were designed. This design was then sent to an optical coating company for manufacture.]

A cavity was designed using the ‘LCAV’ program that would operate with a repetition rate of around 1GHz (see figure 4.14 and table 4.3) and an initial cw characterisation carried out. When the GTI mirrors were supplied they replaced the mirror set used in the results reported in section 4.5.1. This led to a cavity design for a laser operating in the cw regime that allowed for a direct comparison to be made between the two mirror sets.

For a given output power, the pulse energy in the cavity halves as the repetition-rate of the laser is doubled. This implies that the output coupling on this laser has to be kept relatively low so as to maximise the pulse energy and to saturate the SBR.

Cavity Dimension	Value
D1	50mm
D2	12mm
D3	30mm
D4	22mm
Angle between D1 and D2	4 degrees
Angle between D3 and D4	Small
M4	SBR/HR mirror
M2, M3	GTI-HR mirror (transmission <0.1%) RoC M2=M3=25mm
M1	0.2% output coupler

Table 4.3: Cavity configuration for the ~1GHz Ti: sapphire laser, see figure 4.8

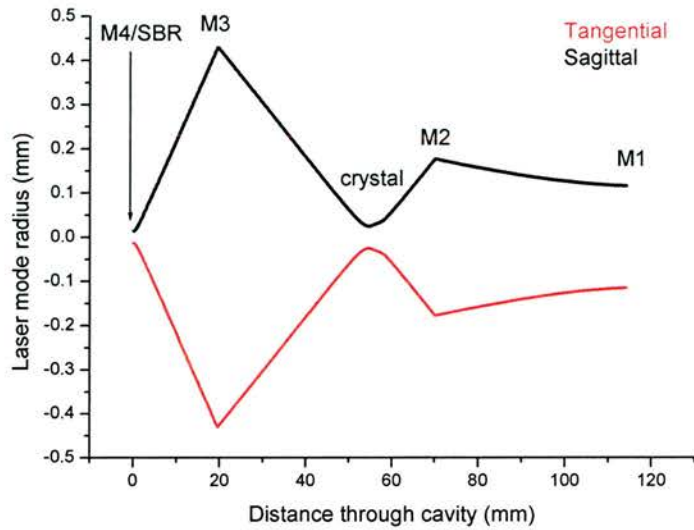


Figure 4.14: Change in spot size through the cavity for the \sim 1GHz Ti: sapphire laser, calculated by the LCAV program.

The cavity illustrated in figure 4.14 provides a spot radius on the SBR of $18\mu\text{m}$ and laser mode spot radius of $27\mu\text{m}$ just inside the front face of the laser crystal. With a 0.2% output coupler in place (M1), the power characteristic, shown in figure 4.15, was obtained. Also shown in this plot is exactly the same cavity configuration with the dispersive mirrors designed in chapter 2 in the place of the standard dichroic mirrors. This plot shows that the reflectivity of these mirrors at the laser wavelength is slightly better than the non-dispersive mirror set, thereby giving a higher slope efficiency and a lower threshold.

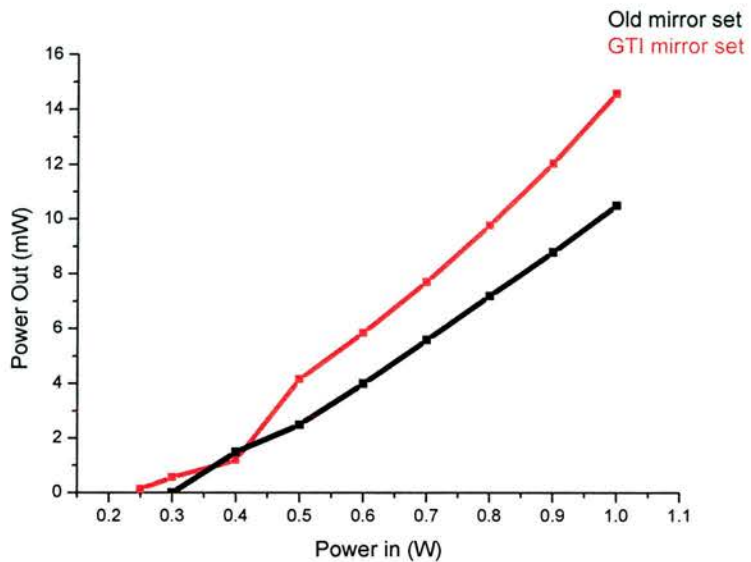


Figure 4.15: Power characteristic for the ~1GHz laser with the mirror set used in 4.5.1. and the new GTI mirrors designed in chapter 2, using a 0.2% output coupler.

The SBR was then inserted into the focussed arm of the laser, and again, this had very little effect on the output power produced by the laser. The laser could be modelocked readily with only a minimal amount of adjustment of the position and angle of the SBR. The repetition rate of the laser was measured using a fast photodiode and no evidence of Q-switching instabilities could be seen in either the RF spectrum, measured with an RF spectrum analyser and fast photodiode, or the pulse train measured on a fast oscilloscope. The spectral and autocorrelation profiles are shown in figure 4.16. The measured repetition rate was ~985MHz. The pulse duration was ~180fs and the laser oscillated on a bandwidth of around 11nm. These measurements imply a duration-bandwidth product of approximately 0.8. [The highly frequency-chirped nature of these pulses will be discussed in the conclusions section of this chapter]

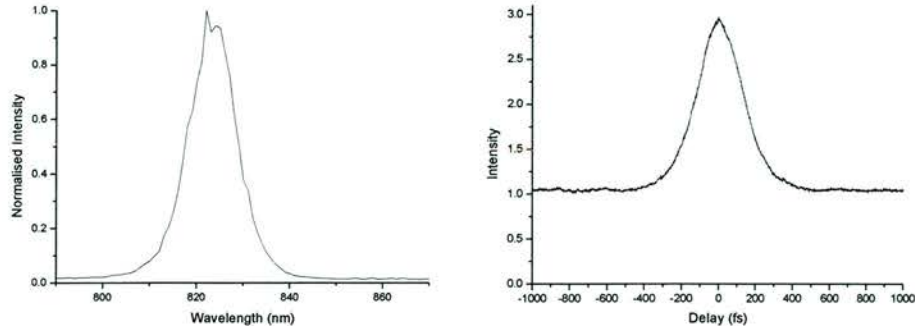


Figure 4.16: The spectrum (left) and autocorrelation (right) of the ~1GHz Ti: sapphire laser

The input pump power was then gradually reduced in order to investigate the threshold for modelocking. The output power as a function of input power is shown in figure 4.17.

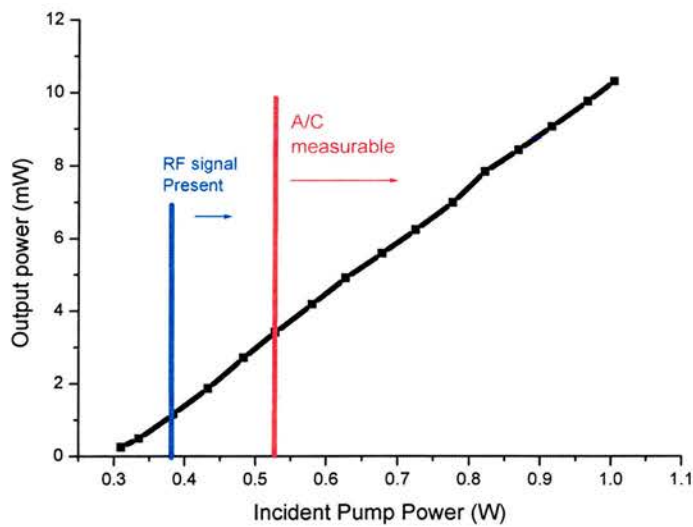


Figure 4.17: Power out as a function of power in for the ~1GHz Ti: sapphire laser

Some interesting points are also noted on this graph. For instance, a measurable autocorrelation was still recordable with 3.5mW output power, which corresponds to 530mW incident pump power. The RF spike, on the spectrum analyser, corresponding to the round-trip frequency was evident with only 1.2mW output power, which corresponds to only 380mW of incident pump power. These results make the possibility of pumping the Ti: sapphire laser with

a pump laser considerably smaller than the Millennia Xs used a viable option. In addition, for a pump laser which is commensurate in size with the laser resonator itself, the move to a mini-laser pump source would also considerably reduce the cost of the overall system and remove the need for closed loop water cooling.

4.5.3 > 2GHz Ti: sapphire laser

The folding mirrors in the cavity were then replaced with mirrors of a smaller radius of curvature. This reduced the cavity footprint without increasing its level of complexity. A cavity was designed using the LCAV modelling program that used 15mm and 20mm radius of curvature folding mirrors. The change in spot size throughout the cavity is shown in figure 4.18

Cavity Dimension	Value
D1	25mm
D2	8mm
D3	20mm
D4	7mm
Angle between D1 and D2	4 degrees
Angle between D3 and D4	Small
M4	SBR
M2, M3	GTI HR mirror (transmission <0.1%) M2=15mm, M3=10mm
M1	HR mirror

Table 4.4: Cavity dimensions for the 2.3GHz Ti: sapphire laser, see figure 4.8

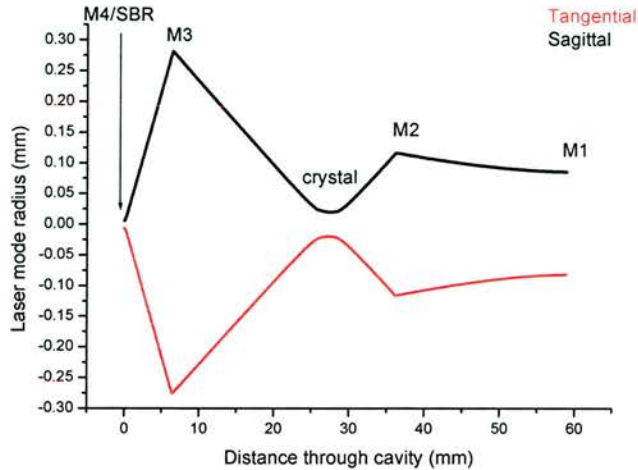


Figure 4.18: Spot Radius as a function of distance through cavity for the 2.3GHz Ti:sapphire laser

Due to the close proximity of the optical elements in this cavity, the laser was not operated cw and the initial setting up and optimisation was carried out with the SBR in the focussed arm. The laser was not expected to modelock readily with the relatively high output couplings used in the laser described in section 4.5.1 due to the lower pulse energy. For this reason a nominally HR mirror was used as an output coupler ($T < 0.1\%$). An autocorrelation measurement was made and a representative profile is included in figure 4.19 together with the output spectrum of the laser.

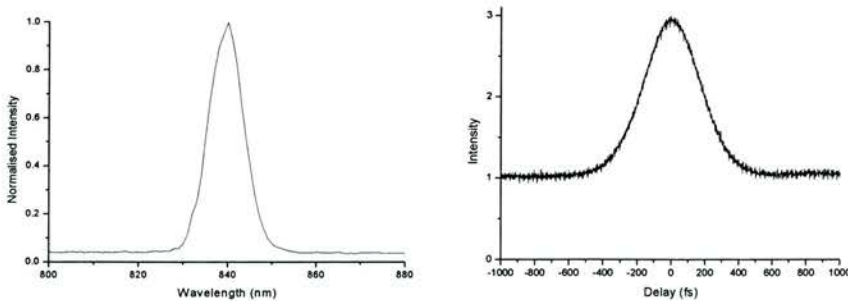


Figure 4.19: Spectral (left) and autocorrelation (right) profiles for the 2.3GHz laser

The repetition rate was measured using a fast photodiode connected to an RF spectrum analyser. Again, there was no evidence of Q-switching instabilities. This laser produced up to 10mW of output power for 1W of incident pump

power. It should be noted that the 10mW of output power for 1W of incident pump power could only be generated operating on the edge of the output coupling mirror where the reflectivity of the mirror coating is somewhat lower than in the centre. As the incident pump power was reduced the RF spectrum analyser indicated modelocked output for incident pump powers of \sim 400mW. This, again, would allow future work to be carried out using a smaller pump source.

4.6 Conclusions

In this chapter the modelling and construction of high-repetition rate Ti: sapphire lasers has been discussed, and some of the implications of low pulse energy modelocked lasers, particularly Q-switching instabilities have been highlighted. The design and performance of a 1GHz pulse-repetition-rate Cr: LiSAF laser that produces near transform-limited 146fs pulses has been included. This, to the author's knowledge is the highest repetition-rate from diode-pumped bulk femtosecond laser modelocked using a semiconductor-based mirror. Modelocked lasers based on Ti: sapphire which operated at \sim 1GHz and 2.3GHz and producing 180fs and 240fs respectively were demonstrated. It was observed that the pulses from these two lasers were significantly frequency-chirped. This could have arisen from a discrepancy between the centre wavelength of the saturable absorption and the dispersion of the mirrors. This would have meant the pulse would not have experienced enough negative dispersion to ensure it was transform-limited. It is also possible that the tight foci used in these lasers would increase the lasers' susceptibility to Kerr-lens modelocking (KLM) with the SBR only then providing the starting mechanism for modelocking. However, evidence of this was not seen in the tolerance of the alignment. However, the lasing bandwidth of these two lasers suggested that extra-cavity dispersion compensation could provide pulse durations as short as 65fs. Both of these lasers were based on 4-element cavities and relied on a custom designed, highly-integrated form of dispersion compensation. Demonstration of modelocked femtosecond lasers with repetition-rates as high as those demonstrated in this chapter provides the performance and robustness required to open up new application areas.

References

- [1] L. Krainer, R. Paschotta, M. Moser, and U. Keller, "77 GHz soliton modelocked Nd : YVO₄ laser," *Electronics Letters*, vol. 36, pp. 1846-1848, 2000.
- [2] L. Krainer, R. Paschotta, S. Lecomte, M. Moser, K. J. Weingarten, and U. Keller, "Compact Nd : YVO₄ lasers with pulse repetition rates up to 160 GHz," *IEEE Journal of Quantum Electronics*, vol. 38, pp. 1331-1338, 2002.
- [3] S. Lecomte, L. Krainer, R. Paschotta, M. J. P. Dymott, K. J. Weingarten, and U. Keller, "Optical parametric oscillator with a 10-GHz repetition rate and 100-mW average output power in the spectral region near 1.5 μm," *Optics Letters*, vol. 27, pp. 1714-1716, 2002.
- [4] I. Y. Khrushchev, I. H. White, and R. V. Penty, "High-quality laser diode pulse compression in dispersion- imbalanced loop mirror," *Electronics Letters*, vol. 34, pp. 1009-1010, 1998.
- [5] A. Bartels, T. Dekorsy, and H. Kurz, "Femtosecond Ti : sapphire ring laser with a 2-GHz repetition rate and its application in time-resolved spectroscopy," *Optics Letters*, vol. 24, pp. 996-998, 1999.
- [6] C. Honninger, R. Paschotta, F. Morier-Genoud, M. Moser, and U. Keller, "Q-switching stability limits of continuous-wave passive mode locking," *Journal of the Optical Society of America B-Optical Physics*, vol. 16, pp. 46-56, 1999.
- [7] Optical Society of America , *Handbook of Optics* vol. IV, McGraw Hill Professional
- [8] A. J. Alfrey, "Modeling of Longitudinally Pumped Cw Ti - Sapphire Laser-Oscillators," *IEEE Journal of Quantum Electronics*, vol. 25, pp. 760-766, 1989.
- [9] J.-M. Hopkins, "Compact, Low Threshold Femtosecond Lasers," (PhD Thesis) in *Physics and Astronomy*. St. Andrews, 1999.
- [10] A. J. Kemp, B. Stormont, B. Agate, C. T. A. Brown, U. Keller, and W. Sibbett, "Gigahertz repetition-rate from directly diode-pumped femtosecond Cr : LiSAF laser," *Electronics Letters*, vol. 37, pp. 1457-1458, 2001.
- [11] W. Koechner, *Solid State Laser Engineering*. New York: Springer-Verlag, 1999.

Chapter 5 - Low-threshold Ti: sapphire lasers

5.1 Introduction

Although the product of stimulated emission cross-section and upper-state lifetime is lower in the case of Ti: sapphire than in both Cr: LiSAF (see Chapter 4) and some Yb-doped materials [1], it is a more well-established gain medium and is used in many commercial ultrafast oscillator systems. Furthermore, the broad emission bandwidth associated with Ti: sapphire is capable of supporting sub-10fs pulses [2]. If the incident pump power requirements can be reduced for Ti: sapphire lasers then a cheaper pump source may be used that combines the benefits of better system integrability as well as lower costs of purchase and operation. This will open up applications to Ti: sapphire lasers where the cost of the pump laser has often hindered the full extent of their use. In this chapter the design criteria for a low-threshold cw Ti: sapphire laser are established and a low-threshold femtosecond Ti: sapphire laser incorporating a SESAM is described.

A conceptually similar approach has been applied to the design of a Kerr-lens modelocked (KLM) Ti: sapphire laser [3]. This laser had a pulse repetition rate of 30MHz, which implies a cavity length of 5 metres. This low repetition rate is required to keep the pulse intensity high enough to exploit the optical Kerr effect, but it does mean that this laser suffers from the inherent disadvantage that any decrease in pump power requirements will be met with an increase in the cavity length associated with the laser. Additionally, modelocked lasers based around KLM alone are not usually as operationally robust as their SESAM modelocked counterparts.

In this chapter the implementation of a low-threshold Ti: sapphire laser in both the cw and modelocked regimes is described. It also includes results obtained from a cw Ti: sapphire laser pumped with a compact and relatively inexpensive 300mW green laser. The key design factors that are discussed in this chapter are the trade-off between dopant concentration and crystal length, the optimisation of the pump focussing geometry and the delivery of sufficient fluence to the saturable absorber to initiate modelocking at modest power levels. All of these

design factors are studied in detail using the Alfrey model [4] discussed fully in section 4.3.

5.2 Modelling and optimisation of low-threshold Ti: Sapphire lasers

When selecting Ti: sapphire crystals for laser operation there are two main options to be considered. The first is to use a crystal with high figure of merit (FOM) and low dopant concentration (e.g. FOM in excess of 260, and 0.15% dopant concentration) or lower FOM and higher dopant concentration (e.g. FOM in excess of 150 and 0.25% dopant concentration). Figure 5.1 shows a direct comparison of two such crystals in the same cavity configuration and the difference in threshold pump power between the two as a function of crystal length. For the modelling described in this section the pump source has an $M^2 \sim 1$ and the pump and laser mode have radii of 25 μm focussed just inside the front face of the crystal.

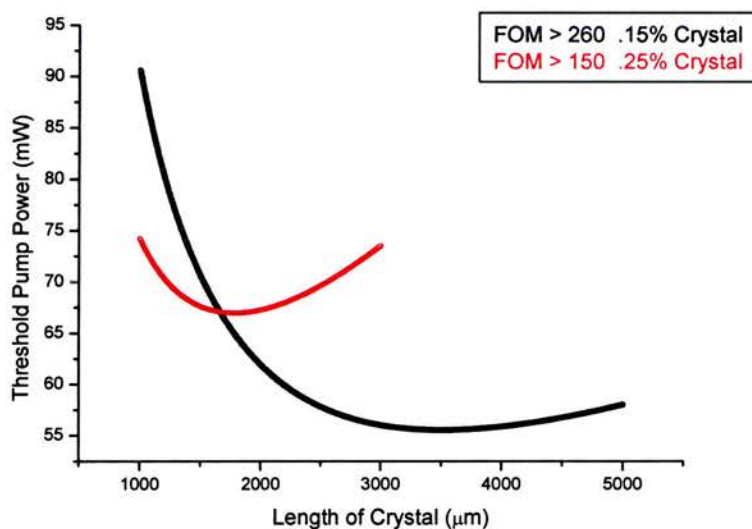


Figure 5.1: Threshold pump power for lasing of Ti: Sapphire laser with two alternative laser crystals.

It is evident from figure 5.1 there is a minimum in threshold pump power for the 0.15% doped crystal at a length of 3.5mm and for the 0.25% doped crystal there

is a minimum threshold pump power for a 2mm long crystal. These two crystal options will afford different slope efficiencies and the predicted output powers as a function of incident pump power are shown in figure 5.2.

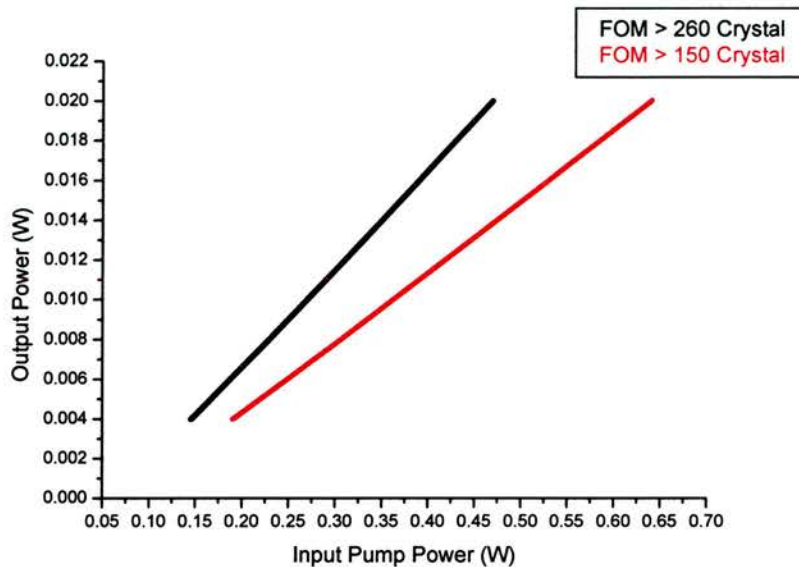


Figure 5.2: Output power as a function of input pump power for the two different crystal options.

The higher slope efficiency of the FOM > 260 (0.15% doped) crystal is attributable to lower absorption and scattering of the laser radiation. This modelling indicates that a crystal length of around 3.5mm (FOM > 260 0.15% doped) will afford the highest slope efficiency and lowest threshold of these two crystal options. However, this will place higher demands on the intracavity dispersion compensation than the 2mm crystal of the more highly doped material.

An important factor in achieving low threshold operation is to ensure the focus of the laser mode is on the front face, or very close to the front face of the crystal [5]. This is required to ensure the highest possible brightness transfer from the pump light to the laser mode. The next step, therefore, in terms of laser design, is to decide on a cavity configuration that will allow for this tight focus of the laser mode and a pump focussing arrangement. The pump focussing geometry will depend on the size and position of the waist of the laser mode.

A diagram indicating the dimensions of the final cavity can be seen in figure 5.3 and table 5.1. This cavity was based on the work published in [6]. The laser cavity was selected as it provided the tight focus of the laser mode within the gain crystal required for low-threshold operation. It also allowed for the circular output beam that may be important for some applications.

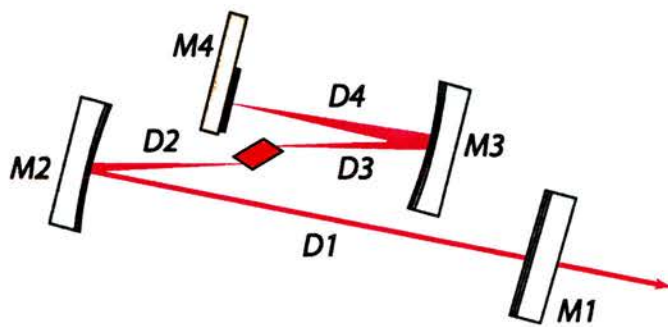


Figure 5.3: Diagram indicating the cavity dimensions for the prospective low-threshold Ti: sapphire laser.

Cavity Dimension	Value
D1	150mm
D2	25mm
D3	70mm
D4	80mm
Angle between D1 and D2	Very small
Angle between D3 and D4	6 degrees
M4	SESAM/HR
M1, M2, M3	HR mirror (transmission <0.1%) RoC M2 = 50mm, M3= 75mm M1=output coupler

Table 5.1: Cavity dimensions for the prospective low-threshold Ti: sapphire laser

The result of using the ABCD matrix-modelling program “LCAV” to calculate the beam profile throughout the laser cavity is shown in figure 5.4. This laser cavity provided a tight focus of the laser mode within the front face of the crystal along with a $25\mu\text{m}$ radius spot on the mirror M4. This spot size provides sufficient fluence on the saturable absorber to ensure stable modelocking at low intracavity powers as well as minimising the potential damage incurred should the laser lapse into Q-switching instabilities, as described in section 4.2. The saturation fluence of the SESAM was $110\mu\text{J}/\text{cm}^2$; this fluence demand can be met with only 5mW of output power with a 0.5% output coupler in this cavity configuration. However, operation of a laser so close to the fluence condition of a saturable absorber usually results in unstable modelocking. This cavity design also ensures a very tight focus of the laser mode ($13\mu\text{m}\times 14\mu\text{m}$) on the front face of the gain crystal. In order to achieve efficient operation the focussed pump mode parameters must match this. Figure 5.5 shows a plot of threshold in mW as a function of the pump laser waist size at the front face of the crystal. This figure shows that a minimum in threshold of around 50mW can be achieved by having a pump waist in the crystal of $10\mu\text{m}$ in radius.

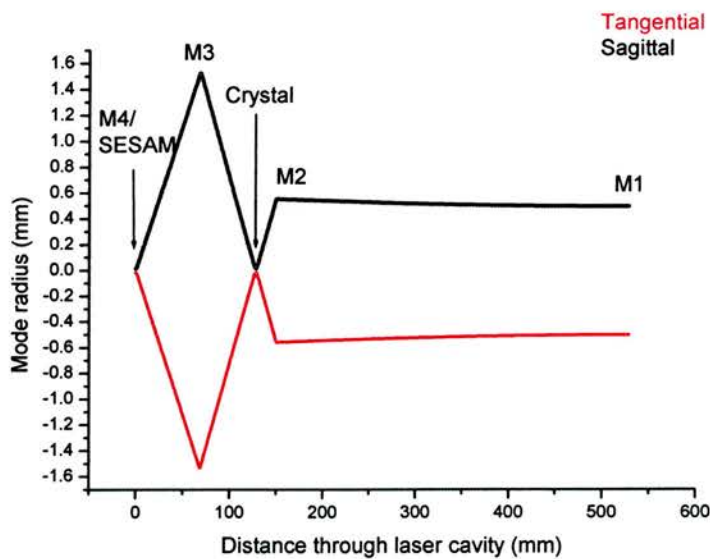


Figure 5.4: Change in spot size as the laser mode propagates through the potential low-threshold cavity

In figure 5.6 the final pump beam waist at the front face of the crystal is plotted against the beam radius before the focussing lens. This figure shows that the incoming beam must be 2mm in radius before the focussing lens to achieve the desired final waist size in the crystal. This can be achieved quite readily using a 1:2 telescoping arrangement and a 100mm focal length lens for a Spectra-Physics Millennia pump laser.

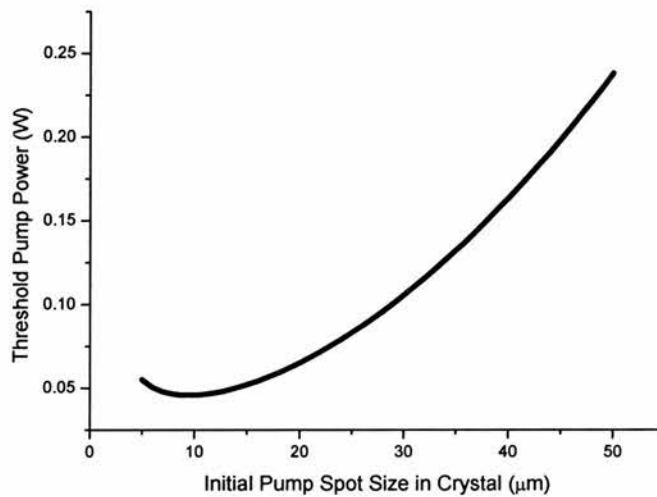


Figure 5.5: Theoretical threshold pump power in mW versus size of intracavity pump mode waist.

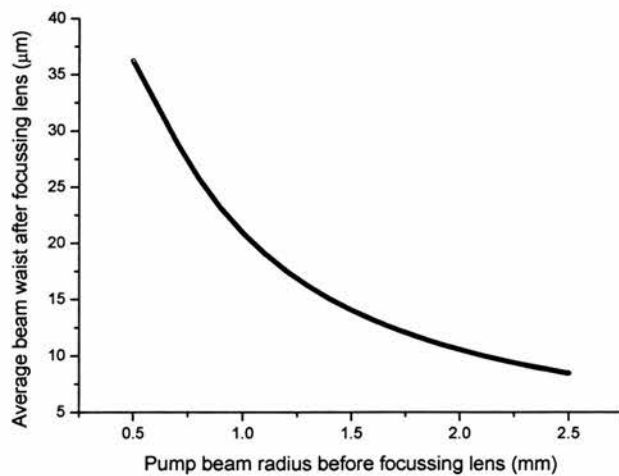


Figure 5.6: Final pump waist size in crystal as a function of incoming pump beam radius

The intracavity parasitic loss must also be minimised to ensure efficient operation. This can be done through the use of only high-precision intracavity optics and good quality optical coatings. Reduction of the intracavity loss in the case of a femtosecond laser can also be achieved through the use of mirror-based dispersion compensation schemes. This avoids the inclusion of prisms, which will incur a small loss from reflection off the Brewster surface as well as propagation loss through the prism glass. Minimisation of the parasitic loss can be done experimentally and a detailed investigation of this is the subject of the next section.

The work described in this section shows clearly that there is some considerable potential for a new class of “reduced threshold” modelocked Ti: sapphire lasers. If indeed the threshold can be reduced to the levels indicated here, the cost of the pump laser and by implication to overall cost of overall system could be reduced dramatically as could the cost of the whole system. The next sections describe the experimental realisation of such a low-threshold, femtosecond laser together with the application of a new low-cost pump source in a cw laser system.

5.3 Experimental realisation of the low-threshold, SESAM-modelocked Ti: sapphire laser

5.3.1 Assessment of the cw laser system

The two crystal samples described in section 5.2 were purchased and used as the gain medium in the laser cavity shown in figure 5.3. The Findlay and Clay loss analysis (described in section 4.5.1) was then carried out on each of the crystal samples in order to experimentally confirm which of the two samples would provide the most efficient laser system. The results of this experiment are shown in figure 5.7. The loss associated with a laser containing the 2mm long crystal was a very large 2.9% whereas the loss associated with a laser containing the 3.5mm long crystal was 0.3%. Due to this large difference in associated loss, this project continued concentrating on the 3.5mm long crystal and the investigations of the 2mm long crystal were discontinued.

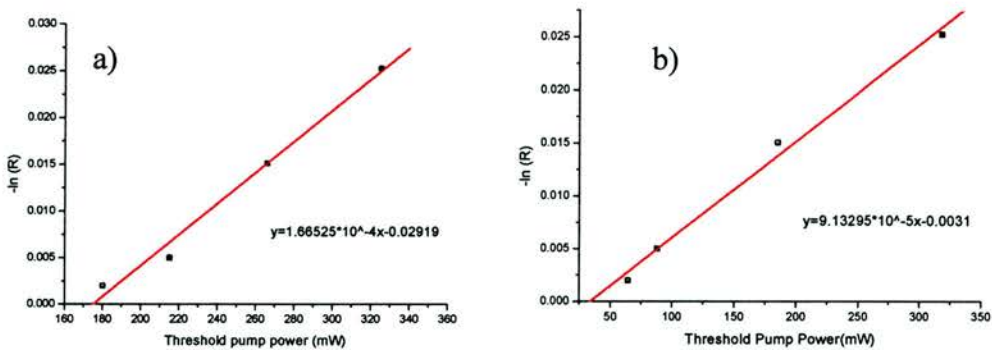


Figure 5.7: Results of the Findlay and Clay loss analysis for the (a), 1.65mm long highly doped sample and (b), the 3.5mm long less highly doped crystal.

The laser was then constructed both with and without a 2:1 pump telescope in place in order to gauge the importance of good mode matching in such a laser system. The power-transfer characteristic both with and without the telescope is shown in figure 5.8. This telescope arrangement made a considerable difference to the threshold pump power. Without the telescope, the threshold was approximately 85mW. However, with the enhanced matching between the pump and laser mode provided by the telescope the threshold was reduced to around 60mW, for a 0.5% output coupler.

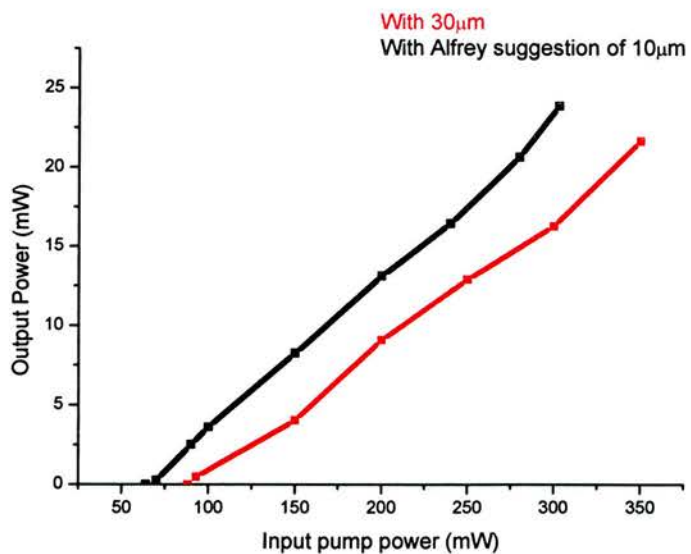


Figure 5.8: Comparison of the power transfer characteristic without the pump telescope arrangement in place (red line) and with the pump telescope arrangement in place (black line) with a 0.5% output coupler.

If this laser was to be successfully modelocked, it was important to know the tuning range of the oscillating wavelength. With this in mind a single fused silica prism was inserted into the laser cavity to tune the centre wavelength of the output. The measured tuning curve is shown in figure 5.9. This plot shows the output power from the laser as a function of oscillating wavelength for ~300mW incident pump power. This laser offered a tuning range of 135nm, from 775nm to 910nm. The peak output power from the laser was found at 790nm, coinciding with the maximum in stimulated emission cross-section associated with Ti: sapphire.

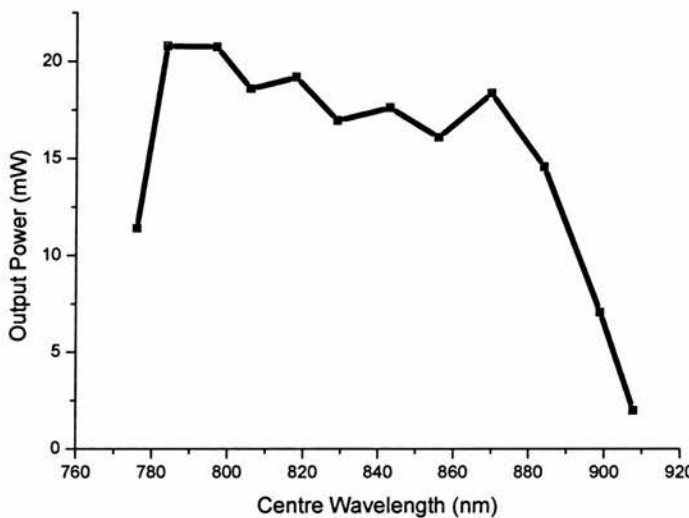


Figure 5.9: Output power as a function of centre wavelength for 300mW incident pump power and a 0.5% output coupler

The low doping of the crystal (dopant concentration: 0.15%, FOM > 260) meant that the absorption coefficient for the pump light was relatively low. This absorption was measured as 2.2cm^{-1} , which means that on a single pass of the crystal 54% of the incident pump light is absorbed. If the pump beam was double passed then the absorption of the pump light should increase to approximately 80%. A 100mm focal length lens was used to collimate the remaining pump light after the 75mm radius of curvature folding mirror and a highly reflecting mirror for 532nm was used to reflect the light back into the crystal. This enhanced the power transfer characteristic of the laser system and this is evident from the data plotted in figure 5.10. This data shows a change in slope efficiency from 9% to 11%.

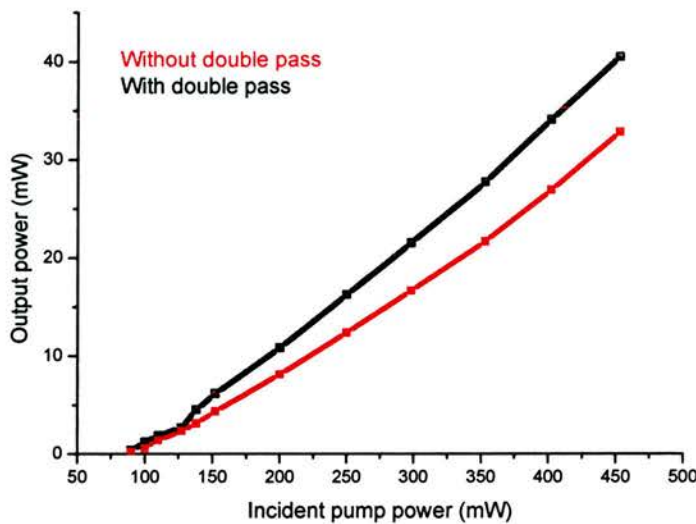


Figure 5.10: Power transfer characteristic with the double-pass arrangement in place (black line) and without (red line).

Two dispersion compensation options were investigated for this laser: one was to use a fused silica prism pair requiring a separation of 50cm to fully compensate for pulse broadening through the crystal; the other was to use the multiple cavity Gires-Tournois interferometer (MCGTI) mirrors supplied by Prof. Robert Szipocs (*R&D Lezer-Optika Bt., Budapest*). These dispersion-compensating mirrors are described in chapters 2 and 3. The insertion of the two prisms increased the length of the collimated arm, D1 in figure 5.3, and incurred a drop in output power from 20mW to 14mW, through the parasitic loss mechanisms described in section 5.2. The insertion of two MCGTI mirrors, with two reflections from each per round trip caused the centre wavelength of the laser output to change from 800nm to 850nm, this in turn caused the output power to drop from 20mW to 18mW. The low-loss SESAM used in the Cr: LiSAF lasers described in Chapter 3 had a centre wavelength of 850nm associated with its response. This meant that the MCGTI mirrors would provide dispersion compensation with the lowest insertion losses in a laser using this SESAM as the modelocking element. Use of the MCGTI mirrors would also allow for a more compact cavity configuration.

5.3.2 Assessment of the modelocked laser system

The laser cavity shown schematically in figure 5.11 (a) was constructed. The round-trip dispersion was calculated using the simple model developed in chapter 3 and was found to be close to 0fs^2 . The output spectrum of the laser was highly unstable and oscillated between a regime which offered $\sim 4\text{nm}$ of spectral bandwidth and one which offered $\sim 10\text{nm}$ of spectral bandwidth. The results from chapter 3 indicated that, for stable modelocking, the Cr: LiSAF lasers required between -100fs^2 and -150fs^2 net dispersion in the cavity. These results indicated that there was insufficient negative net GDD in the cavity for stable modelocking. This was remedied by an extra reflection from an MCGTI mirror, shown schematically in figure 5.11 (b).

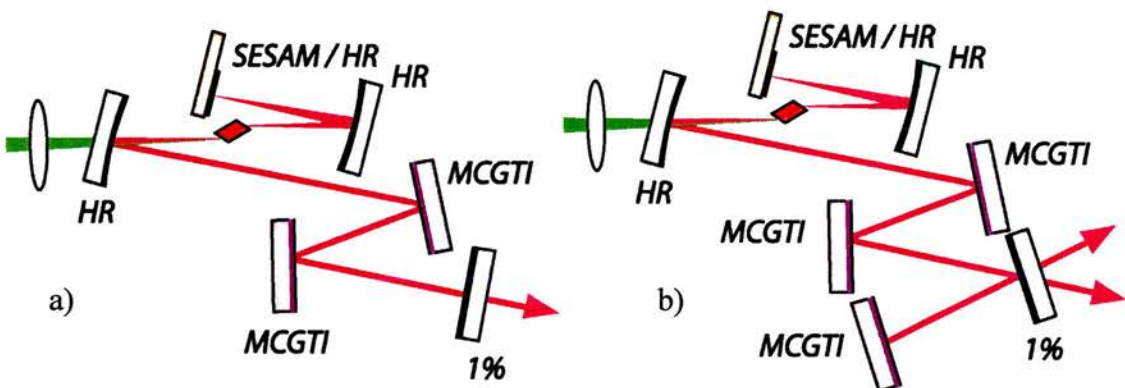


Figure 5.11: The cavity which produced unstable modelocked pulses, (a), and the cavity which produced stable modelocked pulses, (b).

The addition of this extra reflection had the disadvantage that there were now two output beams from the laser, but it did provide a stable modelocked output. The round-trip GDD and third-order dispersion (TOD) are plotted in figure 5.10. Operation at around the dip in TOD shown in figure 5.12 (b) will allow the generation of pulses shorter than $\sim 100\text{fs}$. This is thought to be the factor limiting the output pulse duration in the miniature Cr: LiSAF lasers incorporating MCGTI mirrors discussed in chapter 3.

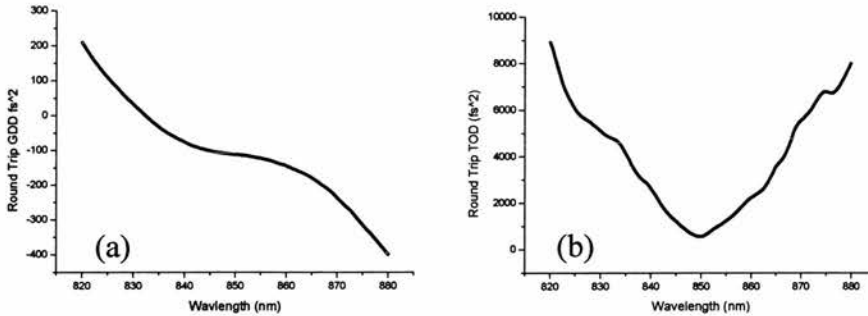


Figure 5.12: The round-trip GDD, (a), and TOD, (b), that provided stable modelocking

When the laser modelocked it oscillated with a centre wavelength of 845nm and produced bandwidth-limited 75fs pulses. The spectrum and autocorrelation profile of these pulses can be seen in figure 5.13. A total output power of ~80mW was generated for 1W of incident pump power with a 1% output coupler and a double-pass of the pump light. Figure 5.14 shows the power transfer characteristic obtained with a 0.5% output coupler, 1% output coupler, and the combination of a 1% output coupler and a double-pass of the pump light. Modelocking of this laser could be achieved with as little as 5mW output power (1% output coupler) through continuous adjustment of the intracavity optics. The repetition rate of this laser was ~300MHz

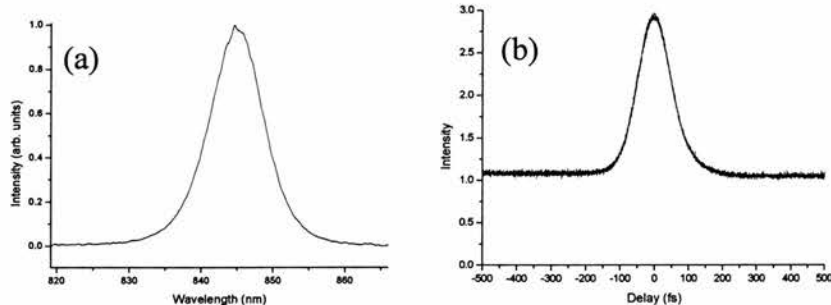


Figure 5.13: Spectrum (a), and measured autocorrelation profile, (b), of the output from the laser indicating bandwidth-limited 75fs pulses

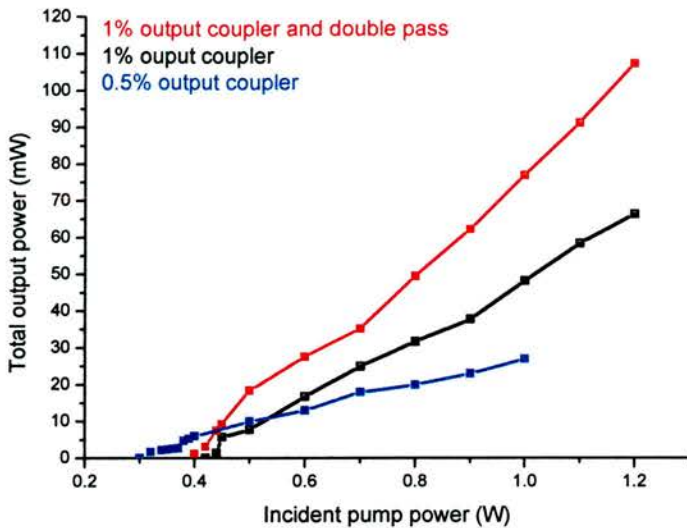


Figure 5.14: Power transfer characteristic of the modelocked laser shown with a 1% output coupler and double-pass of the pump light, a 1% output coupler and a 0.5% output coupler.

The data presented in figure 5.14 show a pump power threshold of 300mW with a 0.5% output coupler and 400mW with a 1% output coupler. The thresholds and power transfer characteristics shown in figure 5.14 demonstrate that a pump laser generating 10W of 532nm light (for example the Spectra-Physics Millennia) is not required to ensure respectable modelocked output powers from a Ti: sapphire laser such as this. After miniaturisation of the laser footprint and ensuring a low threshold pump power the next obvious step is to reduce the physical size of the pump laser as described below.

5.4 Ti: sapphire laser pumped with miniature green laser

The Photonics Innovation Centre (PIC) at the University of St Andrews manufactures a frequency-doubled Nd: YVO₄ laser capable of producing up to 300mW of 532nm light. A Ti: sapphire laser pumped by a green laser which does not require closed-loop water cooling and requires very few external electronic components would be an important step in femtosecond laser development. There are many applications -such as biomedical imaging- where it would be advantageous to have a laser that is both portable and robust. It is for

this reason that an investigation into pumping the cw Ti: sapphire laser described in section 5.2 with the miniature green laser was initiated.

From the results presented in the previous section it can be seen that the PIC laser is unlikely to produce significant modelocked output power from the SESAM modelocked laser. On the other hand, it should be possible to construct a cw laser with respectable output power. An experimental setup which allowed the Ti: sapphire laser to be aligned using the Millennia beam and subsequently allow the PIC laser to be utilised as a pump source is shown in figure 5.15.

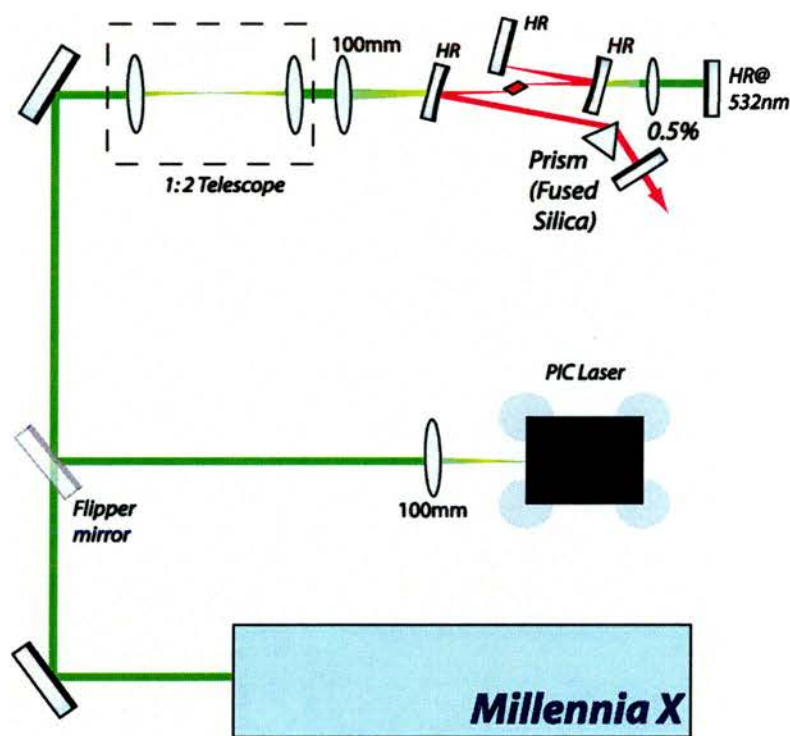


Figure 5.15: Experimental setup used to align the laser using the Millennia and subsequently switch to using the PIC laser as a pump source.

The width of the collimated PIC laser beam before the flipper mirror was measured as 1.1mm by 1.2mm, this is similar to the Millennia beam which has dimensions of 1mm by 1mm. However, it was noted that the spatial quality of the laser beam was subject to quite dramatic changes with time and developed a secondary laser spot. Further to this, the output power was also subject to fluctuation between 290mW and 250mW. This output power was measured after the telescope system shown in figure 5.15.

The Ti: sapphire laser produced around 4mW of output power without a double-pass of the pump light whereas with a double pass in place the laser produced over 10mW of output power when pumped with the PIC laser. The Ti: sapphire laser was not tunable but instead operated on discrete wavelengths separated by several nanometres. Tilting of the output coupler or prism made the spectral output of the laser change from one of these allowed oscillating wavelengths to another. It is thought that this is due to the non-Gaussian distribution of intensity in the crystal and poor pump/laser mode-overlap. This was confirmed when the Millennia output power was lowered to that of the PIC laser and used as a pump source and produced 17mW of output power at a different centre wavelength. The jump from 10mW with PIC laser to 17mW with the Millennia demonstrates the difference in spatial quality between the two laser beams. The free-running spectral output of the laser when pumped with the PIC laser can be seen in figure 5.16 alongside the free-running spectral output of the laser when pumped with the Millennia. The transverse mode profile of the Ti: sapphire laser output changed from being an ideal TEM_{00} mode to a TEM_{01} mode when the transition was made between the two pump sources.

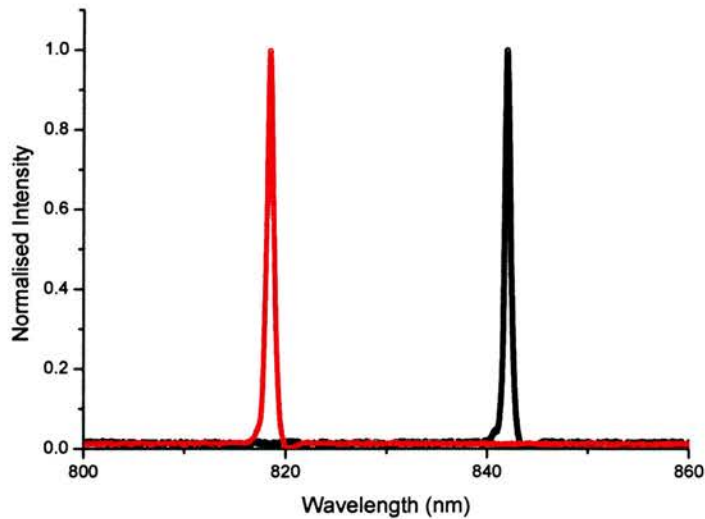


Figure 5.16: The output spectrum of the laser when pumped with the Millennia (red) and with the PIC laser (black). The Millennia gave a TEM_{00} Ti: sapphire laser output whereas the PIC laser gave a TEM_{01} Ti: sapphire laser output.

Should the spatial quality of the next model of the PIC laser improve to an $M^2 \sim 1$ and the intensity stability of its output power improve then the work presented here should provide the basis for a miniature Ti: sapphire laser capable of producing 75fs pulses. Development of a higher quality pump laser that retains the same level of compactness would allow both the Ti: sapphire laser and pump source to be contained within a single chassis.

5.5 Conclusions

This chapter contained subject matter relating to a modelocked Ti: sapphire that incorporated a SESAM that utilised MCGTI-mirror based dispersion compensation. The laser proved to be more compact than its low-threshold KLM counterparts but still retained both a competitive pump power threshold and power transfer characteristic. The laser produced bandwidth-limited 75fs pulses with $\sim 80\text{mW}$ of total output power for only 1W of incident pump power. If the MCGTI mirrors and SESAM could be redesigned for 790nm, the wavelength corresponding to maximum gain in Ti: sapphire, then the threshold could be further lowered. Also, replacing the laser crystal with a shorter crystal with higher dopant concentration (but still the same high FOM such as the material described in the chapter 4) would reduce the number of reflections required on the MCGTI mirrors and allow all the power to be coupled out of the laser in a single beam.

An interesting investigation into the miniaturisation possibilities of the pump source was undertaken. Encouragingly, an assessment of a simplified Ti: sapphire laser having an inexpensive green pump laser showed that an output power of 10mW could be obtained in a cw regime. Both enhancing the spatial quality of the output from the green laser and increasing its output power will improve the performance of this Ti: sapphire laser. Should these two requirements be met then a compact Ti: sapphire laser pumped by a miniature green source may become a reality. Such a laser, which combines low cost with ruggedness, would open up a range of applications where the higher output powers produced by large, expensive Ti: sapphire laser systems are not required.

References

- [1] A. A. Lagatsky, E. U. Rafailov, C. G. Leburn, C. T. A. Brown, N. Xiang, O. G. Okhotnikov, and W. Sibbett, "Highly efficient femtosecond Yb : KYW laser pumped by single narrow-stripe laser diode," *Electronics Letters*, vol. 39, pp. 1108-1110, 2003.
- [2] A. Stingl, M. Lenzner, C. Spielmann, F. Krausz, and R. Szipocs, "Sub-10-fs Mirror-Dispersion-Controlled Ti-Sapphire Laser," *Optics Letters*, vol. 20, pp. 602-604, 1995.
- [3] A. M. Kowalevicz, T. R. Schibli, F. X. Kartner, and J. G. Fujimoto, "Ultralow-threshold Kerr-lens mode-locked Ti : Al₂O₃ laser," *Optics Letters*, vol. 27, pp. 2037-2039, 2002.
- [4] A. J. Alfrey, "Modeling of Longitudinally Pumped Cw Ti - Sapphire Laser-Oscillators," *IEEE Journal of Quantum Electronics*, vol. 25, pp. 760-766, 1989.
- [5] J.-M. Hopkins, "Compact, Low Threshold Femtosecond Lasers," in *Physics and Astronomy*. St. Andrews, 1999.
- [6] B. Agate, B. Stormont, A. J. Kemp, C. T. A. Brown, U. Keller, and W. Sibbett, "Simplified cavity designs for efficient and compact femtosecond Cr : LiSAF lasers," *Optics Communications*, vol. 205, pp. 207-213, 2002.

Chapter 6 - Modelocked Ti: sapphire laser using a VECSEL as a saturable absorber device

6.1 Introduction

In this chapter the construction of a cw Ti: sapphire laser tunable from 900nm to 990nm and the subsequent incorporation of a saturable absorber based on a vertical extended cavity surface emitting laser (VECSEL) device for modelocking [1] are both described. Three distinct intracavity wavelength selection techniques are compared; involving use of (i) a birefringent filter, (ii) a single prism, and (iii) a pair of prisms. All three approaches provided approximately the same degree of tunability but each had associated advantages and disadvantages that are discussed in this chapter. The effect of current injection to a saturable absorber is studied and a number of results presented relating to the change in laser output with centre wavelength and injection current.

The VECSEL used was a prototype product on loan from Novalux Inc. (*1220 Midas Way, Sunnyvale, CA*). The VECSEL, when placed into the focussed arm of the laser cavity, provided similar saturable absorption to that of the SESAM and SBR modelocking elements described in chapter 1. The key feature of the VECSEL was that a voltage could be applied to its active area allowing charge carriers to be electrically injected or removed from the device. The effect of changing the bias to the VECSEL on the output pulse duration was studied. Interestingly, when a periodic voltage is applied to the VECSEL a ‘switchable’ modelocked regime was observed. When a forward or reverse bias voltage was applied across the VECSEL, it was observed that the Ti: sapphire laser does not produce a periodic sequence of pulses. By contrast, when the VECSEL has no injection current then the Ti: sapphire laser emitted relatively long duration, modelocked pulses. This has been interpreted as the first observations relating to a novel modelocking regime where the pulse formation process can be controlled through current injection to a saturable absorber. It is predicted that such behaviour is a first step towards opening up interesting applications in

optical data-systems where it might become possible to reference the pulse train to an external clock.

Modulation of a saturable absorber has been carried out previously. The authors of reference [2] report a fibre laser that is harmonically modelocked by the modulation of the saturable absorber by remnant pump light. In this case, any pump light that is not absorbed within the fibre is used to modulate the SESAM modelocking element, allowing a more stable modelocked output to be achieved. The novelty of the approach described here, where current injection is used to control the modelocking process, represents a quite distinct scheme compared to that described by the authors of reference [2].

6.2 Vertical extended cavity surface emitting lasers – a background

In a vertical cavity surface-emitting laser (VCSEL) the light is extracted perpendicular to the plane of growth whereas edge-emitting lasers emit light parallel to plane of growth [3]. Vertical cavities are desirable for a number of reasons. In particular, such devices can be tested on the wafer rather than being removed, cleaved and tested subsequently. Furthermore, edge-emitting semiconductor lasers typically oscillate on many longitudinal modes and have an asymmetric emitting area. This generally produces an output with relatively poor spatial mode quality. On the other hand, the VCSEL emits light vertically, through the epitaxial structure, removing the need for cleaved facets because the active area can be sandwiched between two Bragg-reflecting mirrors. This can facilitate a laser output in the form of a symmetric transverse mode.

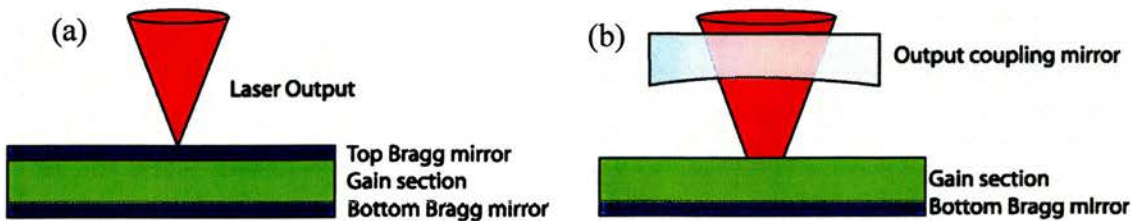


Figure 6.1: Structure of a VCSEL (a), and a VECSEL, (b).

In references [4] and [5], the main differences between a VCSEL and a VECSEL are described in the case of the optically-pumped device but much of the discussion is also relevant to devices pumped by electrical injection. A VECSEL is similar to a VCSEL but it needs an external mirror to complete the laser cavity because it has no top distributed Bragg reflector (DBR) built into its structure. This is illustrated in figure 6.1. The relatively small emitting area associated with a VCSEL means that the output powers are usually limited to a few milliwatts at most. The external cavity associated with the VECSEL enables a larger area to be pumped, whilst still retaining single transverse mode operation, allowing much higher brightness transfer from the pump to the VECSEL device, in the optically pumped case. Also, through careful selection of the output coupling mirror a large output power can be generated at the expense of spatial quality, or high spatial quality laser light can be extracted at the expense of output power. Figure 6.2 shows the detailed structure of the VECSEL device used as a saturable absorber in this chapter.

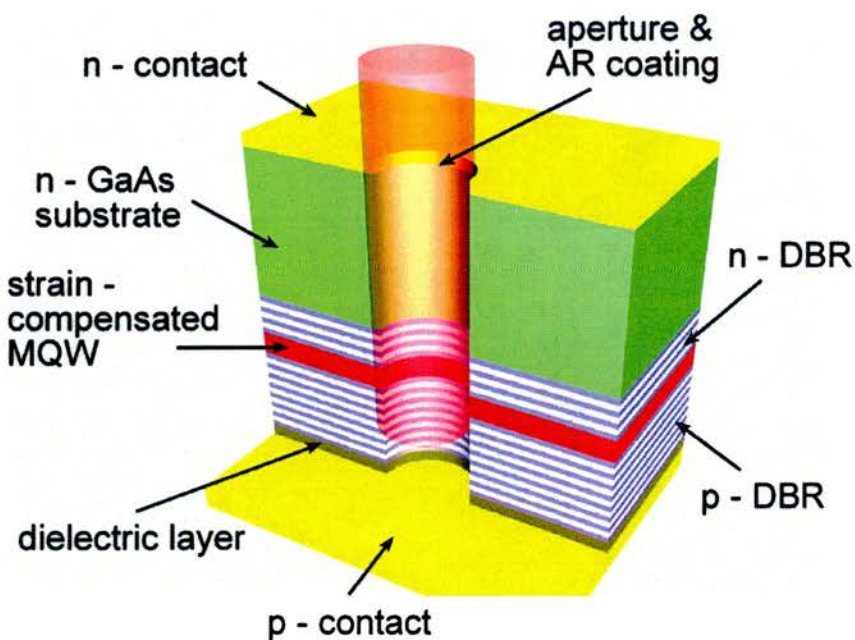


Figure 6.2: The structure of the Novalux extended cavity surface emitting laser [3].

The gain section of the device shown in figure 6.2 consists of several strain-compensated InGaAs quantum wells located at the antinodes of the standing

wave to ensure maximum gain. The number of quantum wells and the strain compensating layers are not known due to commercial confidentiality. The gain region is sandwiched between a p-DBR (Distributed Bragg reflector) and an n-DBR. These two mirrors form a Fabry-Perot type of structure in the device to ensure single longitudinal mode operation. The n-doped top DBR has a reflectivity of 70-80% whereas the p-doped bottom DBR has a reflectivity approaching 99%. Due to the low reflectivity of the n-DBR lasing can only be established with the use of an external mirror. In its simplest form, this extended cavity can take the form of a thin-film mirror coating deposited on the substrate, to create a device similar to a VCSEL. This VCSEL-like device has an emitting aperture of 10-20 μm and an output power of \sim 10mW. Scaling to a larger emitting area and longer cavity with external optics allows higher powers to be extracted from the laser system.

Rafailov et al. [6] placed the device in an external cavity with a curved output coupler as the end mirror, and the power transfer characteristic was obtained for a number of different output couplings. These results are shown in figure 6.3.

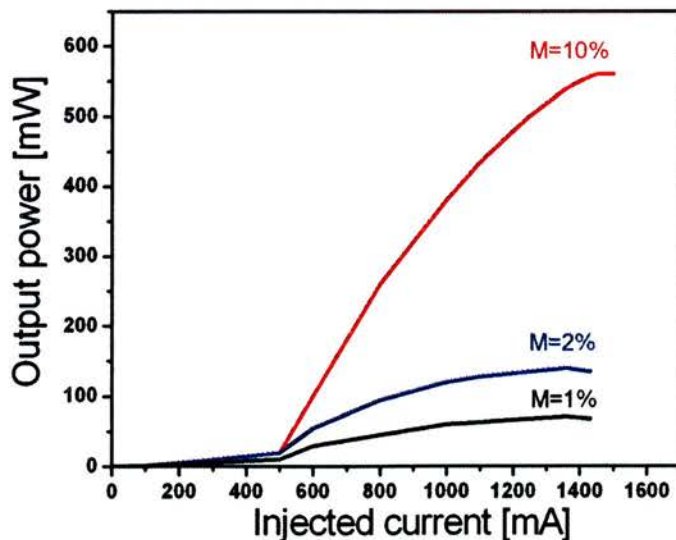


Figure 6.3: Output power from VECSEL with a number of different output couplings.

Shown are 1% (black), 2% (blue), and 10% (red).

The device lased with similar output power characteristics with 25mm, 50mm, and 100mm radius of curvature output couplers. The only difference between the laser systems was as the radius of curvature of the output-coupling mirror

was increased, the mirror had to be moved further away from the device itself. This implied that the laser mode formed in the external cavity remained unchanged as the radius of curvature of the output-coupling mirror was increased. It was possible to get in excess of 500mW of output power from the device through appropriate selection of the output coupling.

The structure of the VECSEL laser is conceptually very similar to that of the first generation of SESAM-type modelocking elements [7]. In both structures there are several quantum wells located at the antinodes of the standing wave set up inside the structure when laser light is incident on the device. In the case of the SESAM this saturates the absorption associated with the device at a very low incident fluence. However, there are several differences between the VECSEL and a SESAM. Some of the important differences in the context of this chapter for the VECSEL include the following; (i) the quantum wells are in a Fabry-Perot etalon which will restrict the extent of the spectral bandwidth, (ii) the top DBR of the device is separated from the incoming laser beam by a substrate, this will increase the associated reflection loss of the device, (iii) The substrate as well as the top and bottom mirrors are doped with charge carriers such that this will also increase the reflection loss of the device.

6.3 Ti: sapphire laser operating beyond 900nm

6.3.1 Introduction

The VECSEL had an emitting zone of $150\mu\text{m}$ diameter. It can be deduced that the beam diameter must be appreciably smaller than this when it reaches the end mirror/VECSEL position to avoid clipping of the laser mode. The VECSEL was designed for laser action around 980nm, which is relatively far removed spectrally from the peak (at 790nm) of the Ti: sapphire gain curve. The following sections describe how all these constraints were overcome to demonstrate the successful use of the VECSEL as an equivalent saturable absorber device.

6.3.2 Design of the “>900nm Ti: sapphire laser”

The laser incorporated a 10mm long Brewster cut Ti: sapphire crystal as the gain medium. Mirrors with high reflectivity at 980nm were used to ensure that the

gain/loss characteristic of the laser would favour operation as close to 980nm as possible. [The cavity design and dimensions are shown in figure 6.4 and in table 6.1.] This cavity provided $\sim 15\mu\text{m}$ radius focus of the laser mode on the end mirror, M4, where the VECSEL was to be placed. The high reflectivity intracavity folding mirrors available for this experiment had a radius of curvature of 100mm.

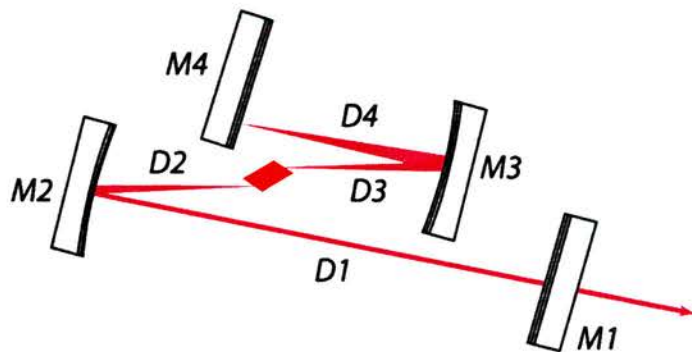


Figure 6.4 Cavity arrangement for the Ti: sapphire laser.

Cavity Dimension	Value
D1	200mm
D2	50mm
D3	221mm
D4	65mm
Angle between D1 and D2	6 degrees
Angle between D3 and D4	3.5 degrees
M4	VECSEL/ HR
M2, M3	HR mirror (transmission <0.1%) RoC M2 = 100mm RoC M3 = 100mm
M1	2% OC

Table 6.1: Cavity dimensions for the Ti: sapphire laser with the VECSEL used as a saturable absorber.

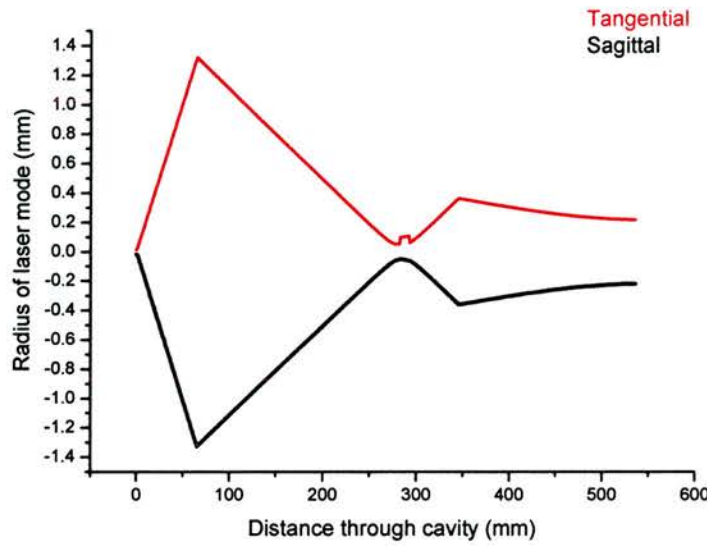


Figure 6.5: The spot size of the laser mode as it propagates through the laser cavity.

As in chapter 4, the LCAV ABCD matrix modelling software was used to calculate the spot size throughout the cavity. The calculated change in spot size is shown in figure 6.5. The pump light from a Spectra-Physics Millennia Xs, operating at 532nm, was focussed onto the laser crystal using a 125mm focal length lens. Without any intracavity tuning element the laser operated at ~910nm and produced around 500mW of output power for 10W of incident pump power with a 2% output coupler in place. In order to tune the laser output to around 980nm the three different techniques investigated were: (i) the birefringent filter described in chapter 3, (ii) a single SF10 prism, and (iii) two SF10 prisms with a movable slit.

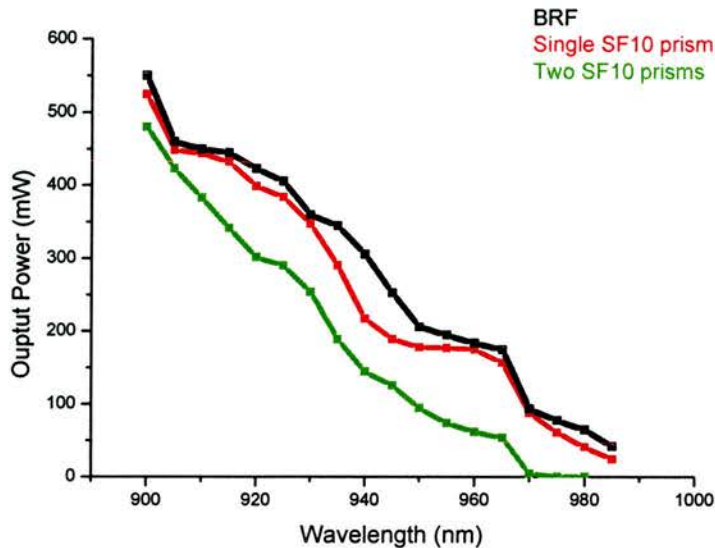


Figure 6.6: Comparison of three ways of tuned outputs for a Ti: sapphire laser. A birefringent filter (black), a single SF10 prism (red) and two SF10 prisms combined with a slit (green). These results were taken using a 2% output coupler and 10W incident pump power.

The results of these tuning experiments are shown in figure 6.6. Only the BRF and single prism techniques provided tuning to 980nm. The decision was made to use the single prism as a tuning element in this laser cavity because the difference in tuning range between the single prism technique and the BRF was insignificant. The benefit of the prism was that it also gave the opportunity to insert some intracavity negative group delay dispersion (GDD) and allow the generation of sub-picosecond pulses.

6.4 Ti: sapphire laser using a VECSEL as a saturable absorber

6.4.1 Initial investigations

This section details the methods employed to align both the VECSEL and Ti: sapphire lasers in the same cavity. Firstly the Ti: sapphire laser was aligned with a standard dielectric high reflector in the mirror position M4. Mirror M4 was then replaced with the VECSEL. The VECSEL was then aligned using around 100mA forward bias such that the Ti: sapphire laser aligned previously, became the extended cavity required for laser action. When the VECSEL had been

successfully configured with this cavity the position of the pump focus on the laser crystal was adjusted until both lasers were oscillating in the same cavity. This had the immediate effect of shifting the free-running wavelength of the Ti: sapphire laser from 910nm up to 940nm. This change in centre wavelength is due to the change in the gain/loss characteristic associated with the Ti: sapphire laser. The VECSEL was then forward biased with a current of around 20mA and slowly increased to 300mA on. The output spectrum was monitored. The results of this assessment are shown in figure 6.7. These results show a spectral component at 940nm, originating from the Ti: sapphire laser when the VECSEL was operated below its threshold current. As the current supplied to the VECSEL was increased to 202mA a spectral component at 980nm, due to the laser light produced by the VECSEL, became visible on the spectrum analyser alongside the peak at 940nm. As the current was increased to 300mA the power entering the spectrum analyser originating from the VECSEL far exceeded the power originating from the Ti: sapphire laser. As such, the spectral component at 940nm illustrated in figure 6.7 is now far smaller than that at 980nm.

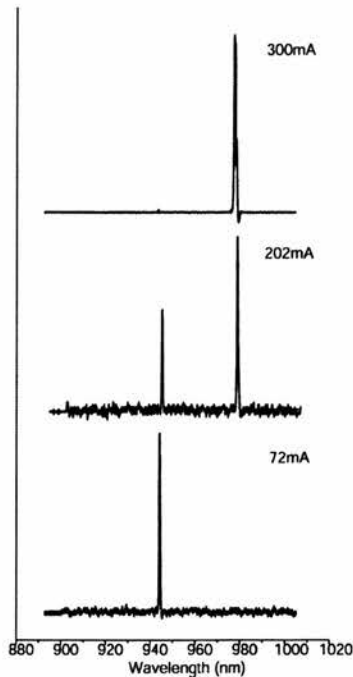


Figure 6.7: Increasing current to the VECSEL (forward bias) and the change in measured output spectrum from the Ti: sapphire laser. It should be noted that the output power at 940nm remained nominally the same.

The RF spectrum of the laser output was measured and a steady peak found at ~250MHz which was the expected modelocked pulse repetition frequency of the laser. The measurement of the output pulse duration was carried out using a photodiode with a response time of 18ps and a 50GHz-bandwidth sampling oscilloscope. The output laser beam intensity was split in two using a 50/50 beamsplitter and a fraction of the output used to both monitor the RF spectrum of the output and trigger the oscilloscope. The other half of the output power was incident on the measurement photodiode. This is shown schematically in figure 6.8.

The author of reference [8] demonstrates that if the oscilloscope has a 50GHz bandwidth then the minimum pulse duration that can be measured using a particular photodiode setup, assuming a Gaussian pulse shape, is not 9ps as would be expected from the sampling rate. It is significantly longer because both the response of the oscilloscope and photodiode must be considered in determining the actual pulse duration. The measured pulse duration may be found by summing the individual impulse responses of the system in quadrature.

For example:

$$\tau_{\text{measurement}} = \sqrt{(\tau_{\text{scope}}^2 + \tau_{\text{photodiode}}^2 + \tau_{\text{actual}}^2)} \quad (1)$$

where $\tau_{\text{measurement}}$ is the measured pulse duration, $\tau_{\text{photodiode}}$ is the response time of the photodiode and τ_{actual} is the actual duration of the pulse.

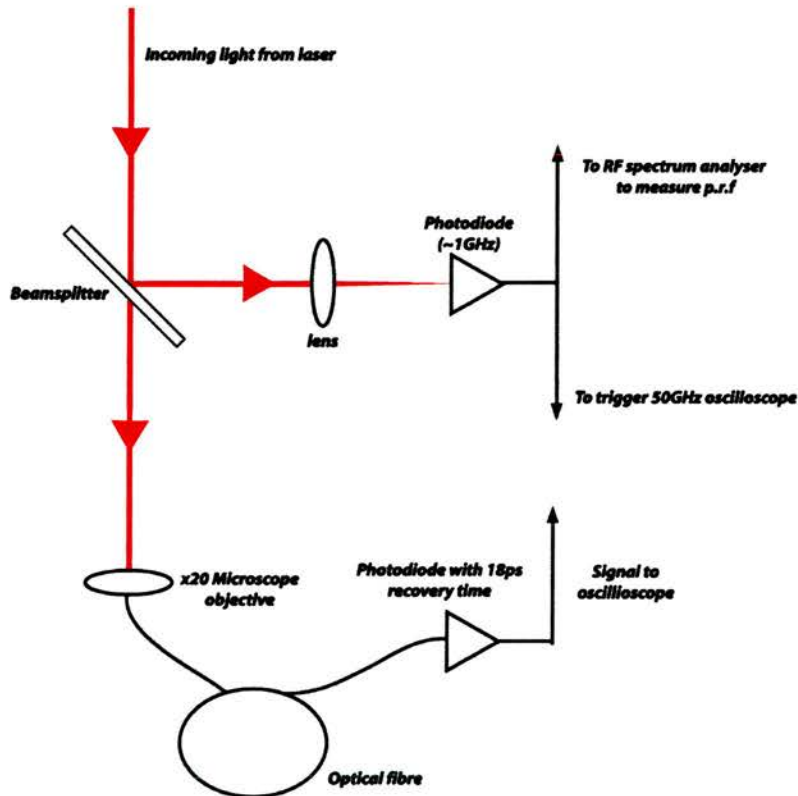


Figure 6.8: System in place to measure the duration of the Ti: sapphire laser output.

However, for the relatively long pulse durations measured in this chapter, there was no need to deconvolve the pulse duration using equation 1 as this correction would have been insignificant.

Firstly, the change in pulse duration was examined as the centre wavelength of the laser was changed. The results obtained can be seen in figure 6.9 where the output spectrum of the laser is shown on the left and the corresponding pulse duration is shown on the right. There is a minimum at 950nm where the pulse duration was 440ps. At 960nm the pulse duration had increased to over 1ns.

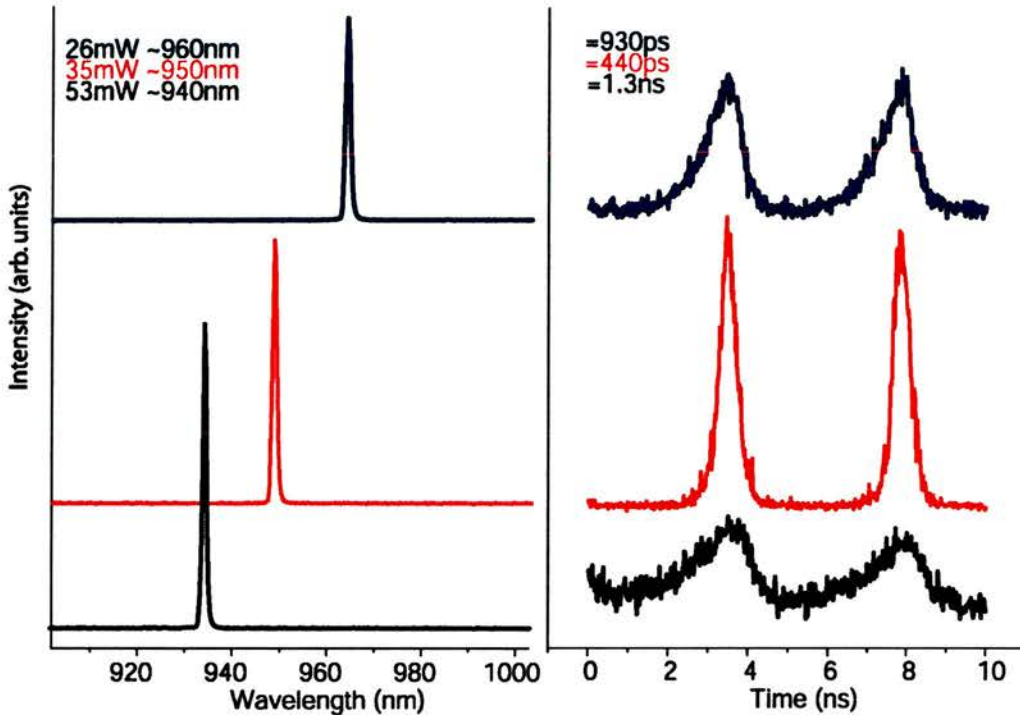


Figure 6.9: The output spectrum of the laser (left) and the corresponding measurement of the pulse duration (right).

The effect of altering the forward/reverse bias to the device was then investigated. These results can be seen in figure 6.10 and table 6.1 where the measured pulse shape is plotted alongside the voltage supplied to the VECSEL. From figure 6.10, the shortest pulses that could be generated were observed when the VECSEL was connected in reverse bias and no voltage was applied. Under these conditions the pulse duration was 300ps and this was the shortest pulse duration that could be achieved in this series of experiments. The effect of forward and reverse bias on the laser system facilitated an increase in output pulse duration. The mechanism for this pulse duration broadening is not yet fully understood although previous work suggests that under reverse bias the recovery time should decrease logarithmically [9]. This should provide shorter pulses as the reverse bias voltage is increased. The physical mechanism for the temporal broadening of the output pulses is not fully understood, although a hypothesis is given in the conclusions section of this chapter.

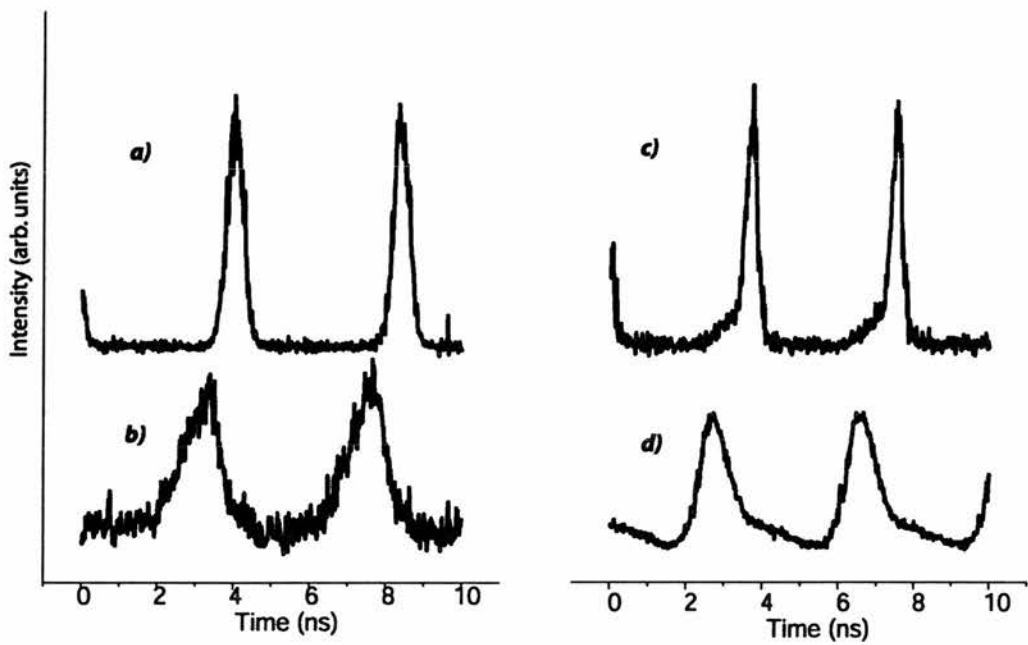


Figure 6.10: Output power and pulse duration for the Ti: sapphire when the VECSEL under forward bias (left) and reverse bias (right).

Caption in Figure 6.10	Current through VECSEL	Voltage across VECSEL	Measured pulse duration	Total output power from laser
a)	0mA	0V (forward bias)	500ps	50mW
b)	20mA	1.26V (forward bias)	1.15ns	53mW
c)	0mA	0V (reverse bias)	300ps	50mW
d)	18mA	-0.03V (reverse bias)	910ps	45mW

Table 6.1: Table of results for figure 6.10.

As the current through the VECSEL was increased the output laser pulses broadened temporally until there was no evidence of pulsed operation on either the fast oscilloscope or the trace that was taken simultaneously on the RF spectrum analyser.

6.4.2 ‘Switchable’ pulses using pulsed incident current

The results of the series of assessments discussed above in section 6.4.1 indicated that with a cw current through the VECSEL the pulse duration increases. With this in mind, a signal generator, which could produce pulses lasting several hundred nanoseconds at a repetition rate of 1MHz was connected to the VECSEL. The effects of having a pulsed current are shown in figure 6.11 for forward bias and in figure 6.12 for reverse bias.

The plot in figure 6.11 shows the output of the laser as measured on a 1GHz-bandwidth photodetector. This detector, while not able to resolve the pulses, gives an accurate representation of whether the laser is operating in a pulsed or in a cw regime. As the current is switched on and off periodically the Ti: sapphire laser modelocks. When the incident current pulse is at a maximum the laser produces a cw output, as shown in zoom-in (a). Conversely, in zoom-in (b) the current pulse is at a minimum and the laser is modelocked. The results shown in figure 6.11 are for a 3kHz modulation on the VECSEL and 150 μ s input pulses. It was found that the modulation of the device was restricted to a maximum frequency of 75kHz and, above this, the VECSEL did not appear to respond linearly as might be expected given that it had not designed for modulation at high frequencies. The main limiting factor in this modulation was the pulse build up time that can be seen at the start of the modelocked regime shown in figure 6.11. In this case it takes ~10 μ s for the well-formed modelocked pulses to evolve from noise. This build up time depends strongly on the relative position of the focus with respect to the VECSEL. This build-up time limited both the duration of the current pulse and the repetition rate, due to the overlap of any two consecutive pulses.

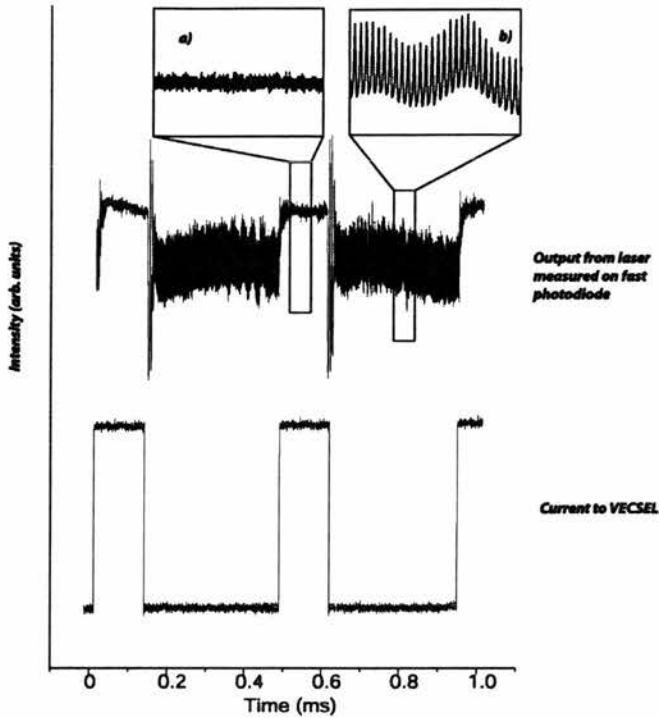


Figure 6.11: The output measured on a fast photodiode from the laser (upper) and the current supplied to the VECSEL (lower) for current pulses of 200mA. Inset (a) shows a cw laser output and inset (b) shows a modelocked laser output.

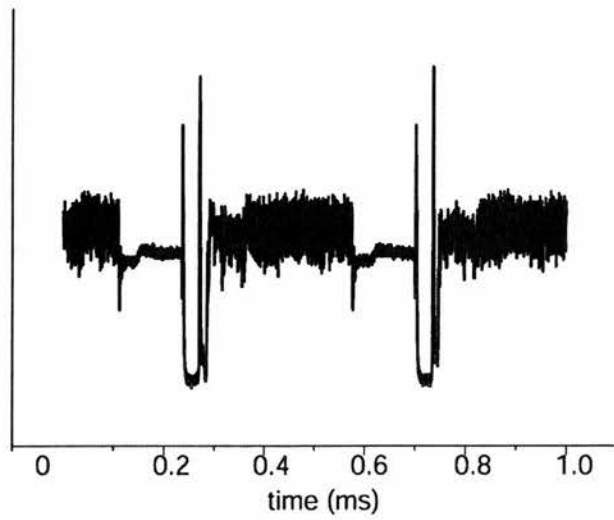


Figure 6.12: Output for the laser under pulsed reverse bias to the VECSEL chip.

The input current pulses were then changed to reverse bias and the results are as illustrated in figure 6.12. Comparison of figure 6.12 and figure 6.11 shows very little change in the output characteristics of the laser when the input pulse sign is

changed from forward to reverse bias. The only real difference is the significant drop in output power when the VECSEL is reverse biased. When the VECSEL is subject to reverse bias, the device acts purely as an absorptive element and saturation of this absorption requires higher incident pulse energy. Thus, this decrease in output power is to be expected.

Although the evaluations detailed in this chapter yielded very interesting results, the processes responsible have not yet been studied fully or explained in terms of the basic physics. It is for this reason that the use of a VECSEL as a saturable absorber is still the topic of ongoing research.

6.5 Conclusions

In this chapter the basic operating parameters and structure of an electrically pumped vertical extended cavity surface emitting lasers (VECSELs) were described. The design and construction of a Ti: sapphire laser that emits wavelengths longer than 900nm was then described. The results of a series of experimental assessments using an electrically-pumped VECSEL as a saturable absorber in a laser cavity were presented. The output pulse duration was measured using a suitably broadband photodiode and sampling oscilloscope combination. The change in pulse duration with oscillating wavelength was examined and, in particular, the effect of forward and reverse bias on the pulse duration was studied. Finally, a pulsed current was supplied to the VECSEL. Interestingly, this pulsed input current allowed the modelocking process in the Ti: sapphire laser to be switched on and off. When the VECSEL was forward or reverse biased the laser did not modelock but when the VECSEL was used purely as a passive element the laser operated in a modelocked regime. This enabled modulation of the modelocked laser at several tens of kHz limited only by the frequency response of the VECSEL device itself.

The pulse durations measured were limited by the intracavity Fabry-Perot etalon present in the VECSEL structure. When reverse or forward bias is applied to the device this could change the reflectivity of the etalon mirrors due to the refractive index contribution of the carriers. This change in reflectivity would

increase or decrease finesse of the etalon. This may, in turn, affect the pulse duration.

The work presented in this chapter represents a first step towards locking the pulse train of a passively modelocked laser to an electrical clock signal. Importantly, locking of the pulse train to an external electrical signal offers applications-related potential for laser sources that might be employed in comms-systems configurations. Notably, if a device could be fabricated which can be modulated at frequencies similar to those associated with the pulse repetition frequency then a type of hybrid modelocking using an actively controlled passive saturable absorber could also be attempted.

References

- [1] J. G. McInerney, A. Mooradian, A. Lewis, A. Shchegrov, E. M. Strzelecka, D. Lee, J. P. Watson, A. Liebman, G. P. Carey, B. D. Cantos, W. R. Hitchens, and D. Heald, "High-power surface emitting semiconductor laser with extended vertical compound cavity," *Electronics Letters*, vol. 39, pp. 523-525, 2003.
- [2] M. Guina and O. G. Okhotnikov, "Harmonic mode locking by synchronous optical pumping of a saturable absorber with the residual pump," *Optics Letters*, vol. 28, pp. 358-360, 2003.
- [3] <http://www.novalux.com>
- [4] W. J. Alford, T. D. Raymond, and A. A. Allerman, "High power and good beam quality at 980 nm from a vertical external-cavity surface-emitting laser," *Journal of the Optical Society of America B-Optical Physics*, vol. 19, pp. 663-666, 2002.
- [5] M. Kuznetsov, F. Hakimi, R. Sprague, and A. Mooradian, "Design and characteristics of high-power (> 0.5-W CW) diode-pumped vertical-external-cavity surface-emitting semiconductor lasers with circular TEM00 beams," *IEEE Journal of Selected Topics in Quantum Electronics*, vol. 5, pp. 561-573, 1999.
- [6] E. U. Rafailov, W. Sibbett, A. Mooradian, J. G. McInerney, H. Karlsson, S. Wang, and F. Laurell, "Efficient frequency doubling of a vertical-extended-cavity surface-emitting laser diode by use of a periodically poled KTP crystal," *Optics Letters*, vol. 28, pp. 2091-2093, 2003.
- [7] U. Keller, K. J. Weingarten, F. X. Kartner, D. Kopf, B. Braun, I. D. Jung, R. Fluck, C. Honninger, N. Matuschek, and J. A. der Au, "Semiconductor saturable absorber mirrors (SESAM's) for femtosecond to nanosecond pulse generation in solid-state lasers," *IEEE Journal of Selected Topics in Quantum Electronics*, vol. 2, pp. 435-453, 1996.
- [8] D. Birkin, "Generation and characterisation of ultrashort diode laser pulses," PhD. Thesis, University of St Andrews, 2001.
- [9] J. R. Karin, R. J. Helkey, D. J. Derickson, R. Nagarajan, D. S. Allin, J. E. Bowers, and R. L. Thornton, "Ultrafast Dynamics in Field-Enhanced Saturable Absorbers," *Applied Physics Letters*, vol. 64, pp. 676-678, 1994.

Chapter 7 - Conclusions and future work

The work carried out during the course of this research project concerned itself with the development of highly adaptable femtosecond laser systems based on Ti: sapphire and Cr: LiSAF gain media. Several significant extensions were made to the parameter space in which these lasers operated. In particular, the maximum pulse repetition frequency, minimum threshold pump power, wavelength tunability, and modulation of the laser output through an electrical current were all subject to experimental analysis. Within this chapter the work detailed in this thesis is reviewed and particular highlights are emphasised. Examples of how this work may be extended in the future are also presented.

In chapter 2, the measurement and analysis of the attributes of thin-film optical coatings were discussed. Techniques through which the dispersive properties of an optical system may be measured were described. The white-light interferometry technique [1] was implemented and used to measure the dispersion in reflection of a dichroic mirror from a particular mirror set. The distinctive but unexpected phase characteristic that appeared in the results of this assessment explained why a Cr: LiSAF laser using these mirrors was able to modelock and produce femtosecond pulses with no intentional dispersion compensation. Analysis of a number of optical coatings capable of supplying the negative GDD required for stable modelocking was discussed. The knowledge gained from this analysis allowed for the custom design of a mirror coating capable of allowing a femtosecond Ti: sapphire laser to be operated at multi-GHz repetition-rates. This mirror coating was designed using the Left, Transmission, Right (LTR) method developed at the University of St Andrews [2].

The integration of negative GDD and saturable absorption has been the subject of previous research. A Gires-Tournois interferometer (GTI) structure has been integrated into a semiconductor saturable absorber mirror (SESAM) to allow for the generation of 125fs pulses with 25mW of average power [3]. This laser did not require any additional intracavity dispersion-compensating elements. Through careful cavity design and dispersion auditing a truly monolithic femtosecond laser cavity could be constructed. The back mirror of the SESAM

used in such a laser would follow on from the ideas presented by the authors of [3] and facilitate full compensation for the pulse broadening due to propagation through the laser crystal.

Chapter 3 presents the results of a series of evaluations using a birefringent filter as a tuning element in a femtosecond Cr: LiSAF laser. This filter was adapted from the design presented by Naganuma and co-workers [4]. These adaptations allowed for the broad spectral pass-bands required when tuning a low-gain modelocked laser. Tunability of the centre wavelength over 20nm was observed when using the specially designed filter in combination with multiple cavity Gires-Tournois interferometer mirrors (MCGTIs). The change in spectral bandwidth and pulse duration over the tuning range was investigated. The results of these experiments confirmed that the filter could be used to influence the oscillating bandwidth and pulse duration generated by a laser system.

The tuning range observed with this laser system could be extended through the use of multiple reflections on GTI mirrors. These reflections would cancel out the residual third order dispersion present in the laser cavity and allow stable modelocking to be achieved over a broader tuning range. Experimentation with reflectivity of the output coupling would quantitatively indicate the degree of bandwidth constriction that any filter order imposed on a laser cavity. Birefringent filters may also open up new avenues in pulse characterisation. A modified autocorrelator setup can be envisaged which contains a birefringent filter in one arm. This will allow the frequency-selection needed to acquire a sonogram trace [5], as shown schematically in figure 7.1.

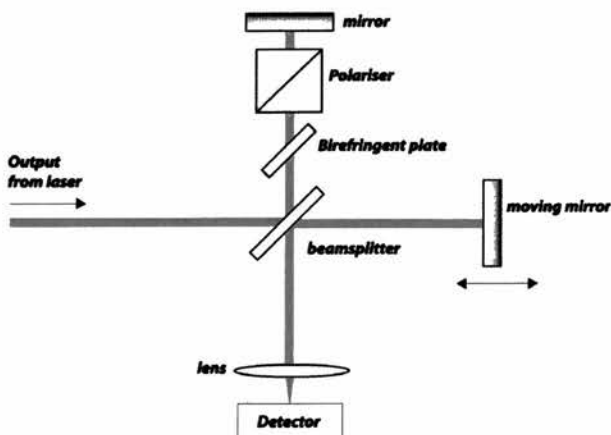


Figure 7.1: A modified autocorrelator setup for acquisition of a sonogram trace.

In chapter 4 an explanation is given for the achievement of high repetition-rate operation from modelocked femtosecond Cr: LiSAF and Ti: sapphire lasers. Modelocked Ti: sapphire and diode-pumped Cr: LiSAF lasers were constructed with repetition-rates of 2.3GHz and 1GHz respectively. Both of the lasers utilised the dispersion-compensating mirrors detailed in chapter 2. Measurement of the mirror coating using the techniques outlined in chapter 2 may throw some light onto how much the dispersive properties of the manufactured mirror coating differ from the theoretical predictions. As the folding mirrors are on curved substrates, to provide control of the spatial properties of the laser mode, such a measurement would be non-trivial as the white-light interferometry technique is more suited to plane mirrors.

The fundamental limit on repetition-rate set by the stimulated emission cross-section in Ti: sapphire was not reached. The limiting factor in this laser was the proximity of the optical components and in particular the implications this had for the number of dispersion-compensating reflections that could be integrated into the laser cavity. If higher repetition-rates were required for a particular application then a method for obtaining the correct dispersion from fewer intracavity reflections would have to be developed. This would be a non-trivial exercise as Ti: sapphire is a very dispersive gain medium. However, it could be achieved through the use of a higher index contrast mirror using an air gap to facilitate a GTI structure with higher group delay dispersion.

In chapter 5, schemes through which the incident pump power requirements for a Ti: sapphire laser can be reduced are established and subjected to theoretical analysis. The construction of a modelocked Ti: sapphire laser that can produce ~80mW of average power for 1W of incident pump power is described. This laser produced bandwidth-limited 75fs pulses. A miniature laser developed in the Photonics Innovation Centre at the University of St Andrews was used as a pump source for a cw Ti: sapphire laser. This laser produced 10mW of output power for 290mW incident pump power.

The performance of the low-threshold Ti: sapphire laser described in chapter 5 could be enhanced through the use of saturable absorber mirror with lower reflection loss. Redesign of all the optical components used within this laser for 790nm would also enhance the power transfer characteristic because this

spectral region corresponds to the highest stimulated emission cross-section in Ti: sapphire. Should the spatial quality of the output from the compact pump laser be enhanced as well as its maximum output power, then a modelocked Ti: sapphire pumped by a miniature green laser may be feasible and indeed practical.

Chapter 6 presents the results from a series of experiments where an electrically-pumped vertical extended cavity surface emitting laser (VECSEL) was used as a modelocking element in a Ti: sapphire laser. Application of an injection current to the active area of this device allowed for a degree of control over the modelocked output pulses. Specifically, when a pulsed current was applied to the device the peak of the current pulse corresponded to an entirely cw output whereas the trough of the current pulse allowed a modelocked output.

The mechanism responsible for the experimental observations detailed in chapter 6 is not clear. A rigorous theoretical analysis would have to be carried out in order to determine what physical mechanisms were responsible for this modulation. As the active region of this device was in a Fabry-Perot cavity, carrier injection to the mirrors may increase or decrease the finesse of the effective etalon structure. This, in turn, will control the bandwidth available to any pulse that is formed. However, the extent to which this effect will be important is not clear. The fabrication of a device capable of high-speed modulation and its application as a saturable absorber may allow the locking of an optical pulse train to an electrical clock signal. This would have interesting and relevant possibilities in respect of applications in high-speed data communications in particular.

References

- [1] I. G. Cormack, F. Baumann, and D. T. Reid, "Measurement of group velocity dispersion using white light interferometry: A teaching laboratory experiment," *American Journal of Physics*, vol. 68, pp. 1146-1150, 2000.
- [2] M. Mazilu, A. Miller, and V. T. Donchev, "Modular method for calculation of transmission and reflection in multilayered structures," *Applied Optics*, vol. 40, pp. 6670-6676, 2001.
- [3] D. Kopf, G. Zhang, R. Fluck, M. Moser, and U. Keller, "All-in-one dispersion-compensating saturable absorber mirror for compact femtosecond laser sources," *Optics Letters*, vol. 21, pp. 486-488, 1996.

- [4] K. Naganuma, G. Lenz, and E. P. Ippen, "Variable Bandwidth Birefringent Filter For Tunable Femtosecond Lasers," *IEEE Journal of Quantum Electronics*, vol. 28, pp. 2142-2150, 1992.
- [5] I. G. Cormack, W. Sibbett, R. Ortega-Martinez, and D. T. Reid, "Ultrashort pulse characterization using a scanning Fabry-Perot etalon enabling rapid acquisition and retrieval of a sonogram at rates up to 1.52 Hz," *Review of Scientific Instruments*, vol. 72, pp. 4071-4079, 2001.

Acknowledgements

Firstly I would like to thank Professor Wilson Sibbett and Dr. Tom Brown for the opportunity to join this research group and for the constant words of encouragement during the course of this project and for the opportunity to submit this thesis.

Secondly I would like to acknowledge the contributions of two of the best scientists I have ever met. Namely Dr. Iain Cormack for his tireless efforts in the lab, for not being put off when nothing worked for months and for knowing when to let me try by myself and make my own mistakes. I would also like to thank Dr. Alan Kemp whose efforts went beyond the call of duty and whose legacy of experimental excellence and Mathcad programs is present in some form throughout this thesis. You two will go far!

My appreciation also goes to a number of friends and colleagues throughout the building. In particular the W-squad and its constantly changing line-up: Pablo, Edik, Alex, Helen, Chris, Will, Michael, Ben, Alan, Maria Ana, Abdul, Tanya (and her spare room), and Michael M. for his mathematical genius.

Thank you to my parents for their constant love and support for everything that I have done over the past 26 years. Thanks to all the inhabitants of 15 Uachdar, Isle of Benbecula, especially Mairi. This would not exist if you and your home hadn't fixed me so quickly. And, finally, to all the diamond weans that I have had the privilege to meet this year!